RESTSTRAHLEN BAND OPTICS FOR THE ADVANCEMENT OF FAR-INFRARED OPTICAL ARCHITECTURE

BY

WILLIAM HENDERSON STREYER

DISSERTATION

Submitted in partial fulfillment of the requirements
for the degree of Doctor of Philosophy in Electrical and Computer Engineering
in the Graduate College of the
University of Illinois at Urbana-Champaign, 2016

Urbana, Illinois

Doctoral Committee:

Associcate Professor Daniel Wasserman, Chair
Associate Professor Minjoo Larry Lee
Assistant Professor Songbin Gong
Assistant Professor Anthony Hoffman, University of Notre Dame

Abstract

The dissertation aims to build a case for the benefits and means of investigating novel optical materials and devices operating in the underdeveloped far-infrared (20 - 60 μm) region of the electromagnetic spectrum. This dissertation and the proposed future investigations described here have the potential to further the advancement of new and enhanced capabilities in fields such as astronomy, medicine, and the petrochemical industry. The first several completed projects demonstrate techniques for developing far-infrared emission sources using selective thermal emitters, which could operate more efficiently than their simple blackbody counterparts commonly used as sources in this wavelength region. The later projects probe the possible means of linking bulk optical phonon populations through interaction with surface modes to free space photons. This is a breakthrough that would enable the development of a new class of light sources operating in the far-infrared.

Chapter 1 introduces the far-infrared wavelength range along with many of its current and potential applications. The limited capabilities of the available optical architecture in this range are outlined along with a discussion of the state-of-the-art technology available in this range. Some of the basic physical concepts routinely applied in this dissertation are reviewed; namely, the Drude formalism, semiconductor Reststrahlen bands, and surface polaritons. Lastly, some of the physical challenges that impede the further advancement of far-infrared techonology, despite remarkable recent success in adjacent regions of the electromagnetic spectrum, are discussed.

Chapter 2 describes the experimental and computational methods employed in this dissertation. Spectroscopic techniques used to investigate both the mid-infrared and far-infrared wavelength ranges are reviewed, including a brief description of the primary instrument of infrared spectroscopy, the Fourier Transform Infrared (FTIR) spectrometer. Techniques for measuring infrared reflection and thermal emission at fixed and variable angles are described.

Finally, the two computational methods most commonly employed in this dissertation are outlined; namely, the transfer matrix method (TMM) and rigourous coupled wave analysis (RCWA) techniques for calculating reflection and transmission spectra for layered materials. The later technique employs the first one in a Fourier space in order to efficiently calculate spectra from layered periodic structures.

Chapter 3 is the first of five to present experimental work carried out in the current course of study and describes a tunable selective thermal emitter made from a thin-film metamaterial composed of germanium deposited upon a layer of highly doped silicon. The structure is essentially an interference filter with an anti-reflection coating (the germanium film) that is significantly thinner than the typical quarter wavelength thickness used in such filters — an effect enabled by the plasmonic properties of the highly doped silicon. The strong absorption band observed in reflection measurements was shown to be selective, tunable by choice of germanium thickness, and largely independent of polarization and angle of incidence. Subsequent heating of the devices demonstrated selective, tunable thermal emission

Chapter 4 describes a different approach to achieving selective, tunable thermal emission; moreover, one that operates in the far-infrared. These devices are made of gold 1D gratings patterned atop aluminum nitride films with molybdenum ground planes beneath. These devices exhibited strong selective absorption that could be tuned by choice of gold grating width. This single parameter was shown to provide absorption resonance tuning across a wide range of the far-infrared with marginal change in the strength and quality factor of the resonance. Subsequent heating of the devices with 2D gratings demonstrated polarization independent selective thermal emission. Computational models of the emission indicated the samples had significantly higher power efficiency than a blackbody at the same temperature in the same wavelength band.

Chapter 5 presents selective thermal emission in the far-infrared from samples of patterned gallium phosphide. The selective absorption of the samples occurs in the material's Reststrahlen band and can be attributed to surface phonon polariton modes. The surfaces of the samples were grated via wet etching to provide the additional momentum necessary for free space photons to couple into and out of the surface phonon polariton modes. Upon heating the samples, selective thermal emission of the surface phonon polariton

modes was observed.

Chapter 6 investigates a potential means of linking lattice vibrations to free space photons. Lightly doped films of gallium arsenide were grown by molecular beam epitaxy and wet etched with 1D gratings. The light doping served to modify the material's intrinsic permittivity and extend the region of its Reststrahlen band. Though the extension of the region with negative real permittivity was small, it extended beyond the longitudinal optical phonon energy of the material, which stands as the high energy boundary of the unmodified material's Reststrahlen band. Hybrid surface polariton modes were observed at energies near the longitudinal optical phonon energy where they are not supported on the surface of the intrinsic material — offering a potential bridge between bulk optical phonon populations and free space photons.

Chapter 7 presents preliminary results exploring the prospect of exploiting an absorption resonance known as the Berreman mode as a mechanism to link optical phonons to free space photons. The Berreman mode is a strong absorption resonance that occurs near the longitudinal optical phonon energy at moderate angles of incidence in polar semiconductors. Preliminary results demonstrate selective thermal emission consistent with the expected spectral position of the Berreman mode in aluminum nitride (AlN), while Raman spectroscopy confirmed the spectral proximity of the longitudinal optical phonon.

The final chapter summarizes the findings and outlines several suggestions for additional research directions that may further advance the pursuit of new technological capabilities in the far-infrared.

To my wife, Rachel Waldemer, who has always been a source of comfort and joy even through the most trying periods of graduate school.

Acknowledgments

This dissertation relied upon the efforts and creativity of my colleagues. Most importantly were those of Prof. Daniel Wasserman whose steady guidance and nimble scientific intuition provided the leadership necessary to make this research possible. I would also like to thank my labmates who served as frequent co-authors and provided unwaivering support and occasional commiseration, especially: Prof. Stephanie Law, Dr. Lan Yu, Dr. Runyu Liu, Dr. Yujun Zhong, Andrew Taylor, and Aaron Rosenberg. I would like to draw special attention to the efforts of a pair of extraordinary undergraduate researchers, Tom Jacobs and Gino Rooney, whose contributions to this work went well beyond the abilities of their peers.

I would like to thank Chris Roberts and his graduate advisor, Prof. Viktor Podolskiy, both of the University of Massachusets-Lowell, as nearly all of this work relied critically upon there insightful input and rare talents. Chris developed an RCWA software package using MATLAB and patiently taught me to make the most of it. This invalubale tool became the first step to exploring new ideas and designing new samples.

I would like to thank our co-investigators Kaijun Feng and Prof. Anthony Hoffman. Anthony served as co-principal investigator with Dan on many of the grants that supported this work, and his knowledge and insight were indispensable.

I would like to thank my additional committee members Prof. Songbin Gong and Prof. Minjoo Larry Lee for graciously agreeing to serve on my doctoral committee.

Table of Contents

Chapter 1

Introduction

1.1 The Far-Infrared

The far-infrared (FIR) region of the electromagnetic spectrum can be considered to fill the space from the edge of the long-wave infrared (13 µm) all the way through to the mm-wave portion of the spectrum. The long-wavelength side of the FIR is most frequently referred to as the THz wavelength range, which is of great interest for a wide variety of optoelectronic, sensing, and imaging applications. The shorter wavelength side of the FIR (20 – 100 µm, which we will refer to as the Reststrahlen band), unlike the THz, has received little attention thus far, despite being a wavelength range of potential interest for a variety of applications (see Section 1.2). The exploration of any wavelength range requires an optical toolkit, consisting of sources, detectors, and optical components such as lenses, beamsplitters, polarizers, and filters. In the 20 – 100 µm wavelength range, such components are few and far between. In large part, this is due to the strong phonon absorption of semiconductor materials, which form the basis of most all optoelectronic devices and in the infrared, most optical materials. We refer to the wavelength range of strong phonon absorption as the semiconductor's Reststrahlen band, which varies between materials and depends on the optical phonon energy of the semiconductor. For wide bandgap materials (SiC, diamond, III-nitrides), the Reststrahlen band lies at high energies (corresponding to free-space wavelengths between 10 – 20 µm). But, for the III-V materials that make up the majority of our optoelectronic infrastructure, phonon energies range across optical wavelengths from 20 – 40 µm, though phonon absorption dominates the total optical losses of these materials for an even broader wavelength range. For this reason, we will refer to a general Reststrahlen band, covering the wavelength range where typical III-V materials become

highly lossy ($\lambda_0 = 20 - 60$ µm). These losses have largely prevented the development of any significant optical infrastructure for the Reststrahlen band, as evidenced by the quantum cascade laser (QCL), which serves as arguably the mid-infrared (MIR) source of choice, as well as a promising THz source, but whose performance decays significantly for devices even approaching the Reststrahlen band [1], a result of phonon absorption in the QCL's constituent materials [2]. Thus, the Reststrahlen band is something of an optical frontier, with little in the way of optical infrastructure and, admittedly, little in the way of motivating applications (though one could argue as to which of the above is the "cause" and which the "effect"). It would not be unreasonable to suggest that the distinct lack of a Reststrahlen band optical and optoelectronic toolkit has limited the exploration of this wavelength range, which in turn has prevented the demonstration of potential applications to drive further exploration. The development of emitters based on electronic transitions in traditional optoelectronic III-V materials seems unlikely, and while efforts to utilize III-nitrides for quantum cascade-like emitters at long wavelengths are exciting [3], efficient emission from such devices may not be realized for some time. The work presented in this thesis aims to highlight challenges against developing a more capable optical architecture operating in the FIR wavelength range and investigate new approaches for enabling such technology.

1.2 Applications

Even with its limited capabilities, a variety of potential applications with unique advantages in the FIR have been identified. For instance, large complex molecules, such as aromatic hydrocarbons [4–6], have distinctive molecular resonances in the FIR. These molecules also have resonances at shorter wavelengths in the MIR, but due to the prevalence of C-C and C-H bonds in these molecules, such higher energy resonances are not distinctive in this range. However, lower energy resonances in the FIR associated with the aromatic ring structures in these molecules are distinctive. Furthermore, the detection and identification of these molecules is of great interest in astrochemistry as these molecules are believed to be among the most abundant molecules in the universe — dispersed among interstellar dust. Far-IR spectroscopy has

been a critical component of efforts to characterize the cosmic microwave background radiation (CMBR) and used aboard landmark missions such as the Cosmic Background Explorer (COBE) [7]. Such instruments aboard spacecraft are typically cooled and can only operate until their coolant is depleted. Advancement of FIR technology could potentially improve responsivity while eliminating the need for cryogenic cooling extending the lifetime of such missions. A specific class of aromatic hydrocarbons known as asphaltenes have been identified using FIR spectroscopy [8–10]. Asphaltenes are an undesirable component of petroleum, which can damage wells and refining equipment. On site, FIR spectroscopic systems could be used to survey and monitor the fraction of asphaltenes present in extracted petroleum — potentially avoiding or mitigating costly degradation of petroleum infrastructure. Recent work has also indicated that FIR spectroscopy may be valuable in the study of sequence-dependent structure of very short polypeptides — potentially leading to new techniques for investigating protein function [11]. In addition to the applications highlighted, the improvement of size, costs, and capabilities of FIR optical architecture will likely enable and encourage further development of new applications.

1.3 State-of-the-Art

Many of the common optical components taken for granted in the visible and near infrared are significantly more expensive, less capable, and more reliant on additional, bulky architecture (e.g. cryogenic cooling and Fourier transform infrared (FTIR) spectrometers) at longer wavelengths. Recent advancements in semiconductor technology have vastly expanded the optical tools now available in the MIR with the tools of choice being the mercury cadmium telluride (HgCdTe or MCT) detector and the quantum cascade laser (QCL). MCT detectors typically require thermoelectric or cryogenic cooling, and commonly available models have adequate responsivity out to wavelengths of $\lambda \sim 20$ µm. This wavelength cutoff makes MCT detectors unsuitable for work in the FIR, where the most commonly used detection devices are the deuterated tryglicine sulfate (DTGS) detector and bolometers. DTGS detectors have slower response times and lower specific detectivities than their MCT counterparts. Bolometers operating in the FIR show improved

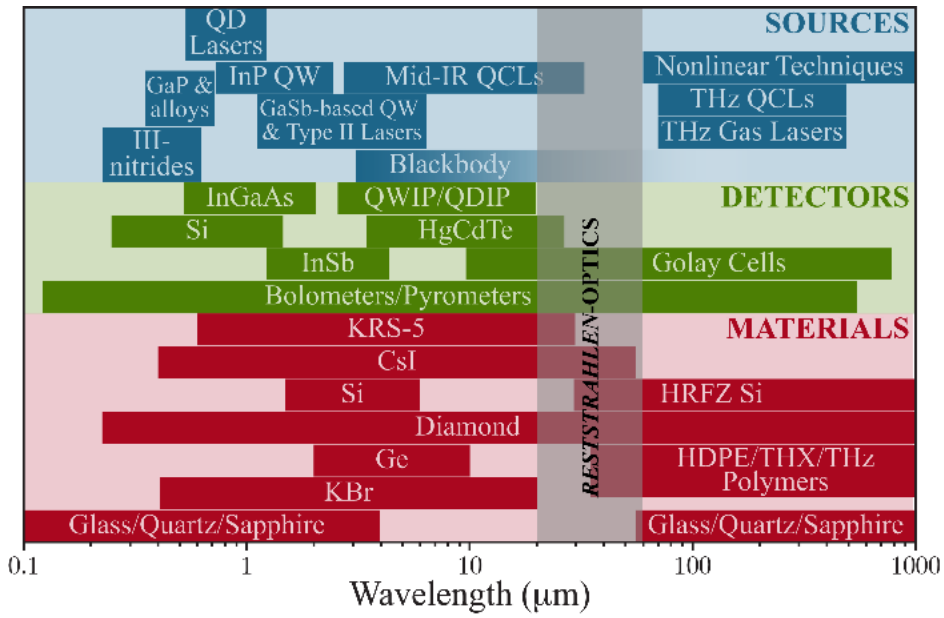

Figure 1.1: Summary of the materials, detectors, and sources that comprise the operational toolkit for Reststrahlen-optics. "HRFZ Si" stands for high resistivity float zone Si.

performance, but also require greater cost and size due to their need to operate at liquid helium temperatures (~ 4 K) along with the associated hassle and expense of handling liquid helium. Likewise, the myriad advantages of the MIR QCL, such as high-power output and broad tunability, are not available at longer wavelengths. The longest wavelengths reached by QCLs to date is $\lambda \sim 24$ μm, which required operation at cryogenic temperatures, and only achieved lasing with pulsed, and not CW, excitation [1]. The most widely available broadband FIR source is the venerable blackbody source, typically appearing in the form of globars installed in FTIR spectrometers. However, thermal blackbody sources lack both wavelength selectivity and power efficiency. Finally, the range of suitably transparent materials becomes sparser along the electromagnetic spectrum from the visible, to the MIR, and to the FIR regions. Potassium bromide (KBr) is commonly used as a substrate for MIR polarizers and beamsplitters, but its transparency only extends to $\lambda \sim 25$ μm. Cesium iodide (CsI) has the widest known transparent infrared range, but is extremely difficult to process due to its softness only suitable in systems wherein range is the higher priority. Thallium bromoiodide (known as KRS-5) is commonly used as a FIR material to $\lambda \sim 40$ μm. Far-IR beamsplitters and windows are often fashioned from thin films of Mylar®,

but its strong absorption bands and lack of mechanical stability limit its optical value. Due to the dearth of ideal optical materials, FIR experimental systems typically rely upon reflective metal optics as much as possible to limit losses and the effects of additional sources of dispersion. Commonly used sources, detectors, and optical materials are depicted along with their respective useful wavelength ranges in Figure 1.1. The gray region highlights the dearth of optical architecture available in the FIR region.

1.4 Surface Polaritons

Polaritons are quasiparticles composed of photons coupled with polar particles in a material — for instance, plasmons and phonons. When these modes are bound to the interface of a metal and a dielectric material, these modes are known as surface polaritons. The metal in question need not be a typical metal whose permittivity depends on its free carriers (i.e. plasmons), but could also be a polar dielectric operating in its Reststrahlen band (i.e phonons, see Section 1.4.2).Both plasmons and phonons are capable of forming surface modes at metal-dielectric interfaces, which are known as surface plasmon polaritons (SPP) and surface phonon polaritons (SPhP), respectively. SPPs have long been the foundation of the field known as plasmonics, which has played in critical role in the development of nanophotonics [12, 13] — the quest to confine electromagnetic radiation into subwavelength volumes in order to realize the same miniaturization in photonics that has led to rapid advancements in electronics. SPhPs have been the subject of more recent investigations, including those presented in this dissertation. They will be discussed at length in later sections.

1.4.1 The Drude Model

The Drude model is a simple physical model used to predict the permittivity of a metal [14]. More generally, the model applies to plasmas or any collection of free carriers in a material such as the conduction electrons of a metal. The model treats the free carriers as a collective oscillation in response to an external electric field with some amount of dampening due to collisions and some amount of bound charge which is unable to respond the external field.

The motion of the free carriers can be described by the mechanical Equation 1.1:

$$m\ddot{\boldsymbol{x}} + m\gamma\dot{\boldsymbol{x}} = -e\boldsymbol{E} \tag{1.1}$$

The free carrier mass is m, the damping constant γ, the carrier charge e, while $\boldsymbol{x}$ and $\boldsymbol{E}$ are the particle displacement and the applied electric field, respectively. Assuming harmonic solutions with angular frequency, ω, to the Equation 1.1, the complex amplitude of that solution can be described as:

$$\boldsymbol{x}(t) = \frac{e}{m(\omega^2 + i\gamma\omega)}\boldsymbol{E} \tag{1.2}$$

This equation for the particle displacement can be related to the total polarization field of the oscillating collection of free carriers by multiplying the displacement by the total free charge as in Equation 1.3, where N is the volume density of the free carriers:

$$\boldsymbol{P} = -\frac{Ne^2}{m(\omega^2 + i\gamma\omega)}\boldsymbol{E} \tag{1.3}$$

The electric displacement field $\boldsymbol{D}$ is shown in Equation 1.4 where ϵ_0 is the vacuum permittivity:

$$\boldsymbol{D} = \epsilon_0\boldsymbol{E} + \boldsymbol{P} \tag{1.4}$$

Substituting the polarization field in Equation 1.3 into Equation 1.4 gives the following where the plasma frequency, ω_p, is described in Equation 1.6:

$$\boldsymbol{D} = \epsilon_b\left(1 - \frac{\omega_p^2}{\omega^2 + i\gamma\omega}\right)\boldsymbol{E} \tag{1.5}$$

$$\omega_p^2 = \frac{Ne^2}{m\epsilon_0\epsilon_b} \tag{1.6}$$

The background permittivity can be attributed to the material's bound charges and is characterized by ϵ_b. Finally, taken together, one can conclude that the permittivity of a material due to free carriers is:

$$\epsilon(\omega) = \epsilon_b \left(1 - \frac{\omega_p^2}{\omega^2 + i\gamma\omega)}\right) \tag{1.7}$$

The Drude model accurately models both the real and imaginary parts of a metal's permittivity using only the parameters ϵ_b, ω_p, and γ. The model works particularly well at longer wavelengths in the radio frequency range, but also quite well at shorter wavelengths. One notable exception is that near the plasma frequency of some noble metals, there is an interband absorption process not accounted for by the carrier scattering rate, γ. This is true of noble metals such as gold and copper, where their color in the visible range can be attributed to interband absorption. A comparison between the modeled and measured permittivity for gold is shown in Figure 1.2.

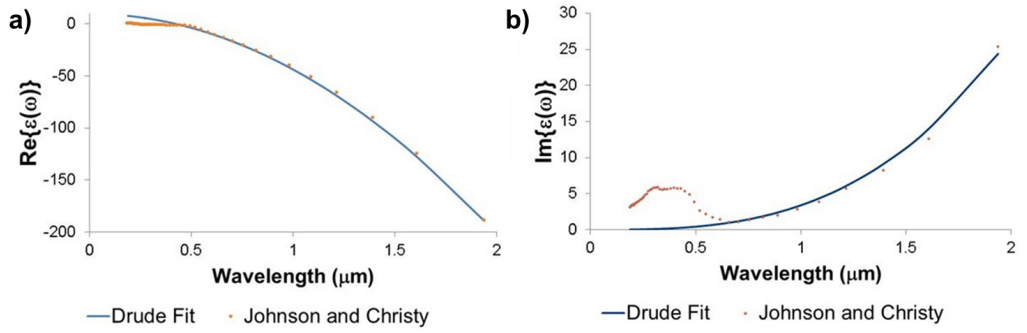

Figure 1.2: (a) Measured (orange dotted) and modeled (blue solid) real permittivity for gold. (b) Measured (orange dotted) and modeled (blue solid) imaginary permittivity for gold. The model and experiment agree well aside from the discrepancy in the visible range, which can be attributed to interband absorption. Drude parameters used: $\omega_p = 2.2 \times 10^{15}$, $\gamma = 19 \times 10^{12}$, $\epsilon_b = 9.6$.

The Drude model works well even for materials with extrinsic carriers such as doped semiconductors. Doped semiconductors can have plasma frequencies at longer wavelengths than the noble metals traditionally utilized in the field of plasmonics, which have plasma frequencies in the visible and ultraviolet range. Thus, for longer wavelength optoelectronics, there has been a growing interest in a class of "engineered" plasmonic materials, whose optical properties

(permittivity) can be optimized for the operational wavelength of interest. These materials include conducting oxides and nitrides [15–17], silicides [18] and germanides [19] in the near-infrared (NIR) to MIR (1 – 5 µm) and doped semiconductors such as Si [20–23], InAs [24], InSb [25], and InAsSb [26] for MIR to FIR (> 4 µm) wavelengths. Very recent results have identified another oxide, cadmium oxide, as a promising tunable and low loss plasmonic material in the MIR (3 – 6 µm) [27]. These materials not only provide the designer with the ability to tailor the plasmonic materials' optical properties, but in the case of doped semiconductors, offer the potential for single-crystal, wavelength flexible plasmonic materials which can be seamlessly integrated into electronic or optoelectronic materials in a single growth. Ultimately, it is this free-carrier response of both traditional plasmonic materials and the new class of engineered plasmonic materials, which results in the negative real permittivity that allows these materials to support both propagating surface plasmon polaritons (SPPs) and localized surface plasmons (LSPs).

1.4.2 The Reststrahlen Band

The Reststrahlen band is a wavelength region of high reflectivity and strong absorption that lies between the transverse, ω_{TO}, and longitudinal, ω_{LO}, optical phonon energies of a polar dielectric. Reststrahlen bands can actually occur near any particularly strong absorption resonance, wherein the Kramers-Kronig relations require an inflection of the real permittivity sufficient enough to cause a narrow region of negative real permittivity. We will concern ourselves with the Reststrahlen bands of common semiconductors, which can be attributed to the strong TO phonon resonance in these materials. The dispersion relation of the TO phonon is altered when it interacts with a photon of similar energy. This interaction results in a quasiparticle known as a phonon polariton and leads to an anti-crossing behavior in the dispersion curves of the TO phonon and the photon. The modification of these dispersion curves is described by the two branches of Equation 1.8, where ϵ_∞ is the short wavelength permittivity of the material, c the speed of light in the material, and ω and k are the angular frequency and wavenumber, respectively, of the two particles.

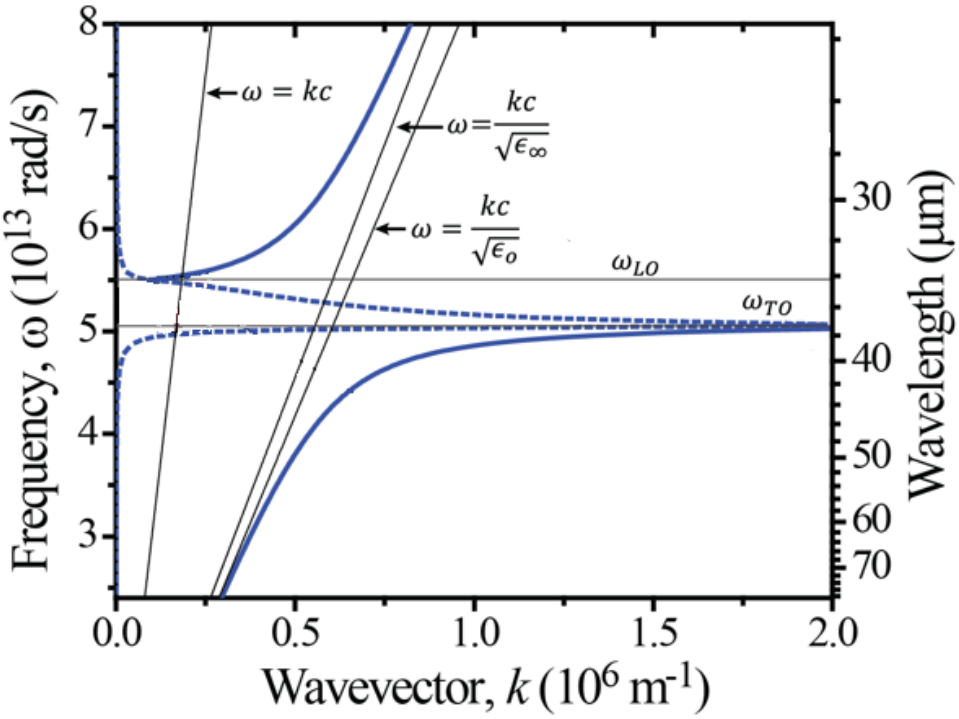

Figure 1.3: Phonon polariton dispersion in the vicinity of the Reststrahlen band of GaAs. Real (solid blue) and imaginary (blue dashed) components of wavevector, k.

$$\omega^2(k) = \frac{1}{2\epsilon_\infty}\left[c^2k^2 + \epsilon_\infty\omega_{LO}^2 \pm \sqrt{(c^2k^2 + \epsilon_\infty\omega_{LO}^2)^2 - 4\epsilon_\infty c^2k^2\omega_{TO}^2}\right] \quad (1.8)$$

An example of the phonon polariton dispersion near the Reststrahlen band using parameters for GaAs is depicted in Figure 1.3. The two branches in solid blue are the real part of the wavevector, k, while the dashed blue is the imaginary part. Note that between the TO and LO phonon energies, the real part of the wavevector has no valid energy values, while the imaginary part is large. This indicates that the phonon polariton is an evanescent, non-propogating wave in this region. Light incident upon the material in this band will be strongly reflected ($R \to 1$), while what little light penetrates the material is rapidly absorbed. Within the same region, the real permittivity of the material is negative with a large imaginary permittivity, which accounts for the strong reflection and is analogous to the high reflectivity of metals at energies below their plasma frequencies. In this sense, semiconductors within their Reststrahlen bands can be said to have metal-like optical properties

[28, 29]. It is for this reason semiconductors can support surface polaritons within their Reststrahlen bands.

The Reststrahlen band permittivity and reflectivity using parameters for indium phosphide is depicted in Figure 1.4 with the permittivity calculated using Equation 1.9, where the new parameters are ϵ_0, the long wavelength permittivity, and Γ_{ph}, the phonon scattering rate.

$$\epsilon(\omega) = \frac{(\epsilon_0 - \epsilon_\infty)\omega_{TO}^2}{\omega_{TO}^2 - \omega^2 + 2i\omega\Gamma_{ph}} \tag{1.9}$$

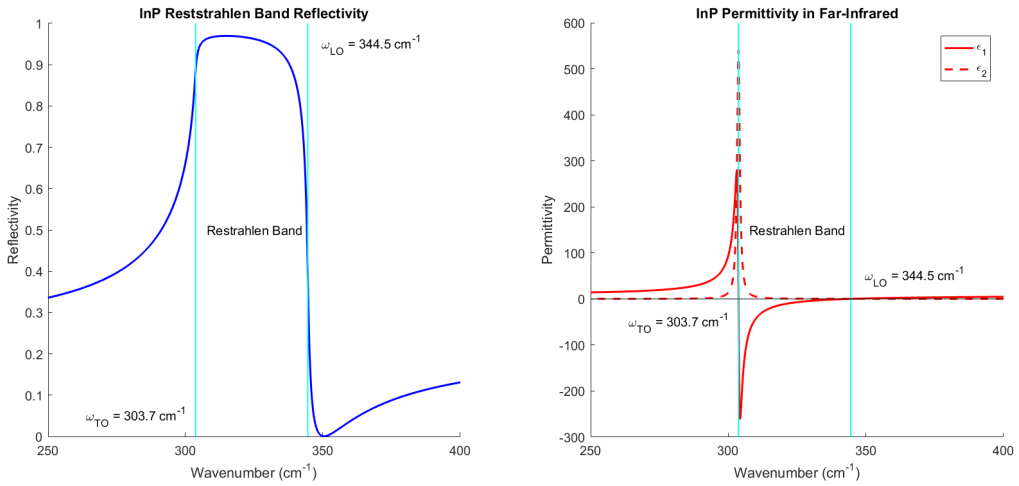

Figure 1.4: Modeled Reststrahlen band reflectivity (left) and permittivity (right) of InP. Reflectivity (solid blue), real (solid red) and imaginary (dashed red) permittivity, TO and LO phonon energies (solid cyan).

The Reststrahlen bands of most semiconductors, save for those composed of more lightweight atomic constituents, will fall in the FIR range of the electromagnetic spectrum. Further exploration of optical processes in semiconductor Reststrahlen bands presents an opportunity for development of novel sources, detectors, and materials in the FIR region, which has not seen the same advance in optical infrastructure available in the MIR and shorter wavelength regions [30]. Due, in large part, to the wide availability of MIR optical components, much of the work investigating surface phonons has used materials of lighter atomic mass – most notably silicon carbide (SiC) [31], and very recently – hexagonal boron nitride (hBN) [32]. SiC is a highly polar material with strong, high-frequency phonon resonances in the MIR ($\sim$ 10 – 12 µm), and has been shown to support both propagating [33–36]

and localized phononic modes [37, 38]. Recent work has investigated the MIR phononic modes of the polar van der Waals crystal, hexagonal boron nitride (hBN), which is particularly noteworthy, as this material exhibits both low losses and natural, dual type hyperbolic responses. Recent work investigating hBN polaritons has demonstrated strongly confined modes propagating over relatively long distances [39], as well as highly confined three-dimensional modes [40].

1.4.3 Surface Polaritons

The study of optical surface waves has been an active and growing field of research for many decades, and one which has benefitted greatly from recent advances in nano-patterning and structuring. These advances have allowed for the demonstration of nano-scale, sub-diffraction optical structures and devices based on the strong optical confinement achievable with tightly bound surface waves. The vast majority of these works have focused on surface plasmons, polariton excitations consisting of charge density oscillations coupled to propagating or localized electromagnetic modes at the interface between a conductor and dielectric [12, 14, 41, 42]. Such excitations form the basis of the field of plasmonics, and have been utilized to demonstrate a wide range of novel optical and optoelectronic devices [43–46]. Typically, the field of plasmonics has utilized noble metals (particularly Au and Ag) as their plasmonic materials. For such traditional plasmonic materials, strong subwavelength confinement occurs when the real part of the permittivity is negative, and of the order of the surrounding dielectric's (positive) permittivity; for Au and Ag, this occurs in the visible to NIR wavelength ranges [47]. At longer wavelengths, traditional plasmonic materials begin to behave more like perfect electrical conductors, precluding much of the subwavelength confinement associated with these metals' plasmonic behavior [48].

From a macroscopic point of view, Maxwell's equations care little where a material's negative permittivity comes from. Thus any material having negative permittivity (and reasonably low losses) can support such surface modes, which has led to interest in materials capable of supporting both propagating and localized surface phonon polaritons (SPhPs and LSPhs, respectively). Unlike their plasmonic brethren, these phononic surface modes are polariton

excitations of lattice vibrations (phonons) and electromagnetic waves, which, like the closely related plasmonic modes, exist at the interface of the phononic material (dielectrics with polar lattices) and a dielectric in a wavelength range where the phononic material has negative real permittivity. This wavelength range occurs in the material's Reststrahlen band, corresponding to energies between the longitudinal and transverse optical (LO and TO, respectively) phonons, and can result in the same subdiffraction confinement observed in SPP and LSP modes, often with lower losses [49].

SPPs can strongly confine light so long as the metal's negative real permittivity has a magnitude on the order of the dielectric's positive real permittivity ($-\epsilon'_m \sim \epsilon'_d$). This is true for noble metals in the visible wavelength range. Alternative plasmonic materials have extended plasmonics into longer wavelengths ranges such as transparent conducting oxides (TCO) [15,16] and transitional metal-nitrides [17] in the near-infrared and doped-semiconductors [20,21,24,50] in MIR to name a few. These materials extend the region of strong plasmonic confinement to longer wavelengths by shifting their respective plasma frequencies to lower energies. It is worth noting that the plasma frequency is the point at which a material's real permittivity changes from positive to negative – transitioning from a primarily dielectric optical response to a metallic optical response. Alternatively, the negative permittivity required to sustain surface polaritons need not come from a metal's free carriers, but rather the negative permittivity within a polar semiconductor's Reststrahlen band can also be exploited, hence SPhPs. Much of the work studying SPhPs has used silicon carbide (SiC) due to its strong phonon resonance in the MIR [34–36]. However, most semiconductors have Reststrahlen bands in the FIR. Most of the wavelength range of the FIR region is covered by the Reststrahlen bands of the common III-V semiconductors and their alloys such as GaAs, GaN, GaP, (Al/In)GaAs, InP, and GaInSb [30]. One of the key aims of our proposal is to leverage SPhPs and the related hybrid surface plasmon phonon polarition (SPPhP) modes as a bridge between free space photons and bulk optical phonons for the purpose of developing novel FIR sources. Figure 1.5 illustrates the Reststrahlen bands of these materials in terms of their FIR permittivity (a), reflectivity (b), and SPhP dispersion (c).

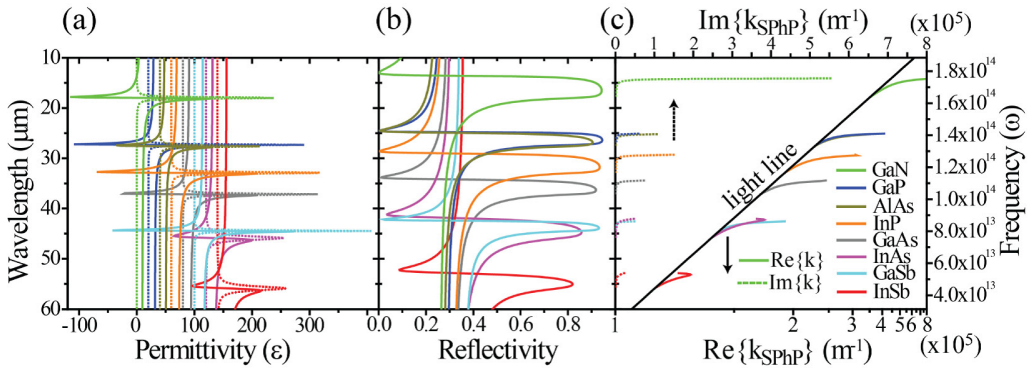

Figure 1.5: (a) Real (solid) and imaginary (dotted) permittivity for the III-V semiconductors GaN (green), GaP (blue), AlAs (yellow), InP (orange), GaAs (gray), InAs (magenta), GaSb (cyan) and InSb (red). Permittivity for each material is offset by 20 for clarity. (b) Normal incidence reflectivity for the materials in (a). (c) Dispersion for surface phonon polariton modes on an air-semiconductor interface for the materials in (a). Real kSPhP (solid) plotted on bottom x-axis, while imaginary kSPhP (dotted) plotted on top x-axis. The light line is shown in solid black.

1.5 Challenges in the Far-Infrared

Much of the progress seen in the MIR over the past decades due to rapid improvements in semiconductor growth and fabrication technology has been transferred to longer wavelengths with only limited success. One of the key reasons for the limitation is that many of the MIR optoelectronic devices depend on intersubband and interband electronic transitions, while electrons couple strongly to longitudinal optical (LO) phonon oscillations near its corresponding energy for a given material — providing fast, non-radiative relaxation pathways. Similarly, photons couple strongly to transverse optical (TO) phonon oscillations. Extending operation of optoelectronic devices beyond the constituent material's Reststrahlen band, bounded by its LO and TO phonon energies, is hindered by the strong interaction between electrons and photons with the material's phonons. In addition to phonon absorption, another important loss mechanism in the FIR is absorption by free carriers. Most, if not all, optoelectronic devices will require doping, which modifies the material's free carrier concentration. The addition of free carriers introduces new optical losses due to damping of the free carriers. The free carrier contribution to a material's permittivity is modeled using the Drude formalism. Both the real and imaginary parts of the free carrier

permittivity increase in magnitude at longer wavelengths making the free carrier absorption in the FIR more significant than at shorter wavelengths [51]. The permittivity contributions of both optical phonons (see Equation 1.9) and free carriers (see Equation 1.7) can be expressed by the Drude-Lorenz model, which is a simple addition of each components' contribution shown in Equation 1.10:

$$\epsilon_m(\omega) = \epsilon_b \left(1 - \frac{\omega_p^2}{\omega^2 - i\gamma\omega} - \frac{\omega_{LO}^2 - \omega^2}{\omega_{TO}^2 - \omega^2 - i\omega\Gamma_{ph}} \right), \quad \omega_p^2 = \frac{Ne^2}{\epsilon_0 \epsilon_b m^*} \tag{1.10}$$

Here, ϵ_b is the background permittivity due to bound charges in the semiconductor, ω_p is the plasma frequency of the Drude model, and γ is the damping of the free carriers. The plasma frequency depends on the free carrier concentration (N), the carrier effective mass (m^*) and the free space permittivity (ϵ_0). The LO and TO phonon frequencies are ω_{LO} and ω_{TO}, respectively, and Γ_{ph} is the damping of the phonons. The collective longitudinal oscillations of free carriers in a material are known as plasmons.

Chapter 2

Experimental and Computational Methods

2.1 Fourier Transform Infrared Spectroscopy

The FTIR spectrometer is the instrument of choice in infrared spectroscopy. Fundamentally, an FTIR is a Michelson interferometer. A broadband infrared light source — typically a globar — is focused and collimated into a beam path (emission experiments use the sample as the source instead of a globar, see Section 2.3). The beam path is split into two paths by an infrared beam splitter. One of the two beam paths is reflected off of a fixed mirror, while the second beam path is directed toward a moving mirror. The moving mirror modulates the path length difference between the two optical beams, thus modulating their phase difference. This modulation of the phase difference leads to constructive, destructive, or partial interference of the two optical paths. After the two beams reflect off of the fixed and moving mirrors, they are recombined as they each pass through the beam splitter for a second time. The recombined beam is then focused on the sample under investigation. The light focused upon the sample is collected in either a transmission or reflection configuration. The light from the sample is then focused onto an infrared photodetector. The experiments performed in this dissertation used a reflection configuration.

Precise control of the moving mirror's position and speed allows for a correlation between the time varying intensity measured by the detector and the phase difference of the optical paths — determined by the mirror's position. The mirror position is precisely monitored by a concurrent interferometer with a helium-neon (HeNe) laser light source. Precise knowledge of the laser's monochromatic wavelength allows for precise determination of the moving mirror's position.

It is important to note that, as an interferometer, the FTIR collects data

about all wavelengths in the optical path at all measurement points. The resulting measurement is known as an interferogram. Mathematically, the interferogram is a phase difference-dependent function known as a field autocorrelation. The phase difference is inferred from the time dependence of the measurement and corresponding knowledge of the mirror position determined by the HeNe interferometer. The phase-dependent interferogram is related to the frequency-dependent power spectrum by the Fourier transform in accordance with the Wiener-Khinchin theorem, hence the "Fourier Transform" part of FTIR spectroscopy [52]. Additional information about FTIR spectroscopy can be found in [53] and [54].

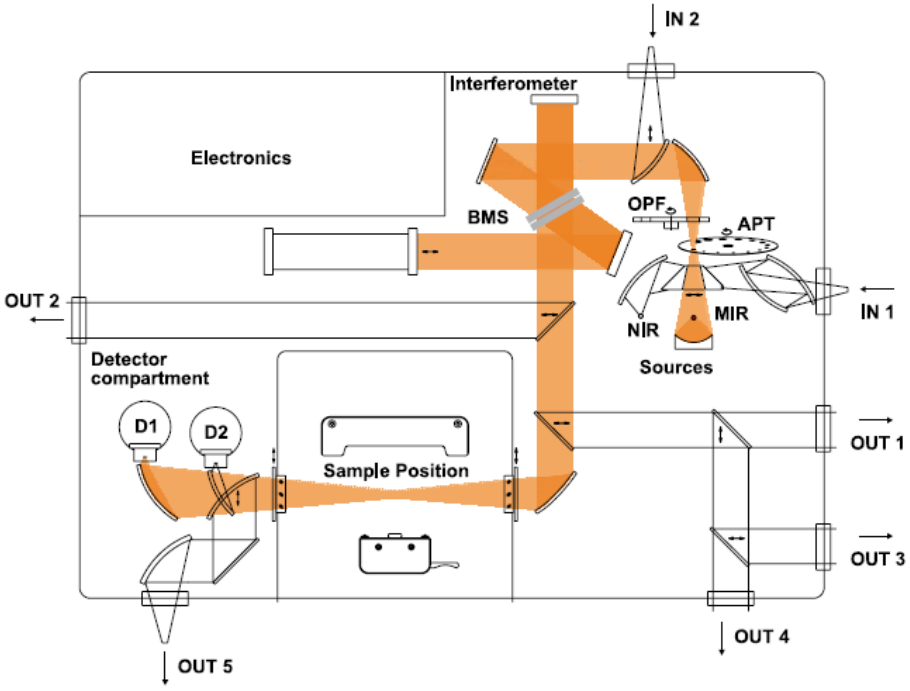

Figure 2.1: Schematic of Bruker v80 series FTIR spectrometer [55].

The experiments performed in this dissertation used both the Bruker v80v and v70 FTIR spectrometers. The primary difference between the instruments is that the v80v can operate under vacuum, while the v70 is purged with dry nitrogen. Both evacuated and purged measurement environments can significantly mitigate the confounding effects of atmospheric absorption in the infrared, but the evacuated environment is more effective. These instruments both feature interchangeable infrared beamsplitters, interchangeable infrared detectors, and both NIR and MIR thermal light sources. Measurements

can be taken internally or externally using several input and output ports (the v80v is equipped with infrared-transparent windows). MIR experiments used an MCT liquid nitrogen-cooled photodetector with zinc selenide (ZnSe) windows and a potassium bromide (KBr) beam splitter. FIR experiments used a room temperature DTGS pyroelectric detector with Mylar® windows and a multilayer Mylar® beam splitter. Figure 2.1 depicts a schematic of the Bruker v80v FTIR spectrometer [55].

2.2 Infrared Reflection Spectroscopy

All of the projects in this dissertation included measurements of the infrared reflectivity of the samples under investigation. These experiments routinely used three distinct experimental configurations for measuring infrared reflection: a Pike 10Spec fixed angle reflection apparatus (Section 2.2.1), a Bruker IR-II infrared microscope (Section 2.2.2), and a custom angle-dependent setup (Section 2.2.3). Another instrument —the Pike VeeMax III — suitable for FIR angle-dependent reflection spectroscopy was made available by a collaborating group (Section 2.2.4). In all cases, reflection measurements were normalized to reflection off of a gold-coated substrate used as a reference measurement. The reflectivity of gold in the MIR and FIR approaches unity for all wavelengths of interest, thus serving as an ideal reference; though, adequately smooth coatings of many other elemental metals would be suitable as well. In cases of particularly low signal strength, a background measurement was also taken, which was subtracted from both the gold reference and the sample measurement before normalizing. A background measurement was typically necessary for FIR reflection experiments due to the lower specific detectivity of the DTGS detector.

2.2.1 Near-Normal Reflection Using the Pike 10SPec

The Pike 10Spec specular reflection apparatus (heretofore referred to as "10Spec") is used to measure reflection off of a sample at a fixed 10° angle of incidence. The 10Spec is particularly convenient as it is inserted and locked into a fixed position within the sample chamber of the FTIR spectrometer. This permits reflection measurements completely within the interior of the

FTIR spectrometer. In the case of the Bruker v80v, the entire sample compartment and instrument compartment of the FTIR can be evacuated to a low pressure vacuum with the 10Spec contained completely within the instrument. Measurements taken under vacuum greatly reduce the effects of atmospheric absorption, which are present in measurements taken under ambient conditions due to the strong infrared absorption of water, carbon dioxide, and other gases. It is also possible to use the 10Spec within the Bruker v70 with similar advantages as this instrument is purged with nitrogen gas; however, experiments in this dissertation did not use the 10Spec in the Bruker v70 FTIR.

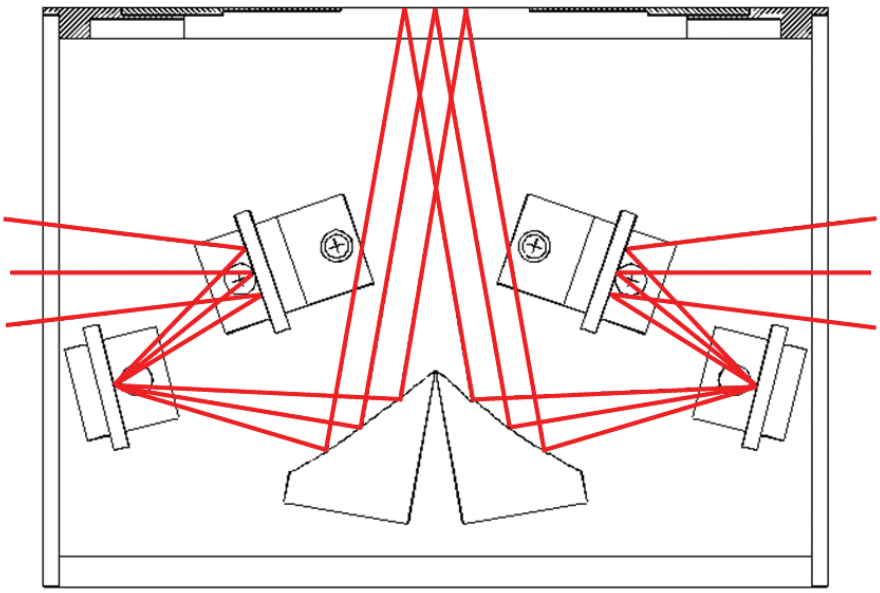

Figure 2.2: Schematic of Pike 10Spec specular reflection apparatus [56].

A schematic of the 10Spec is depicted in Figure 2.2 [56]. The 10Spec is placed inside the FTIR sample compartment such that the beam path enters the right-side port of the apparatus. The sample under investigation is then placed on top of the apparatus over an aperture of interchangeable size. The FTIR beam path is designed such that, in the absence of the 10Spec, the light will be focused upon the center of the chamber where a sample would be mounted in the transmission experimental configuration. The pair of flat mirrors on the right side of the 10Spec are set at a distance from one another such that the focal point of the optical beam is incident upon the rightmost, lower mirror. This mirror is then followed by a curved mirror designed so that

each incoming light ray is directed toward the sample at an angle of incidence of 10°. The curved mirror is shaped such that the 10° angle of incidence is uniform across the entire area of the sample's surface — minimizing spectral broadening due to the finite range of angles of incidence. The reflected light is then collected by an identical set of optical components on the left side of the apparatus and then focused onto the infrared photodetector by a parabolic mirror within the FTIR instrument chamber.

Placement of the sample onto the top of the 10Spec must be undertaken carefully and deliberately. The apertures are circular holes of various sizes within several interchangeable plates, which fit into a slotted opening on the top face of the 10Spec. The clearance between the plate and slotted opening is sufficient to allow for slight lateral translation and out-of-plane tilt of the aperture and sample unless the aperture plate is consistently placed along the same pair of adjacent edges in the slotted opening. Such an error can be significant and confounding for highly angle-sensitive measurements. The bottom side of the aperture plates is inset with a series of concentric grooves. These grooves are meant to scatter light out of the optical path so that the reflectivity of the aperture plate will be negligible. If one should need an aperture even smaller than the smallest available, that smallest aperture plate can be flipped groove side up. A low-reflectivity circular aperature can be placed on top of the plate, while the concentric grooves serve well for properly positioning the new aperture. In this case, it is all the more important to take a background measurement as described in Section 2.2. Polarization selectivity is accomplished by placing an infrared wire grid polarizer into the narrow, but sufficient, space between the 10Spec output port and the left wall of the sample chamber.

2.2.2 MIR Microscope Reflection

The Bruker IR-II infrared microscope is capable of investigating the infrared optical response of a small area of the sample under investigation. The microscope is optically coupled to an output port of the FTIR spectrometer, which directs the FTIR's autocorrelated optical field into an optical path within the microscope. The microscope's internal optics can be switched between reflection and transmission configurations (again, transmission experiments

were not used in this dissertation). The light that is reflected off of the sample is then directed to an internal MCT detector, which was connected over a communications bus to the FTIR spectrometer. A schematic of an infrared microscope similar to the one used in this dissertation is shown in Figure 2.3 [57]. The microscope used in this experiment did not accommodate any interchangeable detectors, such as a FIR DTGS detector. For this reason, the infrared microscope was used only for MIR reflection measurements. The infrared microscope uses an all reflective objective optic (also known as a Schwarzchild, Cassegrain, or reversed Cassegrain objective) with a high numerical aperture. The all reflective objective results in a near absence of chromatic aberration in both the visible and infrared wavelength ranges — allowing the objective to be used in both spectral modes. The high numerical aperture results in a sampling of a wide range of angles of incidence, which may render the infrared scope unsuitable for investigating samples with highly angle-sensitive optical responses. Polarization selectivity is accomplished by placing an infrared wire grid polarizer into the optical path between the microscope and FTIR spectrometer.

Positioning and focusing of the microscope focal point was accomplished using a tandem visible light source and optical path. The microscope features both vertical and horizontal adjustable infrared-opaque internal apertures. Optical imaging is also available through use of the visible light beam splitter beneath the photo tube and attached microscope camera. After locating the area of interest on the sample, the microscope can be switched between the visible and infrared spectral modes. The infrared focal point generally differs from the visible focal point, but the infrared focal point can be found by adjusting the focus while maximizing the infrared signal strength before measuring the spectrum. As with other infrared reflection measurements, it is necessary to take a reference measurement using a gold mirror or other substrate with an optically thick gold coating. It is important to note that differences in the height of the reference sample and the sample under investigation may require adjustment of the focal point. In most cases the infrared signal strength is sufficiently high as to render a background measurement unnecessary. However, when investigating particularly small sample areas, the signal strength may be deficient enough to require a background measurement (see Section 2.2).

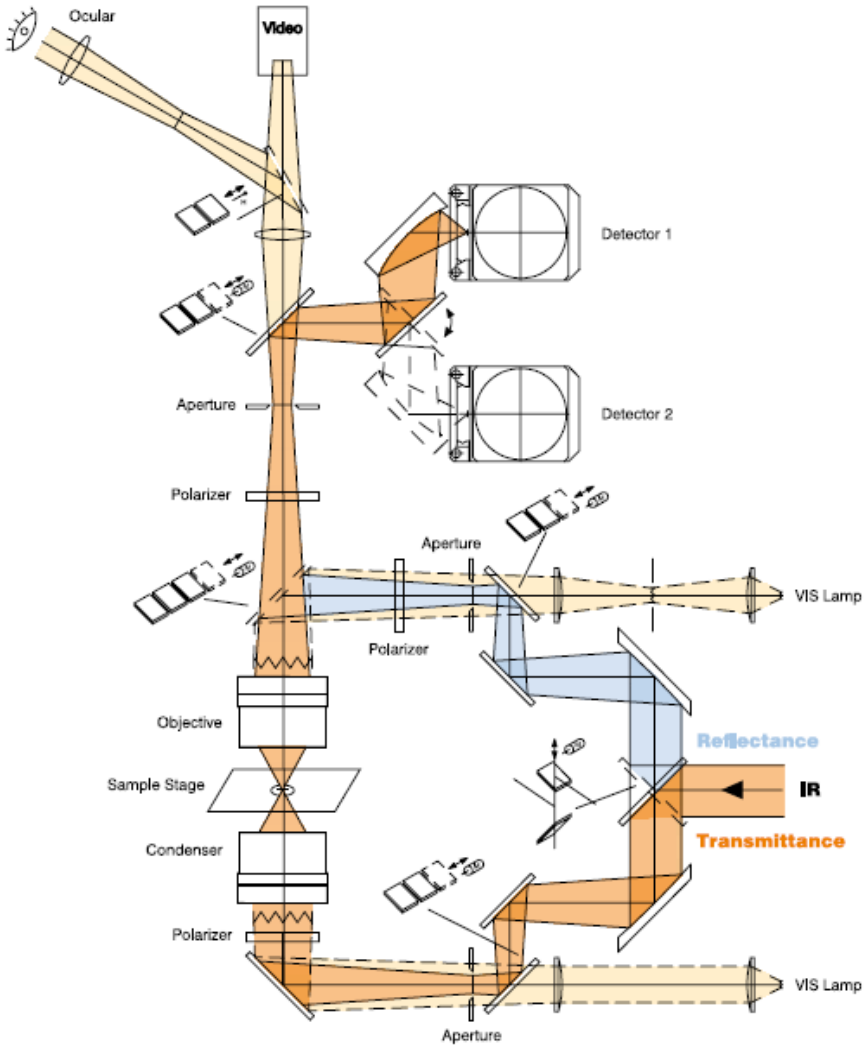

Figure 2.3: Schematic of a Bruker infrared microscope [57].

2.2.3 Angle Resolved MIR Reflection

Angle-dependent reflection spectroscopy was performed on a custom-built experimental setup externally coupled to the Bruker v70 FTIR. Broadband MIR light from the FTIR's internal source was focused on the sample using an 8" ZnSe lens, in order to narrow the solid angle of the incident light and thus improve angular resolution. The incident light was passed through a MIR wire grid polarizer to allow for measurement of both s- and p-polarized reflection. The sample was rotated about its vertical axis, and the collection optics and external MCT detector were mounted to a rail, which also rotated around the vertical axis of the sample. The collection optics consisted of a

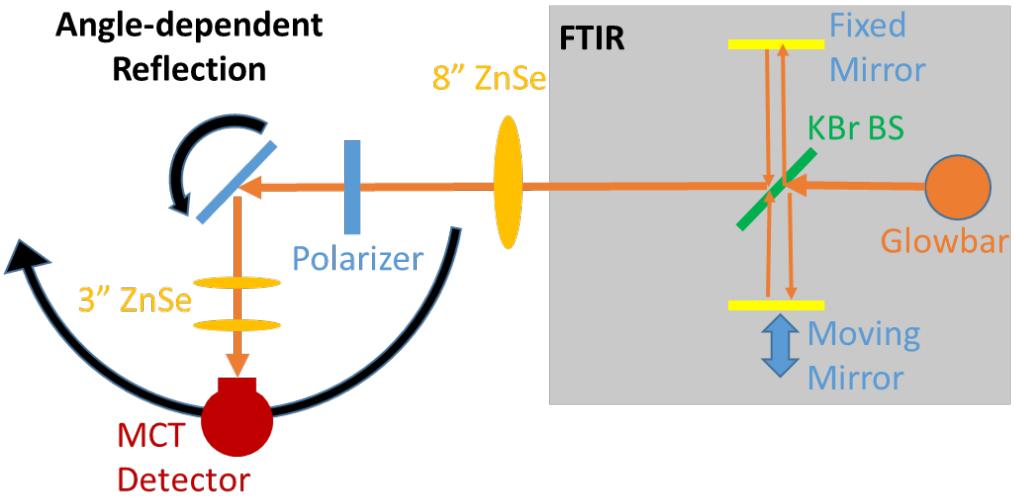

Figure 2.4: Schematic of custom experimental setup for measuring angle resolved MIR reflection spectra.

pair of 3" ZnSe lenses arranged to collect, collimate and focus the reflected light onto the MCT detector. The setup was designed to accurately measure polarization-dependent reflection at angles of 10° – 60° from normal incidence across the entire range of the MIR. A schematic of this experimental setup is depicted in Figure 2.4.

For each angle of incidence, the measured signal was maximized by fine adjustment of the stage-mounted detector position. This adjustment was made for measurements of both the gold reference and samples under investigation as they could not be easily interchanged on the sample holder due to subtle variations in the tilt of the mounted samples. These subtle variations in tilt necessitated carefully adjusting the detector alignment for each measurement. Background measurements were not taken before normalizing the reflection spectra as the strength of the reflected light far exceeded the background signal.

2.2.4 Angle Resolved FIR Reflection

The Pike VeeMax III variable reflection apparatus (heretofore known as "VeeMax") operates in a manor that is very similar to that of the Pike 10Spec fixed angle reflection apparatus. The VeeMax fits into a locked position within the sample compartment of the Bruker FTIR spectrometer, which

is more suitable for FIR spectroscopy than custom external setups due to reduced atmospheric absorption within the purged or evacuated FTIR and the otherwise unavailable use of the internally mounted DTGS detector. The key distinction between the VeeMax and the 10Spec is that the VeeMax can continuously vary the angle of incidence from 30° to 80° by turning a knob on the outside of the instrument. A schematic of the VeeMax is shown in Figure 2.5 [58]. The VeeMax has a pair of flat mirrors at its input and output ports for coupling light into and out of the instrument, as well as two pairs of 45° flat mirrors in the center of the instrument. The bottom pair of 45° mirrors is fixed, while the top pair can be raised and lowered by the external knob. The height of this pair of mirrors changes the angle of incidence upon a pair of curved mirrors, which direct/collect the light toward/from the sample with a near uniform angle of incidence upon the surface of the sample. Similar care should be taken when placing the sample over the aperture as with the 10Spec (see Section 2.2.1). A background measurement is likely to be required when measuring FIR reflection spectra. As with the 10Spec, polarization selectivity is accomplished by placing an infrared wire grid polarizer into the optical path within the sample chamber.

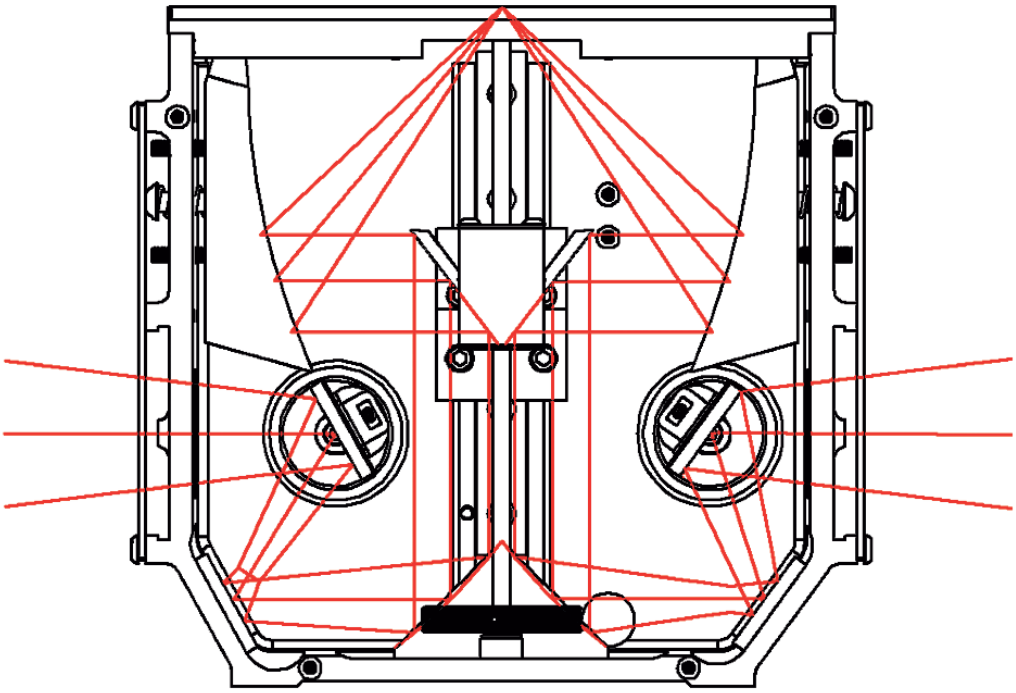

Figure 2.5: Schematic of Pike VeeMAX III variable reflection apparatus [58].

2.3 Infrared Emission Spectroscopy

2.3.1 Thermal Emission in the MIR

MIR thermal emission spectra were measured by mounting samples on a small, custom copper hot plate via melted indium paste. The copper plate was heated by a pair of cartridge heaters inserted into cylindrical slots on each side of the copper plate. Good thermal conduction between the cartridge heaters and the copper plate was ensured by inserting melted indium paste into the cylindrical slots. The temperature of the hot plate was maintained by attaching the cartridge heaters in parallel to a temperature controller with feedback from a thermocouple attached to the front of the copper plate. The hot plate was mounted on a post and attached to a rotational base so that the angle of emission could be varied as needed. The emitted light was spatially filtered by a pair of circular apertures and focused into the FTIR input window using a 5" ZnSe lens. A ZnSe wire grid polarizer was placed in front of the input window to select between s- and p-polarized light. A schematic of the experimental setup to measure MIR thermal emission is shown in Figure 2.6.

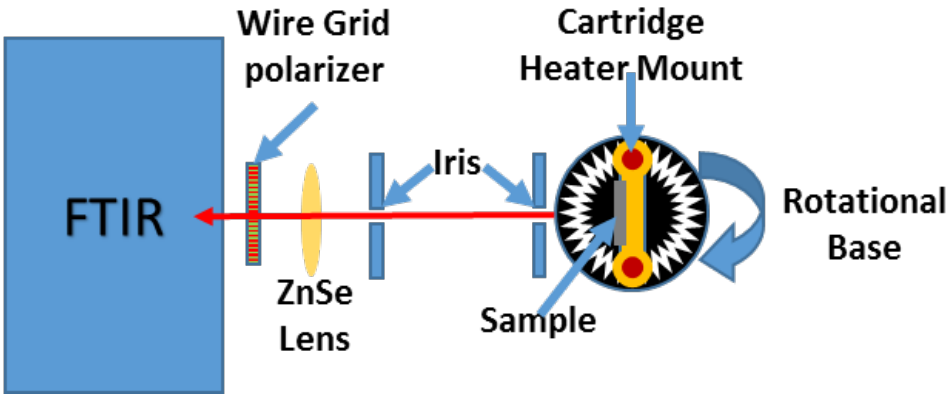

Figure 2.6: Schematic of MIR thermal emission spectroscopy experiment.

2.3.2 Thermal Emission in the FIR

FIR thermal emission spectra were measured by mounting the samples on a hot plate held at a constant temperature by a temperature control unit

with feedback from a thermocouple attached to the hot plate surface. The sample was mounted to the hot plate via a clip integrated into the hot plate's front surface. The hot plate was mounted on a rotational base with the rotational axis aligned to the front surface of the sample to permit optional variation of the angle of emission. The emitted thermal radiation was spatially filtered with a vertical slit or circular aperture and directed toward a flat gold mirror set at a 45° angle between the sample and a gold off-axis parabolic mirror. The parabolic mirror focused the collected thermal radiation into the collection optics of the Bruker v80v FTIR spectrometer. Polarization selectivity was accomplished by placing a FIR KRS-5 wire grid polarizer in front of the FTIR's input port. A schematic of the thermal emission setup is depicted in Figure 2.7.

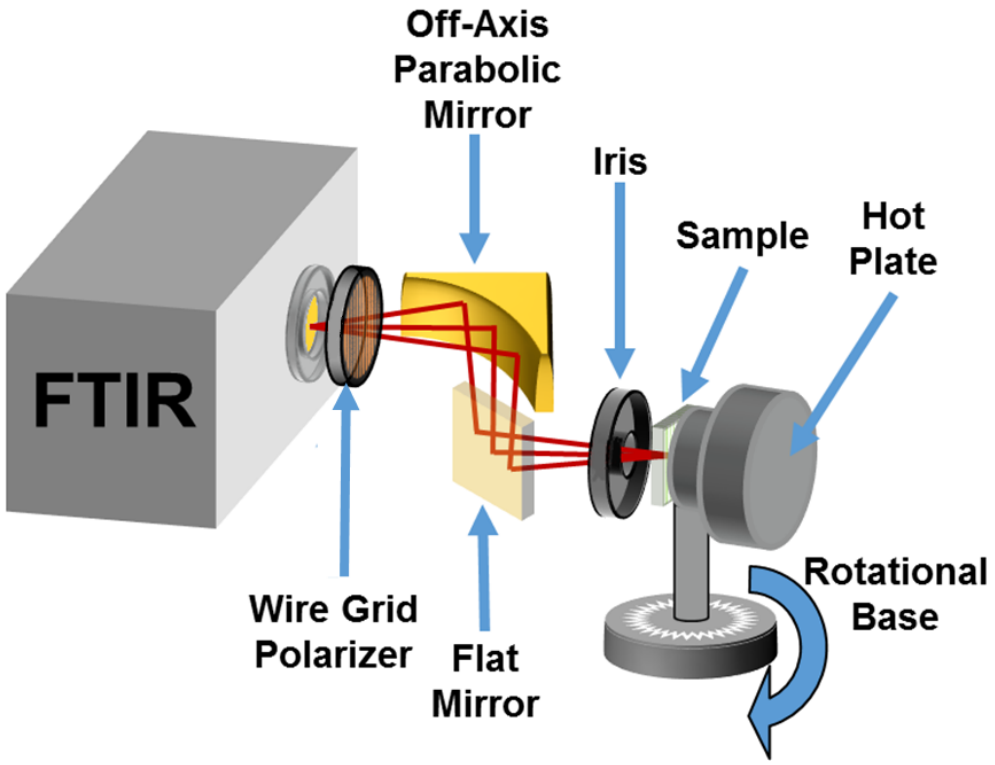

Figure 2.7: Schematic of FIR thermal emission experiment.

Background thermal emission spectra were taken from a covered input port of the FTIR and subtracted from the thermal emission spectra of the sample and the reference. Emissivity was determined by normalizing the sample spectra to those of a reference held at the same temperature: either an Omega BB703 calibrated blackbody source or a graybody source of known emissivity.

The graybody source was a custom-made sample of "black soot" deposited atop a metal ground plane and is described in more detail in Section 4.4.

Due to the lower specific detectivity of the DTGS detector and low radiative power output of thermal sources in the FIR, the light emitted by the samples often hovered barely above the background signal present in the system. One means of improving the signal was to enclose the experimental setup in a plastic tent, which was subsequently purged with dry nitrogen gas. Purging the optical path of the experiment with inert gas significantly reduced losses due to atmospheric absorption of infrared light. At longer wavelengths ($\lambda > 30\ \mu m$), the FTIR input/output port windows are no longer adequately transparent. In this case, the FTIR was vented with the relevant input port window removed. An unused port was replaced by a custom port fitted with a brass NPT coupler and quick connect fitting for 1/4" pneumatic tubing. This tubing was connected to a dry nitrogen supply, which purged the entire FTIR sample and instrument chambers.

2.4 Transfer Matrix Method

The transfer matrix method (TMM) is a means of calculating the transmission and reflection spectra of a series of optical materials with known thickness and optical properties expressed as the complex refractive index (n_i). TMM is commonly described in fundamental texts on Optics [59] and is quite simple to implement using a variety of popular scripting languages, of which we chose MATLAB. The method casts both the interaction of light at interfaces classically described by Fresnel's equations and the propagation of light through a material as linear transformations represented as 2×2 matrices (I_{ij} and L_j, respectively). The product of all of the matrices, the S-matrix (S), describes the reflection and transmission coefficients of the entire system Equation 2.1.

$$[S] = [I_{12}] \times [L_2] \times [I_{23}] \times [L_3] \ldots \times \left[I_{n-1,n}\right] \times [L_n] \tag{2.1}$$

The interface transfer matrix and the propagation transfer matrix are shown in Equations 2.4. The interface transfer matrix has two forms, one for each of the s- and p-polarizations of light. The coefficients r_s, t_s, r_p, t_p, are the reflection

and transmission field amplitude coefficients from Fresnel's equations (2.2) for both s- and p-polarizations. The angles θ_1 and θ_2 are the incident and transmitted (i.e. refracted) angles, respectively. The transmitted angle is determined from Snell's law (Equation 2.3). The phase (ϕ) in the propagation transfer matrix is shown in Equation 2.5, and it depends on the free-space wavenumber (k_0), the thickness of the layer (d), the complex refractive index of the layer (n), and the transmitted angle (θ_2).

$$\begin{aligned} r_p &= \frac{n_2 cos\theta_1 - n_1 cos\theta_2}{n_2 cos\theta_1 + n_1 cos\theta_2} \quad t_p = \frac{2n_1 cos\theta_1}{n_1 cos\theta_2 + n_2 cos\theta_1} \\ r_s &= \frac{n_1 cos\theta_1 - n_2 cos\theta_2}{n_1 cos\theta_1 + n_2 cos\theta_2} \quad t_s = \frac{2n_1 cos\theta_1}{n_1 cos\theta_1 + n_2 cos\theta_2} \end{aligned} \tag{2.2}$$

$$\theta_2 = sin^{-1}\left(\frac{n_1}{n_2} sin\theta_1\right) \tag{2.3}$$

$$L_j = \begin{bmatrix} e^{-i\phi} & 0 \\ 0 & e^{i\phi} \end{bmatrix}, \quad I_s = \begin{bmatrix} \frac{1}{t_s} & \frac{r_s}{t_s} \\ \frac{r_s}{t_s} & \frac{1}{t_s} \end{bmatrix}, \quad I_p = \begin{bmatrix} \frac{1}{t_p} & \frac{r_p}{t_p} \\ \frac{r_p}{t_p} & \frac{1}{t_p} \end{bmatrix} \tag{2.4}$$

$$\phi = \frac{k_0 dn}{cos\theta_2} \tag{2.5}$$

Finally, the transmission and reflection field coefficients for the entire system can be extracted from the elements of the 2 $\times$ 2 S-matrix as shown in Equation 2.6, and the total reflected and transmitted power coefficients can be determined from Equation 2.7 where n_n, n_1 are the complex refractive index of the last and first layers, respectively. As there are two forms of the interface transfer matrix, there will also be two forms of the S-matrix — one for each polarization of light. Any single computation of TMM will return the system's reflection and transmission coefficients for a given wavelength of light, but it is a simple matter to compute multiple wavelengths in a loop in order to produce reflection and transmission spectra.

$$r_{s,p} = S_{s,2(21)}/S_{s,2(11)}, \quad t_{s,p} = 1/S_{s,2(11)} \tag{2.6}$$

$$R_{s,p} = \left|r_{s,p}\right|^2, \quad T_{s,p} = \frac{n_n}{n_1}\left|t_{s,p}\right|^2 \tag{2.7}$$

2.5 Rigorous Coupled Wave Analysis

Most of the structures investigated in this dissertation and their preliminary designs were modeled using the numerical method known as rigorous coupled wave analysis (RCWA) using a MATLAB implementation of the method provided by the research group of Viktor Podolskiy and his student Christopher Roberts at the University of Massachusetts-Lowell [60]. This technique, which was first introduced for one-dimensional gratings [61] and further expanded to accommodate two-dimensional gratings [62], is ideal for modeling the optical properties of periodic, layered material systems such as the samples investigated in this dissertation. The formulation of the method will be outlined following the nomenclature and approach presented in the computational electromagnetics lecture series from Professor Raymond Rumpf at the University of Texas-El Paso [63].

The first step in the formulation of the RCWA method is to transform the spatial differential form of Maxwell's equations (Equations 2.8), where the magnetic field has been normalized by the characteristic wave impedance (Equation 2.9), into Fourier space (Equation 2.10) and expressed in matrix form.

$$\begin{aligned}
\frac{\partial E_z}{\partial y} - \frac{\partial E_y}{\partial z} &= k_0\mu_r\tilde{H}_x & \frac{\partial \tilde{H}_z}{\partial y} - \frac{\partial \tilde{H}_y}{\partial z} &= k_0\epsilon_r E_x \\
\frac{\partial E_x}{\partial z} - \frac{\partial E_z}{\partial x} &= k_0\mu_r\tilde{H}_y & \frac{\partial \tilde{H}_x}{\partial z} - \frac{\partial \tilde{H}_z}{\partial x} &= k_0\epsilon_r E_y \\
\frac{\partial E_y}{\partial x} - \frac{\partial E_x}{\partial y} &= k_0\mu_r\tilde{H}_z & \frac{\partial \tilde{H}_y}{\partial x} - \frac{\partial \tilde{H}_x}{\partial y} &= k_0\epsilon_r E_z
\end{aligned} \tag{2.8}$$

$$\tilde{H} = -j\sqrt{\frac{\mu_0}{\epsilon_0}}\vec{H}_x \tag{2.9}$$

Each component of the electric ($\boldsymbol{s}$) and magnetic ($\boldsymbol{u}$) fields is represented as a column vector. Each element of the field column vectors corresponds to a single harmonic order. Each transverse component of the wavevector for each harmonic order is normalized by the freepace wavevector (k_0) and arranged

as a sparse diagonal matrix ($\tilde{\boldsymbol{K}}_x$ and $\tilde{\boldsymbol{K}}_y$) with dimensions each equal to the total number of harmonic orders. Likewise, the z-coordinate is normalized by the freepace wavevector (k_0) and expressed as $\tilde{z}$. The spatial distributions of the permittivity and permeability within a unit cell have been transformed into their corresponding convolution matrices in Fourier space and expressed as $[\![\epsilon_r]\!]$ and $[\![\mu_r]\!]$, which are square matrices with dimensions equal to the total number of harmonic orders.

$$\begin{aligned} -j\tilde{\boldsymbol{K}}_y\boldsymbol{u}_z - \frac{\mathrm{d}}{\mathrm{d}\tilde{z}}\boldsymbol{u}_y &= [\![\epsilon_r]\!]\boldsymbol{s}_x & -j\tilde{\boldsymbol{K}}_y\boldsymbol{s}_z - \frac{\mathrm{d}}{\mathrm{d}\tilde{z}}\boldsymbol{s}_y &= [\![\mu_r]\!]\boldsymbol{u}_x \\ \frac{\mathrm{d}}{\mathrm{d}\tilde{z}}\boldsymbol{u}_x + j\tilde{\boldsymbol{K}}_x\boldsymbol{u}_z &= [\![\epsilon_r]\!]\boldsymbol{s}_y & \frac{\mathrm{d}}{\mathrm{d}\tilde{z}}\boldsymbol{s}_x + j\tilde{\boldsymbol{K}}_x\boldsymbol{s}_z &= [\![\mu_r]\!]\boldsymbol{u}_y \\ \tilde{\boldsymbol{K}}_x\boldsymbol{u}_y - \tilde{\boldsymbol{K}}_y\boldsymbol{u}_x &= j[\![\epsilon_r]\!]\boldsymbol{s}_z & \tilde{\boldsymbol{K}}_x\boldsymbol{s}_y - \tilde{\boldsymbol{K}}_y\boldsymbol{s}_x &= j[\![\mu_r]\!]\boldsymbol{u}_z \end{aligned} \tag{2.10}$$

Solving for the $\tilde{z}$-component of each field, substituting into the four remaining equations to eliminate the $\tilde{z}$-component, and solving for the derivative with respect to $\tilde{z}$ results in Equations 2.11.

$$\begin{aligned} \frac{\mathrm{d}}{\mathrm{d}\tilde{z}}\boldsymbol{u}_x &= \tilde{\boldsymbol{K}}_x[\![\mu_r]\!]^{-1}\tilde{\boldsymbol{K}}_y\boldsymbol{s}_x + ([\![\epsilon_r]\!] - \tilde{\boldsymbol{K}}_x[\![\mu_r]\!]^{-1}\tilde{\boldsymbol{K}}_x)\boldsymbol{s}_y \\ \frac{\mathrm{d}}{\mathrm{d}\tilde{z}}\boldsymbol{u}_y &= (\tilde{\boldsymbol{K}}_y[\![\mu_r]\!]^{-1}\tilde{\boldsymbol{K}}_y - [\![\epsilon_r]\!])\boldsymbol{s}_x - \tilde{\boldsymbol{K}}_y[\![\mu_r]\!]^{-1}\tilde{\boldsymbol{K}}_x\boldsymbol{s}_y \\ \frac{\mathrm{d}}{\mathrm{d}\tilde{z}}\boldsymbol{s}_x &= \tilde{\boldsymbol{K}}_x[\![\epsilon_r]\!]^{-1}\tilde{\boldsymbol{K}}_y\boldsymbol{u}_x + ([\![\mu_r]\!] - \tilde{\boldsymbol{K}}_x[\![\epsilon_r]\!]^{-1}\tilde{\boldsymbol{K}}_x)\boldsymbol{u}_y \\ \frac{\mathrm{d}}{\mathrm{d}\tilde{z}}\boldsymbol{s}_y &= (\tilde{\boldsymbol{K}}_y[\![\epsilon_r]\!]^{-1}\tilde{\boldsymbol{K}}_y - [\![\mu_r]\!])\boldsymbol{u}_x - \tilde{\boldsymbol{K}}_y[\![\epsilon_r]\!]^{-1}\tilde{\boldsymbol{K}}_x\boldsymbol{u}_y \end{aligned} \tag{2.11}$$

Equations 2.11 can be expressed in block matrix form as in Equations 2.12. The transverse components (x and y) of the electric and magnetic fields are expressed as a single column vector of column vectors. The normalized wave vectors for each component and harmonic order ($\tilde{\boldsymbol{K}}_x$ and $\tilde{\boldsymbol{K}}_y$) and the convolution matrices of the permittivity and permeability($[\![\epsilon_r]\!]$ and $[\![\mu_r]\!]$) form expressions, which are the elements of a single 2×2 matrix ($\boldsymbol{Q}$ and $\boldsymbol{P}$) wherein each element is a square matrix, with dimension equal to the total number of harmonic orders.

$$\frac{\mathrm{d}}{\mathrm{d}\tilde{z}}\begin{bmatrix}\boldsymbol{u}_x\\ \boldsymbol{u}_y\end{bmatrix} = \boldsymbol{Q}\begin{bmatrix}\boldsymbol{s}_x\\ \boldsymbol{s}_y\end{bmatrix}, \quad \boldsymbol{Q} = \begin{bmatrix}\tilde{\boldsymbol{K}}_x[\![\mu_r]\!]^{-1}\tilde{\boldsymbol{K}}_y & [\![\epsilon_r]\!] - \tilde{\boldsymbol{K}}_x[\![\mu_r]\!]^{-1}\tilde{\boldsymbol{K}}_x\\ \tilde{\boldsymbol{K}}_y[\![\mu_r]\!]^{-1}\tilde{\boldsymbol{K}}_y - [\![\epsilon_r]\!] & -\tilde{\boldsymbol{K}}_y[\![\mu_r]\!]^{-1}\tilde{\boldsymbol{K}}_x\end{bmatrix}$$
$$\frac{\mathrm{d}}{\mathrm{d}\tilde{z}}\begin{bmatrix}\boldsymbol{s}_x\\ \boldsymbol{s}_y\end{bmatrix} = \boldsymbol{P}\begin{bmatrix}\boldsymbol{u}_x\\ \boldsymbol{u}_y\end{bmatrix}, \quad \boldsymbol{P} = \begin{bmatrix}\tilde{\boldsymbol{K}}_x[\![\epsilon_r]\!]^{-1}\tilde{\boldsymbol{K}}_{\boldsymbol{y}} & [\![\mu_r]\!] - \tilde{\boldsymbol{K}}_x[\![\epsilon_r]\!]^{-1}\tilde{\boldsymbol{K}}_x\\ \tilde{\boldsymbol{K}}_y[\![\epsilon_r]\!]^{-1}\tilde{\boldsymbol{K}}_y - [\![\mu_r]\!] & -\tilde{\boldsymbol{K}}_y[\![\epsilon_r]\!]^{-1}\tilde{\boldsymbol{K}}_x\end{bmatrix} \tag{2.12}$$

The compact form on the left side of Equations 2.12 allows for easy derivation of the matrix form of the wave equation shown in Equation 2.13 for the electric field. The wave equation is simplified further in Equation 2.14.

$$\frac{\mathrm{d}^2}{\mathrm{d}\tilde{z}^2}\begin{bmatrix}\boldsymbol{s}_x\\ \boldsymbol{s}_y\end{bmatrix} = \boldsymbol{P}\frac{\mathrm{d}}{\mathrm{d}\tilde{z}}\begin{bmatrix}\boldsymbol{u}_x\\ \boldsymbol{u}_y\end{bmatrix} = \boldsymbol{P}\boldsymbol{Q}\begin{bmatrix}\boldsymbol{s}_x\\ \boldsymbol{s}_y\end{bmatrix} \tag{2.13}$$

$$\frac{\mathrm{d}^2}{\mathrm{d}\tilde{z}^2}\begin{bmatrix}\boldsymbol{s}_x\\ \boldsymbol{s}_y\end{bmatrix} - \boldsymbol{\Omega}^2\begin{bmatrix}\boldsymbol{s}_x\\ \boldsymbol{s}_y\end{bmatrix} = 0, \quad \boldsymbol{\Omega}^2 = \boldsymbol{P}\boldsymbol{Q} \tag{2.14}$$

Equation 2.14 can be easily recognized as a set of ordinary differential equations that can be solved as an eigenvalue problem. The general solution for the electric field in Equation 2.14 is shown in Equation 2.15, where $\boldsymbol{s}^+(0)$ and $\boldsymbol{s}^-(0)$ are the initial forward and backward propagating electric fields.

$$\begin{bmatrix}\boldsymbol{s}_x(\tilde{z})\\ \boldsymbol{s}_y(\tilde{z})\end{bmatrix} = e^{-\Omega\tilde{z}}\boldsymbol{s}^+(0) + e^{\Omega\tilde{z}}\boldsymbol{s}^-(0) \tag{2.15}$$

The solutions in Equation 2.15 can be cast as eigenvalues as shown in Equations 2.16 and 2.17, where $\boldsymbol{W}$ is the eigenvector matrix of $\boldsymbol{\Omega}^2$ and $\boldsymbol{\lambda}^2$ its eigenvalues.

$$e^{-\Omega\tilde{z}} = \boldsymbol{W}e^{-\lambda\tilde{z}}\boldsymbol{W}^{-1}, \quad e^{\Omega\tilde{z}} = \boldsymbol{W}e^{\lambda\tilde{z}}\boldsymbol{W}^{-1} \tag{2.16}$$

$$\begin{bmatrix}\boldsymbol{s}_x(\tilde{z})\\ \boldsymbol{s}_y(\tilde{z})\end{bmatrix} = \boldsymbol{W}e^{-\lambda\tilde{z}}\boldsymbol{c}^+ + \boldsymbol{W}e^{+\lambda\tilde{z}}\boldsymbol{c}^- \tag{2.17}$$

An analogous wave equation can be derived for the magnetic field with a different eigenvector matrix $\boldsymbol{V}$ as shown in Equation 2.18.

$$\begin{bmatrix}\boldsymbol{u}_x(\tilde{z})\\ \boldsymbol{u}_y(\tilde{z})\end{bmatrix} = \boldsymbol{V}e^{-\lambda\tilde{z}}\boldsymbol{c}^+ + \boldsymbol{V}e^{+\lambda\tilde{z}}\boldsymbol{c}^- \tag{2.18}$$

The relationship between $\boldsymbol{W}$ and $\boldsymbol{V}$ can be found by differentiating Equation 2.18 without respect to $\tilde{z}$ as shown in Equation 2.19. Comparing terms in Equations 2.12, 2.17 and 2.19 yields the relationship between the eigenvector matrices as shown in Equation 2.20.

$$\frac{\mathrm{d}}{\mathrm{d}\tilde{z}}\begin{bmatrix}\boldsymbol{u}_x(\tilde{z})\\ \boldsymbol{u}_y(\tilde{z})\end{bmatrix} = \boldsymbol{V}\boldsymbol{\lambda}e^{-\lambda\tilde{z}}\boldsymbol{c}^{+} + \boldsymbol{V}\boldsymbol{\lambda}e^{+\lambda\tilde{z}}\boldsymbol{c}^{-} \tag{2.19}$$

$$\boldsymbol{V} = \boldsymbol{Q}\boldsymbol{W}\boldsymbol{\lambda}^{-1} \tag{2.20}$$

Finally, the entire system, $\boldsymbol{\Psi}(\tilde{z})$, can be expressed as Equation 2.21.

$$\boldsymbol{\Psi}(\tilde{z}) = \begin{bmatrix}\boldsymbol{s}_x(\tilde{z})\\ \boldsymbol{s}_y(\tilde{z})\\ \boldsymbol{u}_x(\tilde{z})\\ \boldsymbol{u}_y(\tilde{z})\end{bmatrix} = \begin{bmatrix}\boldsymbol{W} & \boldsymbol{W}\\ -\boldsymbol{V} & \boldsymbol{V}\end{bmatrix}\begin{bmatrix}e^{-\lambda\tilde{z}} & \boldsymbol{0}\\ \boldsymbol{0} & e^{\lambda\tilde{z}}\end{bmatrix}\begin{bmatrix}\boldsymbol{c}^{+}\\ \boldsymbol{c}^{-}\end{bmatrix} \tag{2.21}$$

Equation 2.21 describes the solutions of the transverse electric and magnetic fields in a given layer with an inhomogeneous distribution of permittivity and permeability within the cross-section of its unit cell. The column matrix on the left side of Equation 2.21 represents the electric and magnetic transverse field components for each harmonic order. The first square matrix (with $\boldsymbol{W}$ and $\boldsymbol{V}$) on the right side of Equation 2.21 describes the shape of each harmonic mode, while the second matrix (with $e^{\pm\lambda\tilde{z}}$) describes how the modes propagate and decay/grow (with material loss/gain), while the final column matrix (with $\boldsymbol{c}_i^{\pm}$) describes the relative amplitudes of the the modes. The total spatial fields are a superposition of all of the harmonic modes.

The next step is to express the system in a multilayer framework using scattering matrices. Going forward, the process is completely analogous to the transfer matrix method. The key difference is that the permittivity and permeability of the inhomogeneous layers are expressed as discretized spatial distributions, which are then transformed into their corresponding convolutions matrices in Fourier space. If the permittivity and permeability were expressed as scalar quantities, as in homogeneous layers, the formulation would be identical to that of the transfer matrix method.

To formulate the scattering matrix of a multilayer system, each finite layer

is described by Equation 2.21 and assigned the index i as in Equation 2.22.

$$\boldsymbol{\Psi}_i(\tilde{z}) = \begin{bmatrix} \boldsymbol{s}_{x,i}(\tilde{z}) \\ \boldsymbol{s}_{y,i}(\tilde{z}) \\ \boldsymbol{u}_{x,i}(\tilde{z}) \\ \boldsymbol{u}_{y,i}(\tilde{z}) \end{bmatrix} = \begin{bmatrix} \boldsymbol{W}_i & \boldsymbol{W}_i \\ -\boldsymbol{V}_i & \boldsymbol{V}_i \end{bmatrix} \begin{bmatrix} e^{-\lambda\tilde{z}} & \boldsymbol{0} \\ \boldsymbol{0} & e^{\lambda\tilde{z}} \end{bmatrix} \begin{bmatrix} \boldsymbol{c}_i^+ \\ \boldsymbol{c}_i^- \end{bmatrix} \tag{2.22}$$

The boundary condition between the current layer (i) and the next layer $(i+1)$ is described by Equation 2.23, where the boundary interface occurs at $\tilde{z} = \tilde{z}_i$.

$$\begin{gathered} \boldsymbol{\Psi}_i(\tilde{z}_i) = \boldsymbol{\Psi}_{i+1}(\tilde{z}_i) \\ \begin{bmatrix} \boldsymbol{W}_i & \boldsymbol{W}_i \\ -\boldsymbol{V}_i & \boldsymbol{V}_i \end{bmatrix} \begin{bmatrix} e^{-\lambda_i\tilde{z}_i} & \boldsymbol{0} \\ \boldsymbol{0} & e^{\lambda_i\tilde{z}_i} \end{bmatrix} \begin{bmatrix} \boldsymbol{c}_i^+ \\ \boldsymbol{c}_i^- \end{bmatrix} = \begin{bmatrix} \boldsymbol{W}_{i+1} & \boldsymbol{W}_{i+1} \\ -\boldsymbol{V}_{i+1} & \boldsymbol{V}_{i+1} \end{bmatrix} \begin{bmatrix} \boldsymbol{c}_{i+1}^+ \\ \boldsymbol{c}_{i+1}^- \end{bmatrix} \end{gathered} \tag{2.23}$$

The i^{th} scattering matrix for each finite layer is constructed as a 2×2 symmetric matrix as in Equation 2.24.

$$\boldsymbol{S}^{(i)} = \begin{bmatrix} \boldsymbol{S}_{11}^{(i)} & \boldsymbol{S}_{12}^{(i)} \\ \boldsymbol{S}_{21}^{(i)} & \boldsymbol{S}_{22}^{(i)} \end{bmatrix} \tag{2.24}$$

The elements of the scattering matrix in Equation 2.24 are described by Equations 2.25, which are related to the electric and magnetic field eigenvector matrices, $\boldsymbol{W}$ and $\boldsymbol{V}$. The eigenvector matrices, $\boldsymbol{W_0}$ and $\boldsymbol{V_0}$ correspond to fictitious free space layers of zero thickness used to connect the layers in an interchangeable manner.

$$\begin{aligned} \boldsymbol{S}_{11}^{(i)} &= (\boldsymbol{A}_i - \boldsymbol{X}_i\boldsymbol{B}_i\boldsymbol{A}_i^{-1}\boldsymbol{X}_i\boldsymbol{B}_i)^{-1}(\boldsymbol{X}_i\boldsymbol{B}_i\boldsymbol{A}_i^{-1}\boldsymbol{X}_i\boldsymbol{A}_i - \boldsymbol{B}_i) \\ \boldsymbol{S}_{12}^{(i)} &= (\boldsymbol{A}_i - \boldsymbol{X}_i\boldsymbol{B}_i\boldsymbol{A}_i^{-1}\boldsymbol{X}_i\boldsymbol{B}_i)^{-1}\boldsymbol{X}_i(\boldsymbol{A}_i - \boldsymbol{B}_i\boldsymbol{A}_i^{-1}\boldsymbol{B}_i) \\ \boldsymbol{S}_{21}^{(i)} &= \boldsymbol{S}_{12}^{(i)} \\ \boldsymbol{S}_{22}^{(i)} &= \boldsymbol{S}_{11}^{(i)} \end{aligned} \tag{2.25}$$

$$\begin{aligned} \boldsymbol{A}_i &= \boldsymbol{W}_i^{-1}\boldsymbol{W}_0 + \boldsymbol{V}_i^{-1}\boldsymbol{V}_0 \\ \boldsymbol{B}_i &= \boldsymbol{W}_i^{-1}\boldsymbol{W}_0 - \boldsymbol{V}_i^{-1}\boldsymbol{V}_0 \\ \boldsymbol{X}_i &= e^{-\boldsymbol{\lambda}_i k_0 L_i} \end{aligned}$$

The scattering matrices for each finite layer are combined using the Redheffer star product ($\otimes$) to compute the device scattering matrix ($\boldsymbol{S}^{(device)}$) as in Equation 2.26.

$$\boldsymbol{S}^{(device)} = \boldsymbol{S}^{(1)} \otimes \boldsymbol{S}^{(2)} \otimes \cdots \otimes \boldsymbol{S}^{(n-1)} \otimes \boldsymbol{S}^{(n)} \tag{2.26}$$

A scattering matrix for the global system ($\boldsymbol{S}^{(global)}$) is then computed in Equation 2.27, which includes the scattering matrices for the superstrate ($\boldsymbol{S}^{(R)}$) and substrate ($\boldsymbol{S}^{(T)}$) regions (also known as the reflection and transmission regions).

$$\boldsymbol{S}^{(global)} = \boldsymbol{S}^{(R)} \otimes \boldsymbol{S}^{(device)} \otimes \boldsymbol{S}^{(T)} \tag{2.27}$$

The scattering matrix for the reflection region, ($\boldsymbol{S}^{(R)}$), has elements described by Equations 2.28.

$$\begin{aligned}
\boldsymbol{S}_{11}^{(R)} &= -\boldsymbol{A}_R^{-1}\boldsymbol{B}_R \\
\boldsymbol{S}_{12}^{(R)} &= 2\boldsymbol{A}_R^{-1} \\
\boldsymbol{S}_{21}^{(R)} &= \frac{1}{2}(\boldsymbol{A}_R - \boldsymbol{B}_R\boldsymbol{A}_R^{-1}\boldsymbol{B}_R) \\
\boldsymbol{S}_{22}^{(i)} &= \boldsymbol{B}_R\boldsymbol{A}_R^{-1}
\end{aligned} \tag{2.28}$$

$$\begin{aligned}
\boldsymbol{A}_R &= \boldsymbol{W}_0^{-1}\boldsymbol{W}_R + \boldsymbol{V}_0^{-1}\boldsymbol{V}_R \\
\boldsymbol{B}_R &= \boldsymbol{W}_0^{-1}\boldsymbol{W}_R - \boldsymbol{V}_0^{-1}\boldsymbol{V}_R
\end{aligned}$$

The scattering matrix for the transmission region, ($\boldsymbol{S}^{(T)}$), has elements described by Equations 2.29.

$$\begin{aligned}
\boldsymbol{S}_{11}^{(T)} &= \boldsymbol{B}_T\boldsymbol{A}_T^{-1} \\
\boldsymbol{S}_{12}^{(T)} &= \frac{1}{2}(\boldsymbol{A}_T - \boldsymbol{B}_T\boldsymbol{A}_T^{-1}\boldsymbol{B}_T) \\
\boldsymbol{S}_{21}^{(T)} &= 2\boldsymbol{A}_T^{-1} \\
\boldsymbol{S}_{22}^{(i)} &= -\boldsymbol{A}_T^{-1}\boldsymbol{B}_T
\end{aligned} \tag{2.29}$$

$$\begin{aligned}
\boldsymbol{A}_T &= \boldsymbol{W}_0^{-1}\boldsymbol{W}_T + \boldsymbol{V}_0^{-1}\boldsymbol{V}_T \\
\boldsymbol{B}_T &= \boldsymbol{W}_0^{-1}\boldsymbol{W}_T - \boldsymbol{V}_0^{-1}\boldsymbol{V}_T
\end{aligned}$$

The coefficients of the reflected ($\boldsymbol{c}_R$) and transmitted ($\boldsymbol{c}_T$) fields can be

determined from the elements of the global scattering matrix and the field coefficients of the incident field ($\boldsymbol{c}_I$) as shown in Equations 2.30.

$$\boldsymbol{c}_R = \boldsymbol{S}_{11}\boldsymbol{c}_I, \quad \boldsymbol{c}_T = \boldsymbol{S}_{21}\boldsymbol{c}_I \tag{2.30}$$

The transverse field components of the reflected ($\boldsymbol{r}_\perp$) and transmitted fields ($\boldsymbol{t}_\perp$) can be determined by Equations 2.31.

$$\begin{aligned} \boldsymbol{r}_\perp &= \begin{bmatrix} \boldsymbol{r}_x \\ \boldsymbol{r}_y \end{bmatrix} = \boldsymbol{S}_\perp^{(R)} = \boldsymbol{W}_R\boldsymbol{c}_R \\ \boldsymbol{t}_\perp &= \begin{bmatrix} \boldsymbol{t}_x \\ \boldsymbol{t}_y \end{bmatrix} = \boldsymbol{S}_\perp^{(T)} = \boldsymbol{W}_T\boldsymbol{c}_T \end{aligned} \tag{2.31}$$

The longitudinal components of the reflected ($\boldsymbol{r}_z$) and transmitted ($\boldsymbol{t}_z$) fields are calculated using Equations 2.32.

$$\begin{aligned} \boldsymbol{r}_z &= -\tilde{\boldsymbol{K}}_{z,R}^{-1}(\tilde{\boldsymbol{K}}_x\boldsymbol{r}_x + \tilde{\boldsymbol{K}}_y\boldsymbol{r}_y) \\ \boldsymbol{t}_z &= -\tilde{\boldsymbol{K}}_{z,T}^{-1}(\tilde{\boldsymbol{K}}_y\boldsymbol{t}_y + \tilde{\boldsymbol{K}}_y\boldsymbol{t}_y) \\ \tilde{\boldsymbol{K}}_{z,R} &= -(\sqrt{\mu_{r,R}\epsilon_{r,R}\boldsymbol{I} - \tilde{\boldsymbol{K}}_x^2 - \tilde{\boldsymbol{K}}_y^2})^* \\ \tilde{\boldsymbol{K}}_{z,T} &= -(\sqrt{\mu_{r,T}\epsilon_{r,T}\boldsymbol{I} - \tilde{\boldsymbol{K}}_x^2 - \tilde{\boldsymbol{K}}_y^2})^* \end{aligned} \tag{2.32}$$

Finally, the power in each mode for reflection and transmission can be found from Equations 2.33.

$$\begin{aligned} \boldsymbol{R} &= Re\left\{\frac{\tilde{\boldsymbol{K}}_{z,R}}{\tilde{k}_{z,I}}\right\} \cdot |\vec{\boldsymbol{r}}|^2 \\ \boldsymbol{T} &= Re\left\{\frac{\mu_{r,I}}{\mu_{r,T}}\frac{\tilde{\boldsymbol{K}}_{z,T}}{\tilde{k}_{z,I}}\right\} \cdot |\vec{\boldsymbol{t}}|^2 \\ |\vec{\boldsymbol{r}}|^2 &= |\boldsymbol{r}_x|^2 + |\boldsymbol{r}_y|^2 + |\boldsymbol{r}_z|^2 \\ |\vec{\boldsymbol{t}}|^2 &= |\boldsymbol{t}_x|^2 + |\boldsymbol{t}_y|^2 + |\boldsymbol{t}_z|^2 \end{aligned} \tag{2.33}$$

Chapter 3

Thin Film Perfect Absorbers

As mentioned in Section 1.3, the maturity of MIR technology serves as a convenient springboard for further exploration of FIR technologies while bearing in mind the challenges to heedlessly extrapolating such achievements to longer wavelengths as discussed in Section 1.5. In this chapter, we will discuss the first of several projects that seek to exploit selective thermal emission as an infrared light source, while eventually considering the limitations of this approach and additional alternatives.

According to Kirchhoff's law of thermal emission, altering a material's thermal emission is equivalent to altering that material's absorptivity. In other words, if a material has a strong or perfect absorption resonance, it should also exhibit strong selective thermal emission at the same wavelength. Previous work has demonstrated perfect absorption by means of top-layer patterning to design antennae, plasmonic, and meta-material resonances [64–67] in the microwave [64], MIR [65, 67–69], NIR [66], and visible regimes [70]. Such perfect absorbers operating in the MIR could find potential use in molecular sensors, as the local field is often strongly localized at the absorption resonance, which would enhance the sensitivity of such devices. Such devices have already been shown to be effective at detecting small shifts in refractive index due to adsorption of molecular species on the devices' top layer [66, 71]. Some designs for perfect absorbers can be extended to longer wavelengths in the FIR as described in later chapters.

This chapter contains experimental results and media that have been previously published in a scholarly journal: see [22]. OSA Publishing provides open access to this journal, and reprinting of material for this thesis is permitted under the fair use doctrine. Portions of this work were carried out by Dr. Stephanie Law, Tom Jacobs, Gino Rooney. Stephanie evaporated the germanium coatings, performed liftoff of pattern samples, conducted the preliminary optical characterization of the samples, and made important contributions to the modeling, analysis, and direction of the project. Tom Jacobs and Gino Rooney developed and carried out the process of doping the substrates, as well as conducting the initial optical characterization of this material.

In this chapter, we developed an engineered metal with a thin dielectric film that exhibits strong absorption and selective thermal emission. The engineered metal is a highly doped layer of silicon, which has been previously shown to have metallic optical properties in the MIR [20, 21]. Unlike those structures mentioned above, there is no need for any top layer patterning to achieve the desired absorption resonance. Instead these structures make use of a thin-film interference effect commonly used to design anti-reflection coatings. Such coatings typically employ a dielectric layer of one quarter wavelength thickness above a lossy ground plane. One of the earliest examples of such a device was employed as a RADAR anti-detection device known as the Salisbury screen [72], which made use of a lossy graphite layer suspended one quarter wavelength above a metal ground plane.

The perfect absorbers presented in this chapter utilize a well-known thin-film interference effect widely used to design anti-reflection coatings. Such coatings typically employ film thicknesses of one quarter of a wavelength, which can become unwieldy when operating at longer wavelengths. Our results demonstrate the control of optical properties of a material in such way as to significantly reduce the necessary thickness of the anti-reflection layer in our interference filters. Recent work from the Capasso group [73, 74] has demonstrated strong absorption using much thinner films in the visible wavelength range. In the first case, a sapphire substrate is coated with a temperature-dependent phase change material, vanadium dioxide. By tuning the temperature of the device through its phase-change temperature, the absorption of the device can also be tuned. The second example uses thin germanium films on substrates coated with optically thick gold. These thin-film structures are designed similarly to ours, but exhibit a strong reflection resonance in the visible spectrum. In the visible range, germanium is an absorbing dielectric, while in the MIR, germanium is transparent. Our samples replace the gold ground-plane with an engineered metal of highly doped silicon.

To compare these different thin-film structures, we simulated the normal incidence reflection versus film thickness in Figure 3.1, wherein the film thickness has been normalized by the incident wavelength and the real part of the film's refractive index. A typical sort of anti-reflection structure, such as the Salisbury screen previously mentioned, is depicted in the left panel (a). This structure has a low loss dielectric film on top of a perfect

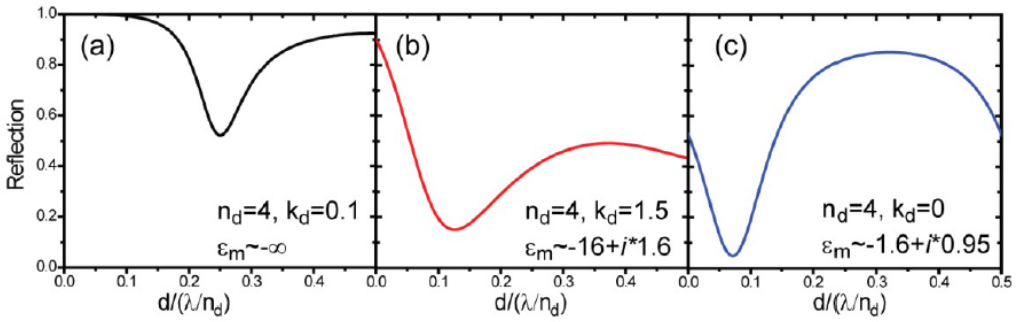

Figure 3.1: Simulated normal incidence reflection for various combinations of thin dielectric films on top of optically thick metal substrates as a function of dielectric thickness, which has been normalized by the incident wavelength and dielectric index. a) A high index, low loss dielectric on top of a perfect electrical conductor. The strongest absorption occurs at one quarter wavelength, but only reaches approximately 50%. b) A high index, lossy dielectric on top of a metal with finite conductivity. The strongest absorption resonance is obtained in a layer thinner than one quarter wavelength and is significantly higher 85%. c) A high index, lossless dielectric on top of an engineered metal with a plasma wavelength slightly shorter than the incident wavelength. The thickness at which the strongest absorption resonance occurs is less than one-tenth of a wavelength and the strength exceeds 95%. This final example most closely resembles the work presented.

.

electrical conductor. Its maximum absorption resonance occurs at one quarter wavelength, and it absorbs approximately 50% of the incident light. The middle panel (b) is most similar to the work by the Capasso group with a high index, lossy dielectric on top of ground plane with permittivity similar to that of gold in the visible regime. This structure has a maximum absorption resonance when the film is less than one quarter wavelength and its strength approaches 85%. The final panel on the right (c) depicts a structure similar to the one presented in this work. Here the dielectric is lossless with a high index, and it sits on a ground plane of engineered metal. The simulated permittivity at the surface of our engineered metal is described in Section 3.2. The real part of the permittivity crosses zero at $\lambda = 4.2$ µm, indicating the plasma frequency of the material. The engineered metal has a plasma wavelength slightly shorter than the incident wavelength. This means that the magnitude of the real part of the permittivity is small in comparison to that of a perfect electrical conductor or to noble metals, such as gold and silver, in the visible and longer wavelength ranges. Because the engineered

metal is a highly doped semiconductor, its doping can be used to control its plasma frequency, thus controlling its permittivity at a given wavelength. This control over the optical properties of the engineered metal allows one to optimize the strength of an absorption resonance at a given wavelength, while the position of the resonance is determined by the thickness of the dielectric film essentially decoupling the two parameters of the resonance. Such control over the design of perfect absorbers is not possible using traditional noble metals. Furthermore, the design and fabrication of the perfect absorbers presented here is much simpler and less expensive that the methods mentioned previously which require carefully designing and patterning a top metal layer.

3.1 Fabrication of Highly Doped Silicon

Our engineered metals were fabricated on silicon-on-insulator (SOI) substrates comprised of a thick (610 – 640 µm) poly-crystalline silicon handle, a buried oxide layer (0.9 – 1.1 µm), and an active layer of single-crystalline silicon (2 – 3 µm). These substrates were doped using P509 Filmtronix Spin-On Dopant (see Figure 3.2). The substrates were cleaned using a standard degrease procedure by rinsing the surface with acetone and isopropanol. After baking at 125 °C for 5 minutes to remove excess moisture from the surface, 0.5 mL of dopant were applied to the substrate and spun at 4000 RPM for 40 seconds. The spun-on dopant layer was then hard-baked at 200 °C for 12 minutes. The dopant was then driven into the active layer of the substrate using a conventional furnace at 1100 °C for two hours. Finally, the dopant layer was removed with an aqueous 1:1 hydrofluoric acid solution. This procedure left a clean surface and highly doped active silicon layer. After doping, the substrates were optically characterized using MIR reflection spectroscopy. The reflection spectra of un-doped (blue) and doped (red) substrates are shown in Figure 3.2a. In the un-doped case, Fabry-Perot oscillations are clearly present with a free spectral range of approximately 574 cm^{-1}, which is consistent with the manufacturer's specifications for the thickness of the active silicon layer and indicates that the un-doped layer is transparent. After doping, the Fabry-Perot oscillations are absent, indicating that the active layer is no longer transparent, but strongly absorbing and metallic at frequencies below 2000 cm^{-1}.

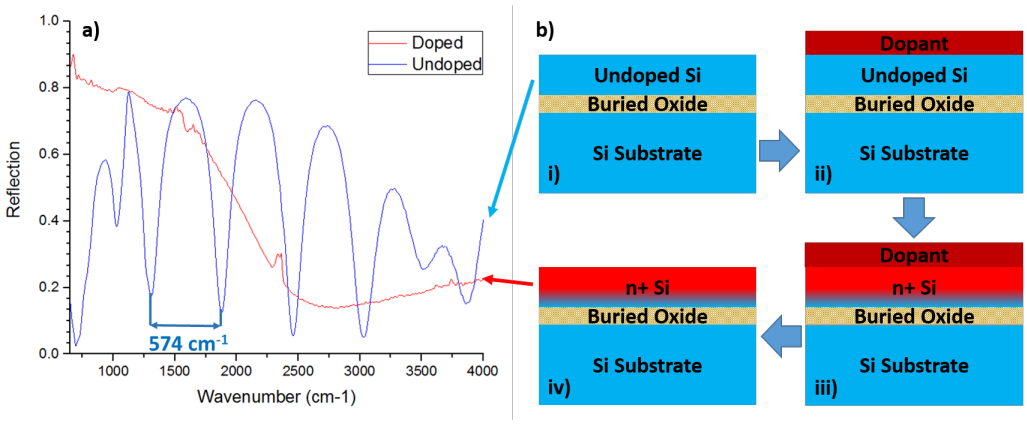

Figure 3.2: a) MIR reflection spectra for SOI substrates before and after doping process. b) The spin-on doping process. i) Undoped SOI wafer. Its reflection spectrum is shown in blue in a). ii) Application of spin-on dopant layer. iii) Driving in dopants in furnace. iv) Removal of dopant layer using hydrofluoric acid. Reflection spectra of the doped material are shown in red in a). The previously dielectric material is now strongly reflective at long wavelengths indicative of a metallic optical response. It is clear that the material has a plasma frequency somewhere near 2000 cm^{-1}.

The doped SOI wafers were then degreased and a thin germanium film was deposited by electron beam evaporation from a 99.99% germanium source at a rate of approximately 2 Å/s. The film thickness was monitored using a quartz crystal monitor and confirmed with a germanium-selective etch and profilometry. For our Ge-thickness studies, three evaporation runs of 82.5, 165, and 330 nm were performed and seven total samples were fabricated with thicknesses ranging from 82.5 nm to 577.5 nm in 82.5 nm steps. For patterned Ge samples standard lithographic and liftoff techniques were used.

3.2 Determination of Sample Permittivity

We first measured normal incidence reflection data using a Bruker IR-II infrared microscope coupled to a Bruker V80V Fourier transform infrared (FTIR) spectrometer. Even though our microscope was equipped with a high numerical aperture, gold Cassegrain-style lens, subsequent measurements revealed our thin-film absorbers to be highly insensitive to the angle of incidence. This indicates that our microscope measurements were a good approximation of a normal incidence reflection experiment, which is signifi-

cantly more difficult to perform as it requires the alignment of a beam-splitter along with the introduction of its additional dispersion. We used our normal incidence measurements taken both before and after doping (see Figure 3.2) to determine the sample permittivity as shown in Figure 3.3.

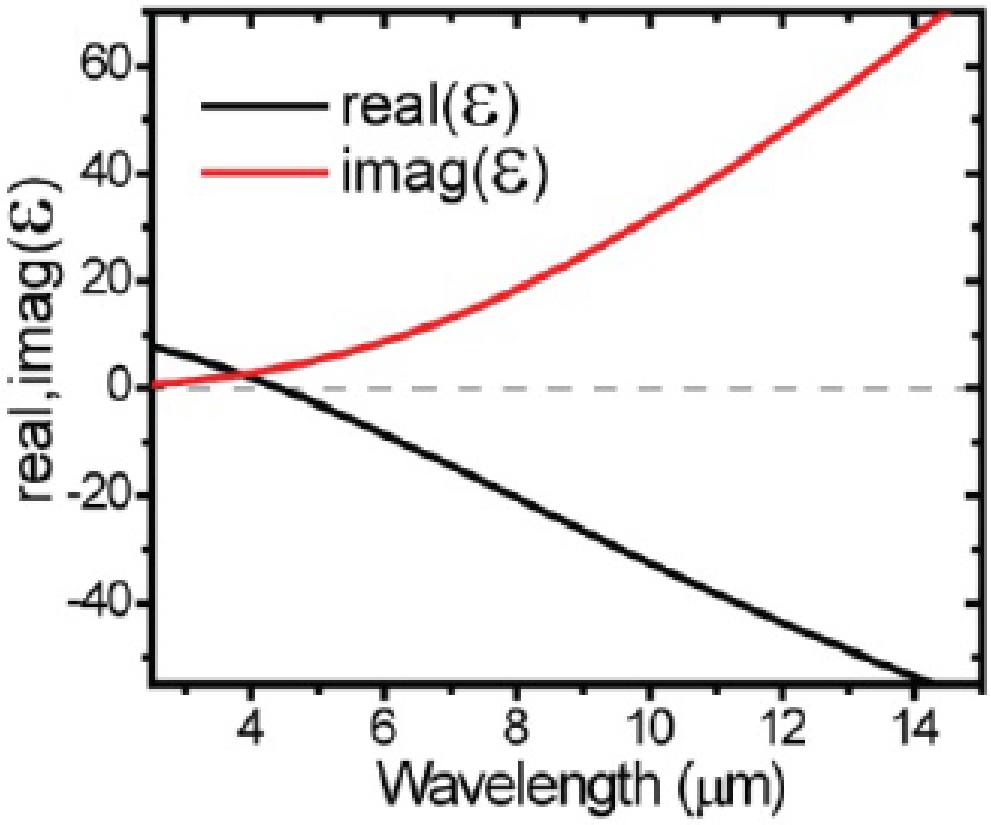

Figure 3.3: Calculated real (black) and imaginary (red) permittivity at the surface of our engineered metal made of highly doped silicon. The real part of the permittivity crosses zero near 4.2 µm, indicating the material's plasma wavelength.

We modeled the doping profile of our substrates using a complementary error function, which is the analytical solution to Fick's laws of diffusion for a fixed source near the surface of a material (Equation 3.1). We took the z-axis to be the direction of diffusion, disregarding lateral diffusion. The carrier concentration (n) depends on the position from the surface (z), the surface dopant concentration (C_s), and the diffusion length — or the square root of the product of the diffusivity (D) and the diffusion time (t). The diffusion length depends on the dose (Q), and the surface dopant centration (C_s). We determined the dose from Hall measurements to be approximately 50×10^{16}

cm^{-2} and used the surface dopant concentration as a fitting parameter along with the electron scattering time.

$$n(z) = C_s \left[erfc(\frac{z}{\sqrt{(Dt)}}) \right], \quad \sqrt{(Dt)} = \frac{Q\sqrt{\pi}}{2C_s} \tag{3.1}$$

The Drude model is used to model the permittivity of free electron gases, and is widely used to calculate the optical properties of metals at long wavelengths [50]. The Drude model depends on two material-specific parameters: the plasma frequency ω_p and the electron scattering rate γ (Equation 3.2). The plasma frequency depends on the carrier concentration (n), the material's effective electron mass (m^*), the material's dielectric constant (ϵ_s), the fundamental electron charge (e), and the vacuum permittivity (ϵ_0). The plasma frequency indicates the frequency at which the real part of a metal's permittivity changes sign. At frequencies above the plasma frequency, the real part of a material's permittivity is positive and indicative of a dielectric optical response, while at frequencies below the plasma frequency, the real part is negative and indicative of a metallic response. The scattering rate characterizes the total effect of all electron scattering mechanisms and accounts for free electron absorption. It is typical that the scattering rate is determined by fitting the Drude model to experimental data.

$$\epsilon = \epsilon_s \frac{\omega_p^2}{\omega^2 - i\omega\gamma}, \quad \omega_p^2 = \frac{ne^2}{\epsilon_0 \epsilon_s m^*} \tag{3.2}$$

In most cases, the carrier concentration can be easily determined by a variety of techniques, while the material's effective mass and dielectric constant are often well known in the literature. In this chapter, we took the dielectric constant of silicon to be 11.8, and the effective mass to be 0.28 times the mass of a free electron. The carrier concentration was determined by modeling the doping profile using Fick's law of diffusion.

Our structures were modeled using a 1D transmission matrix (T-matrix) formalism. The samples are broken into layers of thickness d_i, with a complex refractive index, $\tilde{n_i}$ and a complex transmission angle $\tilde{\theta_i}$ (calculated from Snell's law) assigned to each layer. The transfer matrix I_{ij} is determined for each interface of the structure (between layers i and j), as well as the transfer

matrix L_i for propagation through the i^{th} layer. The total reflection and transmission through the system can be extracted from matrix product of all of the layers' and interfaces' T-matrices, as described in Section 2.4. The doping profile of our samples is estimated assuming a constant surface concentration of dopants (provided by the spin-on dopant coating) and a diffusion coefficient for phosphorus atoms in Si. From this, the distribution of dopants in our material is expected to follow a complementary error function (erfc) profile as a function of depth (z) in accordance with Fick's law of diffusion. The Drude model can be applied to these films [50], resulting in only the surface doping concentration and scattering time as adjustable parameters. Using a doping-independent scattering rate in our material allows for the determination of the material's plasma frequency, and thus the material's complex permittivity as a function of depth. For the samples used in this work, little variation in plasma wavelength is expected over the thickness of the active Si layer, an expectation verified by reflection measurements on doped active Si layers etched to varying depths. This sample was modeled with a surface plasma wavelength of 4.2 µm. At longer wavelengths ($\lambda_0 > 3$ µm), the doped active Si is either highly absorbing or highly reflective, and little to no light reaches the buried oxide, making the SOI wafer functionally equivalent to a heavily doped Si wafer. Thus we can treat our system as an infinitely thick doped-Si wafer with a doping profile described by a complementary error function. Choice of only the surface dopant concentration and a constant scattering time allows for accurate fitting to our experimental data. The parameters used to fit the experimental data for the uncoated sample are then held constant throughout our modeling of the subsequently Ge-coated samples. For the Ge-coated samples, the Ge was treated as a lossless dielectric with $n_{Ge} = 4$.

3.3 Angle-Resolved Reflectivity of Germanium-Coated Samples

Normal incidence measurements using a Bruker IR-II infrared microscope were used to determine the dependence of the absorption resonances versus the thickness of the thin germanium films including the reflection data of the uncoated highly-doped silicon samples. Experimental (a) and modeled (b) results are depicted in Figure 3.4. The reflection spectra of our samples show

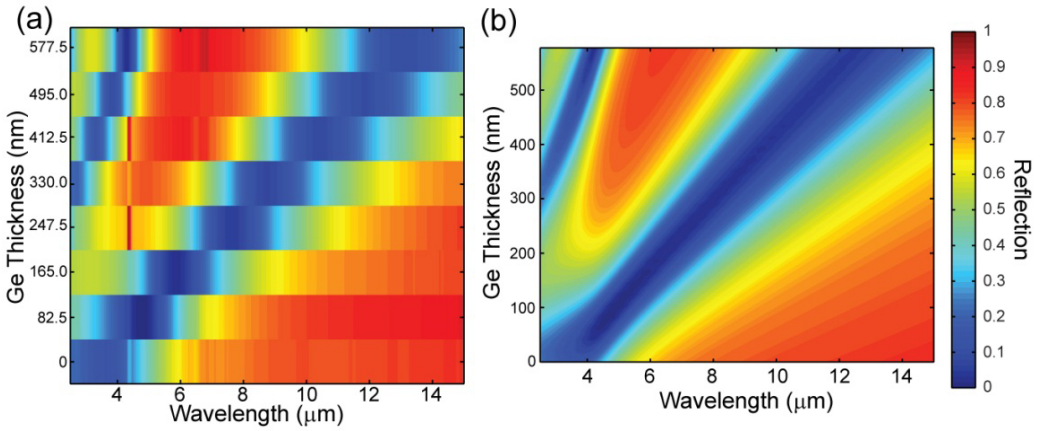

Figure 3.4: Reflection spectra for our thin-film perfect absorbers. a) Experimental results. b) Simulated results. The reflection spectra are compared with the thickness of the germanium films showing that the perfect absorption resonances scale to longer wavelengths with thicker germanium films.

strong dips at resonant wavelengths, which scale to longer wavelengths for thicker germanium layers. As our samples did not show any transmission in the same wavelength range, nor is there any patterning to scatter the incident light, these dips in reflection can be attributed to absorption in our samples.

In most cases, these absorption resonances exceed 95%, approaching 99%. The anomalous features in the experimental data that appear near 4 μm for the 247.5 nm and 412.5 nm samples are artifacts introduced by atmospheric absorption. Otherwise, our experimental and simulated results show excellent agreement. It is important to note the thickness of our germanium films versus the wavelength of the absorption resonances. Typical thin-film interference effects predict minimal reflection at a given wavelength using a film thickness of one quarter wavelength, while also accounting for the refractive index of the film material.

Our thin germaniums are films are significantly less than the corresponding quarter-wavelength thickness. This fact is depicted in Figure 3.5 where we have plotted on the left (blue) axis a scaling factor that divides the quarter-wavelength thickness of the observed resonance by the actual thickness of our ultra-thin germanium films. In each case, our samples show a scaling factor that exceeds unity (blue dots).

We also modeled our scaling factor revealing the trend that our scaling factor increases as we approach the plasma wavelength of our highly doped silicon, but that the scaling factor approaches one at longer wavelengths as would

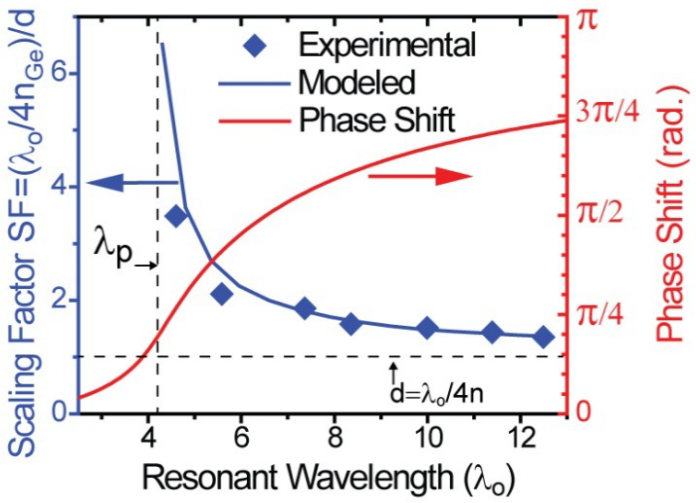

Figure 3.5: Comparison of the germanium thickness to the quarter-wavelength thickness of the corresponding absorption resonance (left, blue). The scaling factor is the quarter wavelength thickness divided by the actual thickness and shown for each sample (diamonds) as well as calculated (line). The calculated phase shift (right, red line) at the interface of the germanium and engineered metal. The phase shift is minimal and less than π near the plasma wavelength of the engineered metal, but approaches π again at longer wavelengths far from the plasma wavelength. The non-trivial phase shift permits perfect absorption in films thinner than one quarter wavelength.

be expected of a typical thin film interference anti-reflection coating. On the right (red) axis of Figure 3.5, we examine the reason behind this enhancement of the scaling factor near the material's plasma wavelength, where we have calculated the phase shift at the interface between our germanium films and highly doped silicon. At the boundary between a dielectric and a perfect electrical conductor, the expected phase shift of the electromagnetic wave is π radians, but our engineered metals of highly doped silicon exhibit non-trivial interfacial phase shifts. These phase shifts are small near the plasma wavelength but approach π radians at longer wavelengths far from the plasma wavelength. This reduced phase shift is how our samples are able to achieve perfect absorption despite the deep sub-wavelength thickness of the films.

After investigating the relationship between germanium thickness and absorption resonance, we investigated the polarization and angle dependence of the films. Figure 3.6 shows the experimental (a,c) and modeled (b,d) reflection spectra for the sample with a 412.5 nm thick germanium film for both s- (a,b) and p-polarizations (c,d). Both of the absorption resonances

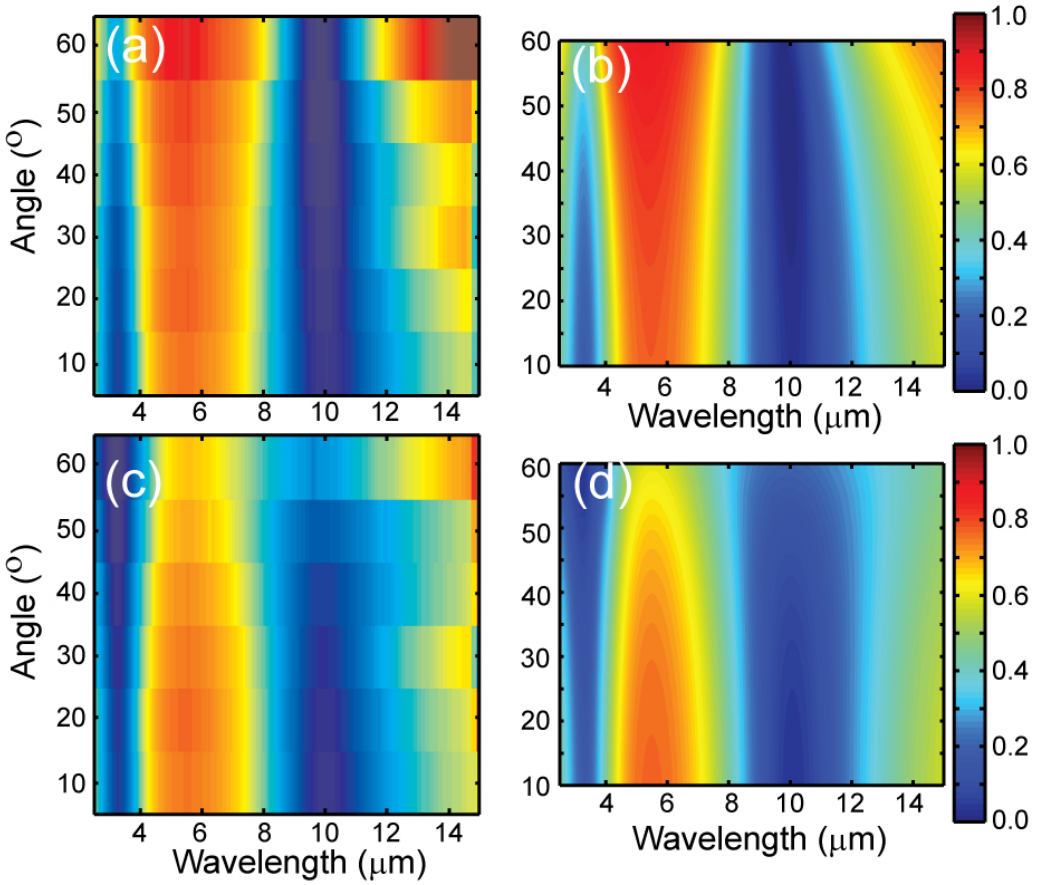

Figure 3.6: Angle-dependent and polarized reflection spectra for a sample with 412.5 nm of germanium. (a,c) Experimental, (b,d) modeled, (a,b) s-polarization, (c,d) p-polarization.

observed at normal incidence are still present at higher angles of incidence. Furthermore, the resonance does not shift significantly across the entire range of incident angles from 10° to 60°, nor is the resonance dependent on the polarization of the incident light. We attribute this insensitivity to angle of incidence to the large refractive index of germanium (n = 4), which means that the angle of refraction is always small in comparison. The small angle of refraction means that the optical path length through the germanium film is only marginally increased even at higher angle of incidence. The polarization insensitivity is explained similarly as Fresnel's equations predict that the reflection coefficients of s- and p-polarizations of light diverge slowly at small angles of incidence. Since the absorption of light in our samples occurs at the interface between the germanium and engineered metal and the angle of refraction at the germanium/air interface is small, then one would expect

little difference between the reflection spectra for the two polarizations, as is indeed predicted numerically and observed experimentally.

3.4 Selective Thermal Emission

Following our reflection study of our perfect absorbers, we next investigated their thermal emission spectra. As discussed previously, Kirchhoff's law of thermal radiation predicts that an object's absorptivity must equal its emissivity. We then expect that whenever a material displays a strong absorption resonance, it should also show a strong thermal emission peak at the same location. Experimental (a) and calculated (b) thermal emission spectra are shown in Figure 3.7 for each of the seven thicknesses of germanium investigated. Samples were mounted on a custom heating apparatus and heated to 450 K as described in detail in Section 2.3.1. The emission spectra, corrected for the thermal background emission of the spectrometer, show a clear shift to longer wavelengths as the germanium thickness of the samples is increased, as expected from the reflection results. The presence of atmospheric absorption is evident in the range of 5 – 7 µm, as this coincides with a strong absorption band of water vapor. In order to account for other sources of experimental dispersion, most importantly the response of our MCT detector, we next modeled our results numerically and scaled the computed spectra by the spectral response of the detector. For comparison, we have calculated the spectral emission of a perfect blackbody source scaled by the responsivity of the detector. With the exception of the 82.5 nm and 165 nm samples, the unmodified experimental results match very well with the scaled numerical results. The reduction in the emission peak of the aforementioned samples is clearly due to the atmospheric absorption mentioned earlier.

Our final experiment investigated the spatial selectivity of patterned samples, where the parts of the germanium film were removed using standard metal liftoff techniques. One of these patterns is depicted in Figure 3.7 (inset), which was imaged using a commercially available thermal camera. A germanium thickness of 412.5 nm was chosen as its emission peak is near 10 µm, which is the center of range of the camera and near the peak thermal emission of room-temperature blackbodies. The height of the image is approximately 2 mm. The orange regions of the image are those with a higher apparent

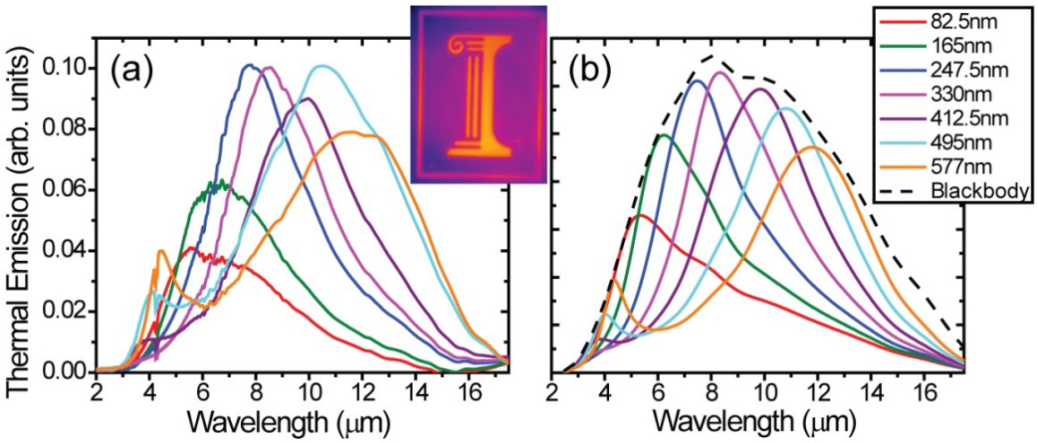

Figure 3.7: Experimental (a) and modeled (b) emission spectra for each of the germanium thicknesses investigated. Thermal image (inset) of a sample with the germanium film patterned with an "I" logo.

temperature, while those in purple have a lower apparent temperature. The orange areas are also those which have germanium, while the purple areas are without. The thermal image indicates that the germanium-coated regions selectively emit, while the uncoated regions emit a gray-body spectrum even though all regions are held at the same temperature.

3.5 Discussion

In conclusion, we have demonstrated strong-to-perfect absorption from sub-wavelength germanium films of varying thicknesses, deposited on heavily doped silicon engineered metal substrates. The ability to control the spectral position of the absorption resonance with germanium thickness across a wide range of MIR wavelengths was demonstrated. In addition, the spectral position and the strength of the observed resonances were shown to be largely angle- and polarization-insensitive. Thermal emission from these films was measured and shown to be spectrally selective, and patterned films were demonstrated to give spatially selective thermal emission. Our structures were modeled using a transmission matrix approach, and the model results agreed nicely with the experimental data, for both reflection and emission. Our experimental and modeling results indicate that the strong absorption observed results from the unique properties of our engineered semiconductor metals, which allow for control over the metal substrate's optical properties

across a broad range of wavelengths and strong absorption with effectively lossless dielectric coatings. The films demonstrated here are low cost, with a straightforward fabrication process, and thus hold potential for use as low-cost thermal light sources or emissivity controlling coatings.

The materials used in this experiment cannot be scaled easily to longer wavelengths. The performance of this material relied upon its ultra-high doping density. While lower doping densities could extend the plasma frequency to longer wavelengths, such a density would be too low to reliably control. Furthermore, the low doping density would also reduce the losses in the doped layer, which contributed to the rapid accumulation of phase at the designer metal's interface with the ultra-thin film germanium layer — allowing for that layer to be significantly thinner than the typical quarter wavelength thickness of anti-reflection coatings. Nevertheless, the addition of free carriers has potential utility in other approaches to developing FIR technologies to be discussed in later chapters. The work presented demonstrates the potential for perfect absorbers to be used as selective thermal emission sources. Chapter 4 will consider an alternate design of a perfect absorber, which is suitable for operation at FIR wavelengths.

Chapter 4

Metamaterial Selective Thermal Emitters

Thermal emitters are ubiquitous in MIR optics, serving as cost-effective broadband IR sources in most Fourier transform infrared (FTIR) spectrometers, as well as in a range of IR sensor and illumination systems. Such emitters work reasonably well at MIR, or even NIR, wavelengths, which correspond to peak thermal emission for a blackbody across a range of hot, but achievable, temperatures. At longer wavelengths, however, thermal sources become more problematic, simply due to their weak FIR spectral emittance, even at high temperatures as shown in Figure 4.1. At temperatures where emitted power from a 1×1 cm^2 blackbody surface, across the entire 30 – 40 µm wavelength range, approaches the 10 mW range, the fraction of total emitted power in this wavelength ranges is well below 1%, meaning that the vast majority of the system's energy is lost at wavelengths outside of this band. Thus, while cost-effective, thermal emitters are highly inefficient, especially for applications requiring light emission in only limited wavelength bands, or at long wavelengths.

However, the spectral range of emission for a thermal source can by controlled using surfaces and structures with engineered absorption resonances. By Kirchoff's law, which relates the emissivity and absorptivity of a surface $\epsilon(\lambda) = \alpha(\lambda)$, these resonances will, upon heating of the surface, result in spectrally selective thermal emission. Numerous approaches have been used to engineer the IR absorptivity, and therefore the emissivity, of such thin films, leveraging a variety of layered, patterned, and/or engineered surfaces and materials [66, 67, 76–84]. Much of the effort toward the development of selective thermal emitters has focused on the MIR (reasonably efficient for temperatures up to $\sim$ 1000 K) and, more recently, the NIR ($T >$ 1000 K)

This chapter contains experimental results and media that have been previously published in a scholarly journal: see [75]. AIP Publishing permits authors to include their published articles in a thesis or dissertation.

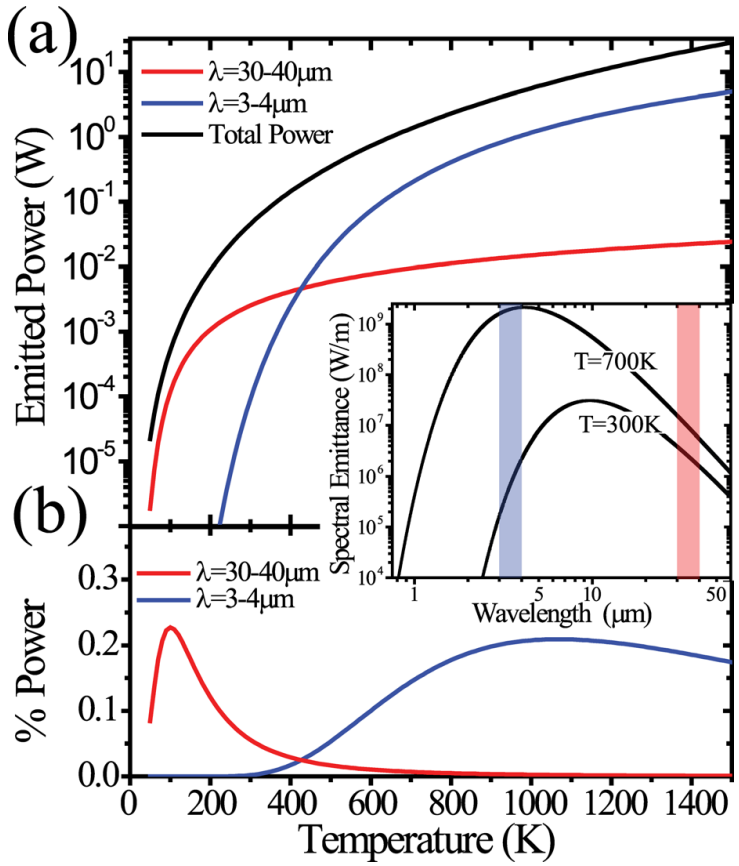

Figure 4.1: (a) Calculated integrated spectral emittance (power) from an ideal blackbody 1×1 cm^2 in the 30 – 40 µm (red) and 3 – 4 µm (blue) spectral bands, as well as across the entire spectrum (black). (b) Percent of total power emitted from a blackbody in the 30 – 40 µm (red) and 3 – 4 µm (blue) spectral bands. Inset shows log-log plot of blackbody spectral emittance for 300 K and 700 K surfaces, with the 30 – 40 µm (red) and 3 – 4 µm (blue) highlighted.

for thermophotovoltaic applications [68]. In such frequency selective surfaces, absorption can be engineered via thin-film interference, [22, 73] antenna or plasmonic resonators [66–68, 81] structured dielectric waveguides [85], propagating surface modes [76, 79] or even surface phonon polariton modes. The majority of the work utilizing phonon resonances has leveraged the high energy (10.6 – 12 µm) phonons of SiC [33, 86–91]. However, these surfaces have operating wavelengths limited to discrete bands determined by the material's phonon energies, and suffer from significant emission outside the spectral band of interest. Thus, the ability to design and engineer selective thermal emitters at long wavelengths, away from phonon resonances, may provide

cost-effective thermal light sources with improved efficiency and greater wavelength flexibility, even if the total power emitted in a given wavelength band is still limited by Planck's radiation law.

Selective thermal emitters have promise as tunable FIR sources with reasonably high output power. Previous work from our group successfully demonstrated a MIR selective thermal absorber and thus also a selective thermal emitter, by way of Kirchoff's law of thermal emission using a metamaterial composed of a patterned metal layer on top of a low loss dielectric spacer and a metal ground plane. In this case, both metals were gold, while the dielectric was spin-on-glass (SOG). The top gold layer was patterned with a 1D or 2D grating [67, 71], which coupled TM-polarized light into a resonance ($\lambda = 6 - 8$ µm) dependent upon the width of the strip ($w = 1.9 - 3.2$ µm). The efficiency of the coupling depended primarily on the thickness of the spacer ($t = 250$ nm). With carefully chosen parameters, the absorption resonance could be tailored to a specific wavelength and could approach near perfect absorption ($\sim 100\%$). Upon heating the device, strong selective thermal emission was observed. The work presented in this chapter extrapolated the previous metamaterial selective thermal emitter to longer wavelengths by selection of appropriately scaled dimensions and materials [75]. Once again, the top layer was patterned gold, while the dielectric spacer was changed to aluminum nitride (AlN) and the ground plane to molybdenum. The molybdenum was chosen as it facilitated the growth of the AlN on a silicon substrate. The AlN has a Reststrahlen band near $\lambda = 15$ µm, but beyond this band in the region with $\lambda = 30 - 40$ µm the materials exhibit low losses and low dispersion. Additionally, AlN is widely used to fabricate microelectromechanical systems (MEMS) devices due to its piezoelectric properties with the possibility of our selectively absorbing devices serving as the platform for novel FIR bolometric devices. A recent collaboration successfully demonstrated a similar device operating in the MIR [92].

4.1 Sample Design and Fabrication

The fabricated metamaterial selective emitters are depicted as schematics and micrographs in Figure 4.2 for the polarization-dependent 1D gratings (a) and the polarization-independent 2D gratings (b). The design consists of

a patterned metal (Ti/Au) top layer, separated from a solid metal ground plane (Mo) by a dielectric spacer (AlN). Here, we utilize AlN due to its high energy Reststrahlen band (11 – 15 µm) [93], which gives the AlN nearly constant refractive index at wavelengths much longer than its optical phonon resonances. Samples with varying thickness of AlN (1200, 1400, 1600, and 1800 nm) deposited above a layer of molybdenum (100 nm) were purchased from OEM Group, Inc. A layer of Au (65 nm) was then deposited via e-beam evaporation (with a 5 nm Ti layer for adhesion) over the AlN. The Ti/Au top surface was patterned using a KI/I_2-based gold etchant (Transene Gold Etchant TFA) through a lithographically defined photoresist etch mask. Grating patterns with periods $\Lambda = 20$ µm were chosen in an attempt to ensure that effects from diffraction would occur away from the wavelength range of interest. One-dimensional (1D) grating patterned samples with a range of grating widths were fabricated on wafers of each AlN thickness. In addition, two-dimensional (2D) grating patterns were fabricated for emission experiments. The 2D grating pattern was chosen so that the selective thermal emission would be polarization independent. Otherwise, the experiment would require the use of a polarizer, which would result in the loss of at least half of the emitted power.

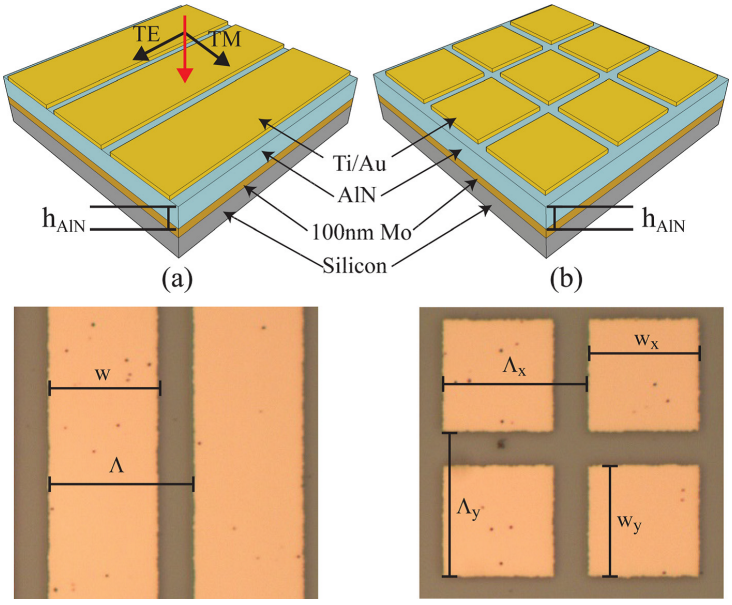

Figure 4.2: Layer structure, schematics, and micrographs of fabricated (a) polarization-dependent and (b) polarization-independent FIR absorber/emitter structures.

4.2 Permittivity Models of Materials

The wavelength-dependent permittivity of the AlN was modeled using a Lorenz oscillator with parameters taken from the literature [93] and shown in Equation 4.1. The model was defined in terms of the freespace wavenumber, $\bar{\nu}$, with units of cm^{-1}, where ϵ_0 is the low frequency permittivity of AlN, ω_L and ω_T are the longitudinal and transverse optical phonon frequencies, and γ is the phonon scattering rate. The permittivities of gold and molybdenum were calculated using the Drude model (see Section 1.4.1) with values taken from the literature [94, 95].

$$\epsilon_{AlN}(\bar{\nu}) = \epsilon_0 \left(1 + \frac{\omega_L^2 - \omega_T^2}{\omega_T^2 - \bar{\nu}^2 - i\gamma\bar{\nu}} \right) \tag{4.1}$$

Reflection measurements were taken before the deposition and patterning of the gold gratings. The experimental reflection measurements of the AlN on Mo gold plane were compared to RCWA calculations of the expected reflection for this structure. A least squares algorithm was used to fit the model parameters from the literature to the measured data with only modest adjustments to the cited values. The cited and model parameters are summarized in Table 4.1 for AlN and in Table 4.2 for gold and molybdenum. The real and imaginary parts of the AlN permittivity are shown in Figure 4.3.

Table 4.1: Aluminum Nitride Permittivity Model

	ϵ_0 $(-)$	ω_L (cm^{-1})	ω_T (cm^{-1})	γ (cm^{-1})
Cited	4.68	894.3	663.6	6.636
Fitted	4.96	894.3	663.6	6.636

Table 4.2: Drude Parameters for Gold and Molybdenum

	ϵ_0 $(-)$	ω_p (cm^{-1})	γ (cm^{-1})
Au	9.5	72765	571
Mo	0	60200	412

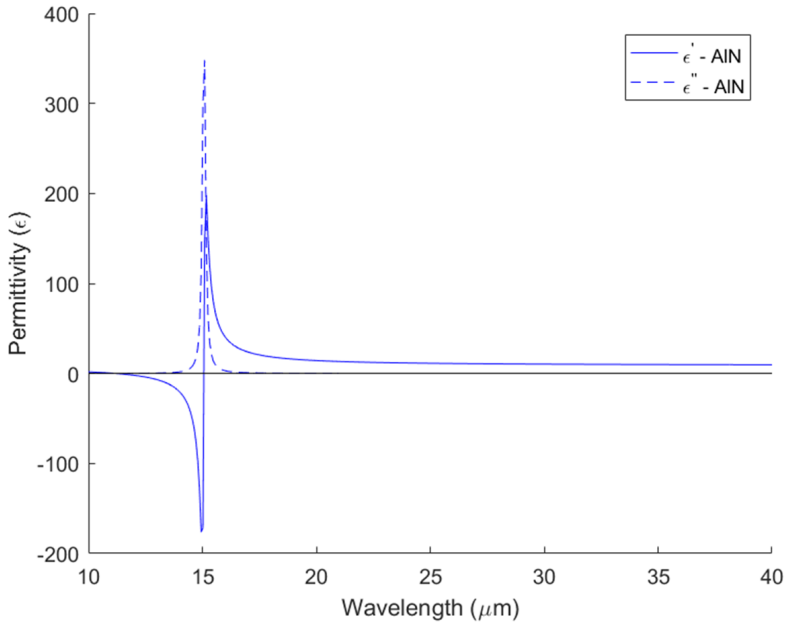

Figure 4.3: AlN permittivity. Real part (solid) and imaginary part (dashed). Note that the strong TO phonon resonance is apparent near $\lambda = 15$ µm in the material's Reststrahlen band high absorption and high dispersion. In the wavelength range of interest ($\lambda = 30 - 40$ µm), the real permittivity is approximately constant with low absorption.

4.3 Reflectivity

Reflection spectra were collected in a Bruker V80v Fourier transform infrared (FTIR) vacuum spectrum using a Pike Technologies 10Spec specular reflectance accessory, allowing for reflection spectra at 10° from the sample normal as described in Section 2.2.1. A KRS-5 wire-grid polarizer was placed in the beam path in order to obtain both transverse electric (TE) and transverse magnetic (TM) polarized reflection spectra. Figure 4.4 shows the RCWA-modeled and experimental TE- and TM-polarized reflection data for a 1D grating structure with $w = 13$ µm, $h_{AlN} = 1400$ nm, and $\Lambda = 20$ µm. As expected, strong absorption features are observed for TM, but not TE polarized light. Because the Mo groundplane is optically thick, and the periodicity of the grating structures is subwavelength, the strong TM reflection dip at $\lambda = 32.5$ µm cannot correspond to either transmission or diffraction, and must therefore be evidence of strong, spectrally selective absorption in the three-layer system. The inset shows the magnetic field amplitude ($\overrightarrow{H_y}$)

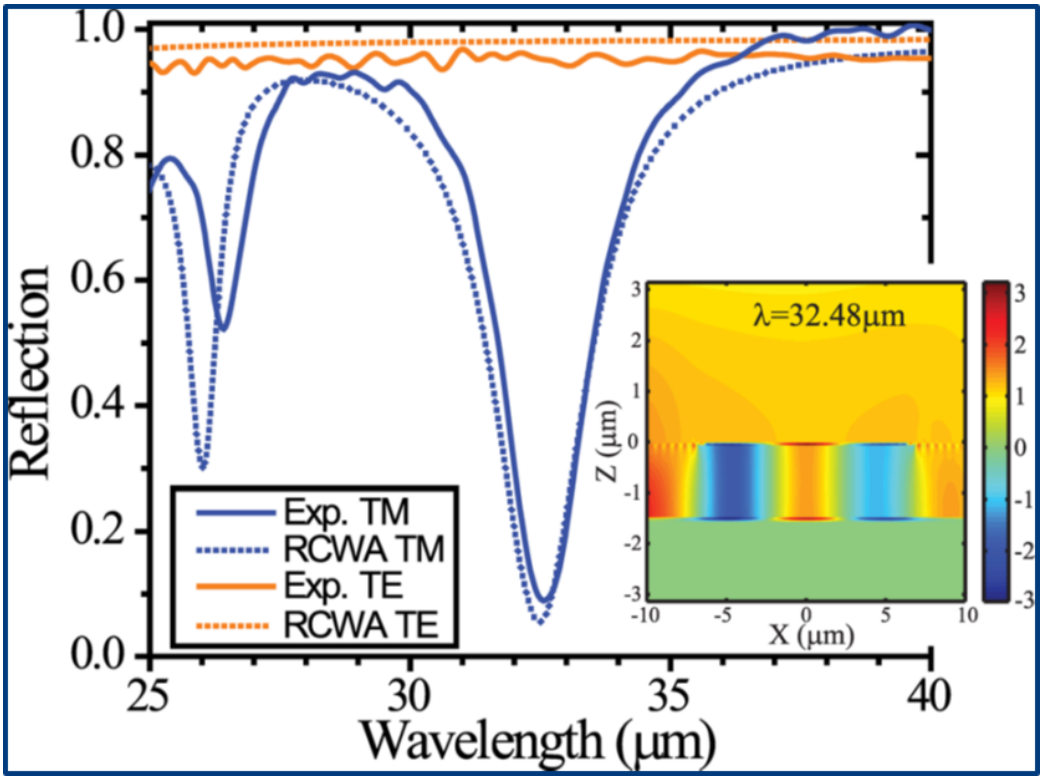

Figure 4.4: Simulated (dotted) and experimental (solid) reflection spectra for TE- (orange) and TM-(blue) polarized light incident at 10° from surface normal. Inset shows H_y at resonance ($\lambda = 32.5$ μm).

for TM-polarized reflection at resonance, indicating that we are coupling to a higher-order antenna mode in the top patterned Au layer. Strong absorption at similar wavelengths can be simulated with grating structures having $w = 4$ μm, $h_{AlN} = 600$ nm, and $\Lambda = 6$ μm, but these lower order resonances have spectral widths approximately twice those of the structures with the wider stripes presented here, and thus we chose to focus on the larger stripes, for their improved spectral selectivity.

Figure 4.5 shows the (a) simulated and (b) experimental TM polarized reflection spectra from a series of samples with 1D grating structures with $h_{AlN} = 1400$ nm and $\Lambda = 20$ μm, and with fabricated stripe widths of $w = 9.7$, 11.7, 13, 14, and 15 μm (undercutting during the metal wet-etch decreases the stripe widths from the designed by 2 μm). The experimental data show a good fit to our RCWA simulations. All samples show peak absorption of $\sim 90\%$, with off-resonant reflection $> 90\%$, with resonances across the $\lambda = 27 - 37$ μm wavelength range.

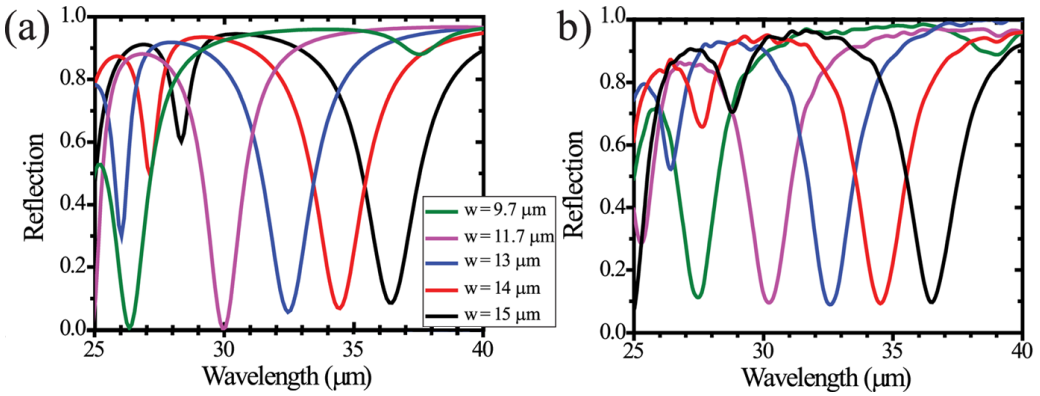

Figure 4.5: Simulated (a) and experimental (b) TM-polarized reflection from FIR absorber structures for structures with AlN thickness $h_{AlN} = 1400$ nm, $\Lambda = 20$ µm, and stripe widths $w = 9.7$, 11.7, 13, 14, and 15 µm. Because of undercutting during the metal wet-etch process, the designed stripe widths were $w = 13$, 14, 15, 16, and 17 µm.

4.4 Thermal Emission

For emission experiments, the sample was mounted on a hot-plate external to the FTIR, and the thermal emission from the sample, spatially filtered by an aperture, was collected and focused into the FTIR (with the input window removed) using reflective optics as described in Section 2.3.2. Both the sample and collection optics were enclosed with a plastic "tent" structure, and the FTIR and tent kept at nitrogen gas overpressure, in order to mitigate atmospheric absorption and the significant transmission losses of the FTIR window at longer wavelengths ($\lambda > 35$ µm). In order to isolate the sample emission from the significant thermal background, emission from the system was measured with the aperture blocked.

We also collected emission from a "black soot" reference sample with near-uniform broadband emissivity (in effect acting as a calibrated "graybody"). This sample was fabricated by placing our Si/Mo substrate (with AlN etched off) in the flame of a candle until the surface is optically black [96, 97]. Reflection measurements of the soot sample were taken using the Pike 10Spec reflection apparatus. Since the sample has an optically thick ground plane, no transmission is possible from the substrate, and the absorptivity of the sample was estimated to be, $A = 1 - R$, which by Kirchhoff's law of thermal emission is also equal to the emissivity. This measured graybody emissivity was used to correctly scale the measured emission of the black soot reference.

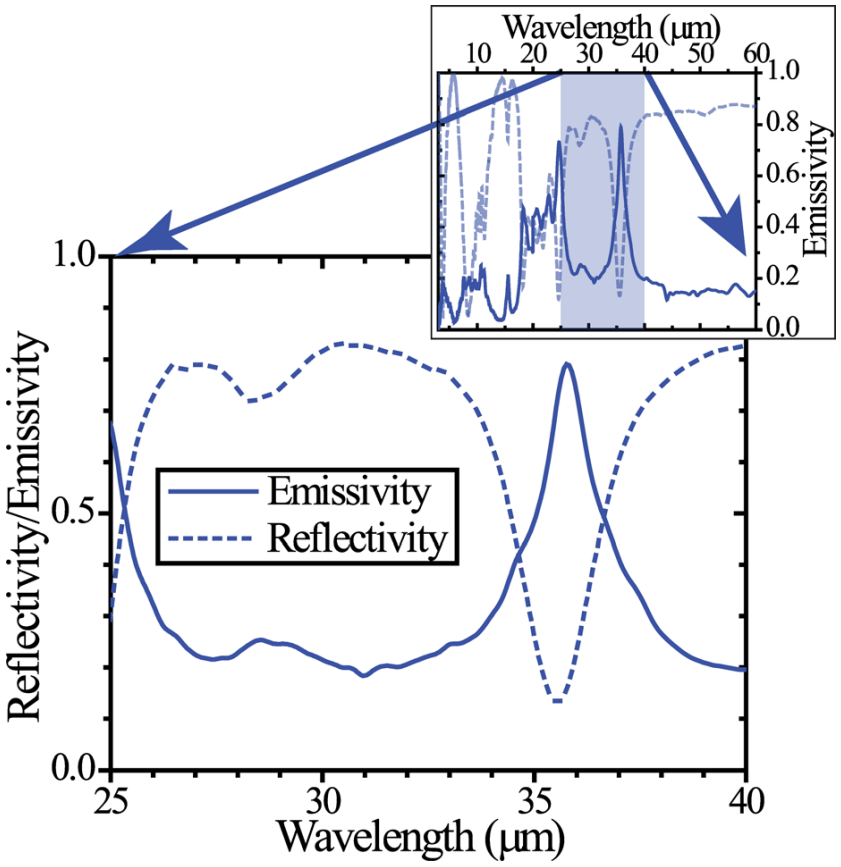

Figure 4.6: Experimentally measured IR (inset) and FIR unpolarized emissivity (solid) and reflectivity (dashed) of a sample with $h_{AlN} = 1400$ nm and a top patterned layer consisting of a 2D array of patches, with $\Lambda_x = \Lambda_y = 20$ µm and $w_x = w_y = 15$ µm.

For selective emitter applications, achieving strong off-resonant reflection is as important as the strength of the resonant absorption feature, as thermal emission away from resonance is integrated over a broad range of wavelengths, and even weak broadband, off-resonance emission can overwhelm the designed selective emission, especially for emitters designed to operate at long wavelengths. Figure 4.6 shows the experimental emissivity at 200 °C (along with room temperature reflectivity for comparison) from a sample with $h_{AlN} = 1400$ nm and a top patterned layer consisting of a 2D array of patches, with $\Lambda_x = \Lambda_y = 20$ µm and $w_x = w_y = 15$ µm. A 2D grating pattern was used to ensure polarization independent emissivity, allowing us to capture thermal emission without a polarizer, thus improving our signal to noise. As can be seen from Figure 4.6, a clear peak in the emissivity is observed at the designed resonance of the sample, and the spectral features observed in the

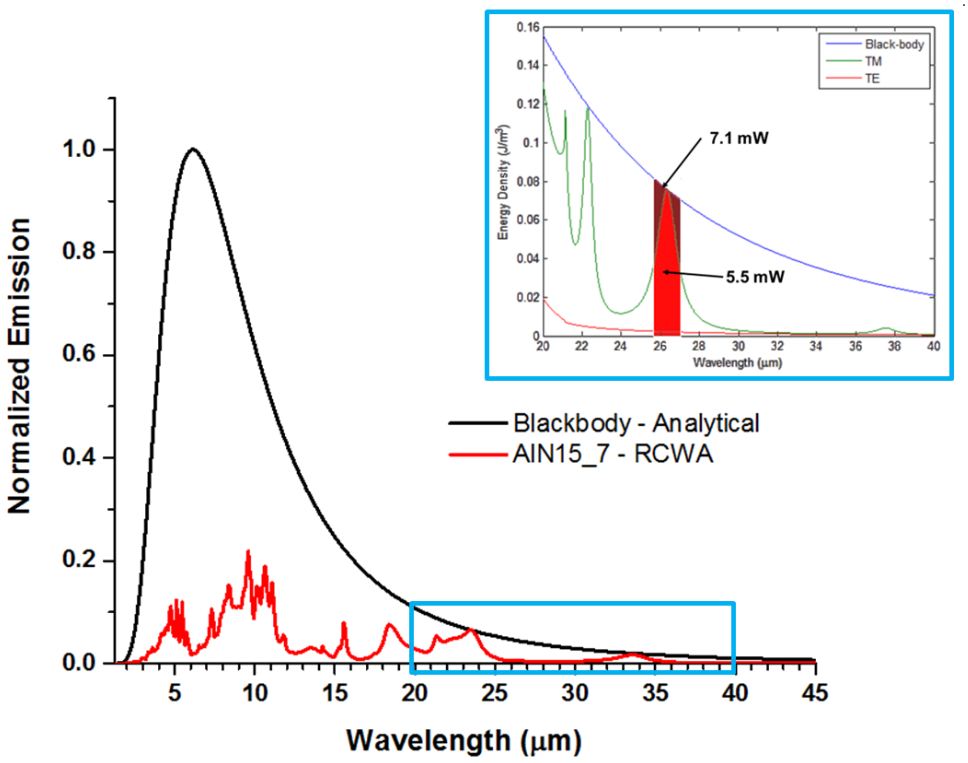

Figure 4.7: RCWA-simulated emission spectrum for the structure depicted in Figure 4.1b with a lateral area of 1×1 cm^2 maintained at a temperature of 600 K in an ambient environment of 300 K. (Inset) We estimate the thermal radiant power emitted in the narrow band depicted in red to be 5.5 mW. For comparison, the power emitted by a blackbody in the same band would be 7.1 mW.

room temperature, 10° incident angle reflectivity are generally reproduced in the experimental emissivity (despite the slight difference in angle).

In addition, we used our RCWA simulations to calculate the fraction of the samples' total thermal emission contained within the spectral range defined by the FWHM of our FIR emission resonance as shown in the inset of Figure 4.7. The estimated power that would be emitted from a 1×1 cm^2 sample maintained at a temperature of 600 K in an ambient environment of 300 K is depicted in the light red band of the inset, and is equal to 5.5 mW. For comparison, the additional power emitted from a blackbody emitter of the same area and temperature is depicted by the dark red band of the inset. The total power emitted by the blackbody in this band is 7.1 mW. For the sample in Figure 4.7, we note that 2.4% of the total thermal emission sits

within this wavelength band. For comparison, a perfect blackbody at the same temperature emits only 0.42% of its power in this same band. Thus, in addition to providing spectrally selective emission in the FIR, these structures also improve the efficiency of emission into the resonant wavelength band by over a factor of 5.

4.5 Discussion

In summary, we have demonstrated strong selective absorption and emission at FIR wavelengths from subwavelength thickness structures with designed absorption/emission resonances. We have shown both polarized and unpolarized resonances, and demonstrated control of the resonances across the $\lambda = 27 - 37$ µm wavelength range. Samples were characterized by FTIR reflection and emission spectroscopy, and modeled using 3D RCWA, with excellent agreement between the simulated and experimental response of the structures.

While the FIR, in particular, the portion of the FIR overlapping with the Reststrahlen band of traditional optoelectronic semiconductor materials, remains an extremely challenging wavelength range for the development of optical and optoelectronic structures and devices, the work presented here offers a small step toward the development of an optical infrastructure for this largely unexplored region of the electromagnetic spectrum.

Chapter 5

Surface Phonon Polariton Selective Thermal Emitters

Chapters 3 and 4 explored means of modifying the infrared absorptivity, and thus emissivity, of materials via an interference filter, in one case, and a metamaterial in the second case. Other approaches to engineering the thermal emission of materials include a broad range of designs, absorbing incident light (or thermally emitting light) via coupling to photonic crystals, [83, 99, 100], localized [66] and propagating surface plasmons [79, 80, 99], metamaterial structures [81, 101], antennas [67], or even unusual waveguide modes [84].

Many of the above absorption mechanisms rely on the coupling of light, in some form, to free carriers in metallic surfaces or metallic constituents of composite materials. Here, the optical response of the free carriers in the metal gives a negative real part of the metal permittivity ($\epsilon'_m < 0$), and can be modeled across a wide frequency range using the Drude formalism (see Section 1.4.1). Materials with negative permittivity resulting from free carriers can support propagating bound modes, typically, referred to as surface plasmon polaritons (SPPs). Similarly, a polar dielectric with a phonon resonance can support propagating bound modes, typically, referred to as surface phonon polaritons (SPhPs), as these materials also exhibit negative permitttivity in their respective Reststrahlen bands (see Section 1.4.2). In either case the regions of negative real permittivity support surface polariton modes (see Section 1.4.3).

Much of the proposed and demonstrated phenomena utilizing phonon resonances for negative permittivity have focused on SiC [85, 87–91, 102, 103], a strongly polar material with high-energy phonon resonances in the 10.6 – 12 µm wavelength range [104]. Examples of SiC-based optical phenomena include enhanced near-field light-matter interaction [87], superlensing [103],

This chapter contains experimental results and media that have been previously published in a scholarly journal: see [98]. AIP Publishing permits authors to include their published articles in a thesis or dissertation.

MIR perfect absorption [89], and extraordinary optical transmission and absorption in perforated SiC membranes [90]. In addition, patterned SiC has been used to demonstrate spectrally selective coherent emission resulting from thermally excited SPhPs outcoupling to free space via patterned gratings at an angle that depends on the wavevector of the SPhP [102]; the resulting emission is directional and quasi-monochromatic within a small angular window. Additional work exploring surface phonon polaritons has been carried out using GaAs [105–108] and in early work using GaP [109, 110], which each also exhibit strong phonon resonances in their respective Reststrahlen bands. The majority of surface phonon based phenomena have been investigated on SiC surfaces in large part because the high-energy phonons of SiC lie in the MIR and are thus accessible using standard MIR sources, detectors, and optics. However, it is conceivable that by utilizing materials with lower-energy phonon resonances, one can leverage the phonon resonances in the Reststrahlen band to develop a toolkit for novel optical and potentially optoelectronic materials and devices in the generally inaccessible FIR range.

Our intertest in SPhP modes lies in their interaction with phonons near the surface of the polar material. The key limitation of all of the previous methods of controlling a material's thermal emission is the reliance on thermal emission itself. Thermal emission of an object at a given temperature above the temperature of its ambient environment is an equilibrium process and will never emit more total power or more power within a particular wavelength band than that emitted by a blackbody under the same conditions. In short, when in thermal equilibrium, the emissivity of any material, at any wavelength cannot exceed unity. Overcoming this limitation would require the emission to be driven by a non-equilibrium process. One of the aims in our course of research was to investigate means by which phonon populations might be outcoupled to free space through interaction with surface modes. For this reason, we turn our investigations to surface polariton modes as a potential means to enable novel emission mechanisms in the FIR.

In this chapter, we used undoped gallium phosphide (GaP) substrates and patterned them with 1D gratings. SPhPs are supported at the interface of the GaP and air superstrate within the Reststrahlen band of GaP. The grating on the surface of the GaP permits the SPhP modes to couple to incoming and outgoing free space photons by adding additional momentum to the photons — thus crossing the SPhP dispersion curve. We demonstrate selective absorption

and subsequent selective thermal emision within the GaP Reststrahlen band. Chapters 6 and 7 will investigate the question of how one might enable the outcoupling of phonons through interaction with these surface modes.

5.1 Sample Design and Fabrication

The GaP gratings were fabricated using a wet etch process using a patterned SiOx etch mask. The samples were wet etched in a solution of hydrochloric acid, hydrogen peroxide, and deionized water [$HCl : H_2O_2 : H_2O(3 : 3 : 1)$], with 100 µL of 50 mM sodium dodecyl sulfate solution to improve the uniformity of the etch process. The lateral profile of the etched GaP was measured by surface profilometry and cross-sectional scanning electron microscopy (XSEM).

The GaP permittivity was modeled using the method (Equation 5.1) developed in [111] and is shown in Figure 5.1b. The model is parameterized by the high-energy permittivity (ϵ_∞), a primary oscillator corresponding to the GaP TO phonon resonance and denoted by the subscript "0" (i.e. S_0, γ_0, and ν_0), as well as two additional oscillators with much smaller amplitudes that characterize two-phonon interactions (subscripts "1" and "2"). Polarized reflection measurements were taken at a 10° angle on incidence using a Pike 10Spec apparatus (see Section 2.2.1) of the unpatterned GaP surface and compared to expected values calculated from Fresnel's equations (see Equation 2.2) and the above model with its cited parameters. A least squares algorithm was used to fit the first four parameters (those denoted by subscripts "∞" and "0") while fixing the cited values of the remaining parameters (see Table 5.1). Minor adjustments to the published fitting parameters (for the spectral position of the primary resonance) were made to align the rising edge of the modeled reflection (at $\sim$ 400 cm^{-1}) with our experimental measurements. The measured (solid blue) and fitted model (blue dots) TM-Polarized reflection spectra are depicted in Figure 5.1a and agree well, though the experimental reflection somewhat overestimates the predicted reflection in the highly dispersive region of the GaP permittivity, perhaps a result of either (i) imperfect reflection from the Au mirror used to normalize the spectra or, alternatively (ii) the difficulty in fitting the highly dispersive portion of the GaP permittivity.

$$\epsilon_{GaP} = \epsilon_\infty + \frac{S_0(1-(S_1+S_2))\nu_0^2}{\nu_0^2 - \nu^2 + i\nu\gamma_0 - \frac{S_1\nu_1^2\nu_0^2}{\nu_1^2-\nu^2+i\nu\gamma_1} - \frac{S_2\nu_2^2\nu_0^2}{\nu_2^2-\nu^2+i\nu\gamma_2}} \tag{5.1}$$

Table 5.1: Gallium Phosphide Permittivity Model

	Cited	Fitted
$\epsilon_\infty(-)$	9.09	9.426
$S_0(-)$	2.01	2.189
$\gamma_0(\mathrm{cm}^{-1})$	1.1	1.214
$\nu_0(cm^{-1})$	363.4	362.6
$S_1(-)$	7×10^{-4}	7×10^{-4}
$\gamma_1(\mathrm{cm}^{-1})$	21	21
$\nu_1(\mathrm{cm}^{-1})$	349.4	349.4
$S_2(-)$	3.5×10^{-4}	3.5×10^{-4}
$\gamma_2(\mathrm{cm}^{-1})$	12.6	12.6
$\nu_2(\mathrm{cm}^{-1})$	358.4	358.4

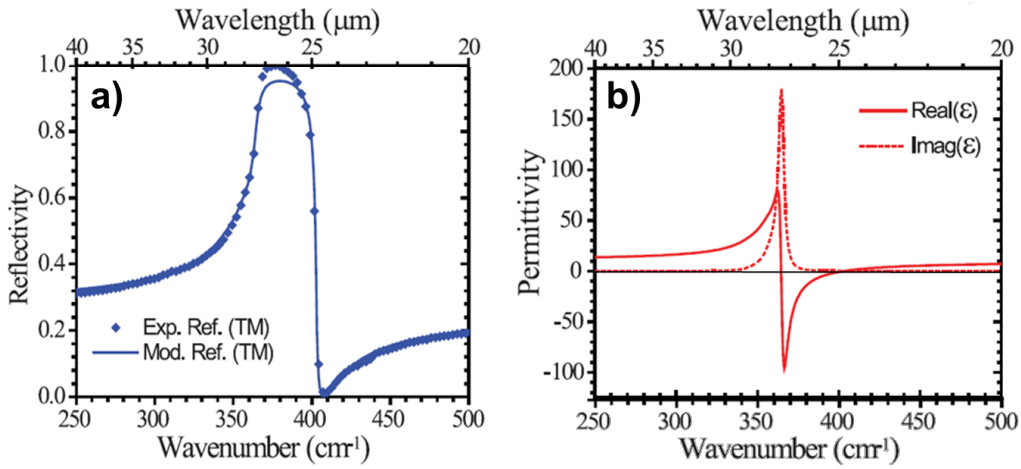

Figure 5.1: (a) Modeled (blue, calculated from the permittivity in (b)) and experimental (blue diamond) "TM" reflection from a flat GaP surface (b) Real (solid red) and imaginary (dashed red) permittivity of GaP, following model of Ref. [111].

5.2 Experimental Setup

Reflection spectra were measured with a Bruker V80v Fourier Transform Infrared (FTIR) vacuum spectrometer using an internal room temperature pyroelectric deuterated triglycine sulfate (DTGS) FIR detector. The experiment used a PIKE Technologies 10Spec specular reflection accessory (see Section 2.2.1), giving reflection spectra at a 10° angle of incidence within the vacuum sample compartment, thus minimizing effects of atmospheric absorption. Reflection spectra were measured in two orientations, shown schematically in Figures 5.2a and 5.2b and a KRS-5 FIR beamsplitter was used to select the polarization of the incident light. SPhPs can only be excited by incident light with a component of the electric field perpendicular to the grating ridges, thus only one polarization in each configuration can excite the SPhPs. In Figure 5.2a, only the TE-polarized incident light (where the incident electric field is always parallel to the sample surface) couples to SPhPs, while in Figure 5.2b it is the TM-polarized light (where the magnetic field is always parallel to the sample surface), which couples to SPhPs. We refer to the sample orientations shown in Figure 5.2a and Figure 5.2b as "TE" and "TM," respectively. All reflection data were normalized to reflection off of a gold mirror.

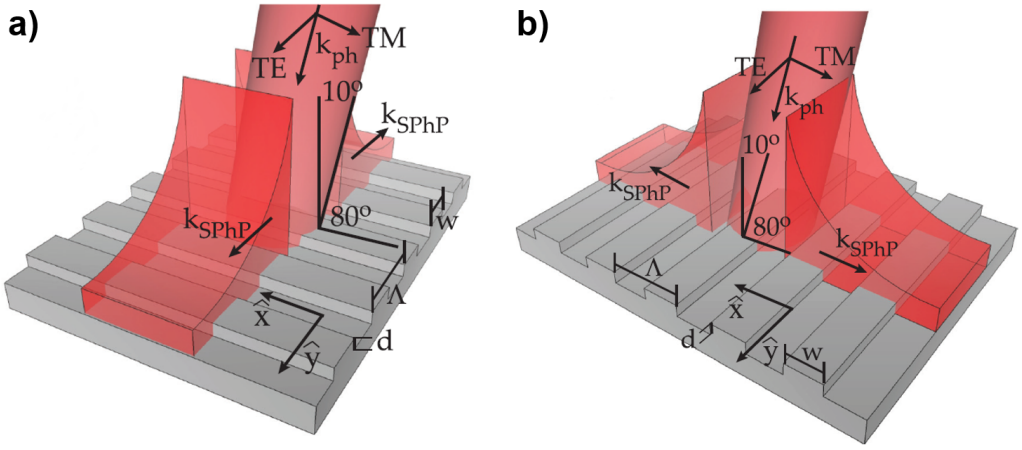

Figure 5.2: Schematics of SPhP excitation in the (a) TE and (b) TM experimental configurations, showing incident light with propagation constant kph and electric field polarizations, as well as the SPhP propagation on the patterned GaP surface.

5.3 Reflectivity

Reflection spectra from the GaP samples for both the TE and TM sample orientations are shown in Figure 5.3 for patterned samples with grating periods from 15 to 40 µm (colored lines), along with reflection data for the flat GaP wafer (black line). No reflection dips were observed for light polarized parallel to the grating lines, in either experimental configuration. The dips in the TM-polarized reflection for the patterned samples are attributed to coupling into SPhP modes. Figure 5.3 also shows simulated polarized reflection calculated using finite element methods (FEM) from patterned GaP surfaces for both sample orientations [5.3b-TE, 5.3d-TM], using the commercial FEM package COMSOL Multiphysics.

The surface profile of the patterned samples, determined by surface profilometry (an XSEM image of a sample with a grating period of $\Lambda = 40$ µm

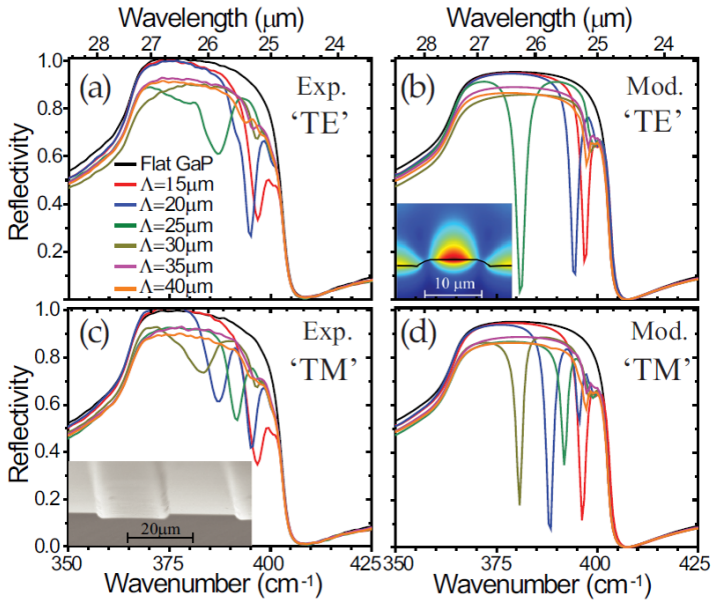

Figure 5.3: (a and c) Experimental and (b and d) modeled reflection spectra from patterned (color-coded lines) GaP grating structures in the (a and b) "TE" and (c and d) "TM" experimental reflection configurations. Reflection from patterned GaP samples with grating periodicities of 15 (red), 20 (blue), 25 (green), 30 (yellow), 35 (magenta), and 40 (orange) µm are shown. Calculated and experimental reflection from flat GaP surface (black) is shown for comparison. The inset in (b) shows the simulated magnetic field intensity for the $\Lambda = 20$ µm. The inset in (c) shows an XSEM image of the $\Lambda = 20$ µm sample.

is shown in the inset of Figure 5.3c), were imported into our FEM model, while the GaP permittivity used is that shown in Figure 5.1. FEM models were verified using rigorous coupled wave analysis (RCWA, not shown), which replicates both the experimental and FEM data. Sharp dips in reflection occur at wavelengths corresponding to coupling to SPhP modes. The inset of Figure 5.3b shows the magnetic field at resonance for a sample with $\Lambda = 20$ µm for the TE orientation, and bears all the hallmarks of a bound surface electromagnetic mode.

It can be seen that the depth of the reflection dips in our simulations are somewhat stronger than our experimental dips. We attribute this discrepancy to both fabrication imperfections (i.e., variation in etch depth, etched surface roughness) and experimental factors (imperfect incident beam collimation and/or Au background normalization). The modeled coupling frequencies, and relative coupling strengths, closely resemble those observed experimentally. Stronger dips in reflection are observed, both experimentally and in simulations, for gratings with $\Lambda < 25$ µm, where no diffraction of the incident light is possible. For absorption resonances farther from the GaP phonon resonance (in the less-dispersive portion of the GaP permittivity), we see agreement in the spectral position of our resonances to within ~ 1 cm^{-1} between model and experiment.

However, for resonances occurring in the more highly dispersive region of the GaP permittivity, we observe a larger discrepancy between model and experiment, both in spectral position (~ 5 cm^{-1}) and intensity. Such a discrepancy could be an indication again, of the difficulty in accurately modeling the GaP permittivity closer to the phonon resonance. In addition, this discrepancy could also result from the greater sensitivity of our response, in this frequency region, to even slight changes in beam collimation, incidence angle, or sample position.

5.4 Polariton Dispersion

Using Equation 5.2 and the permittivity from Figure 5.1a, we calculated the dispersion relation for SPhPs (see Section 1.4.3) on a flat GaP substrate. The disperson relation in Equation 5.2 relates the wavenumber (k_{SPhP}) of the SPhPs, the freespace wavenumber of the incident light ($k_0 = \frac{\omega}{c}$), the permittiv-

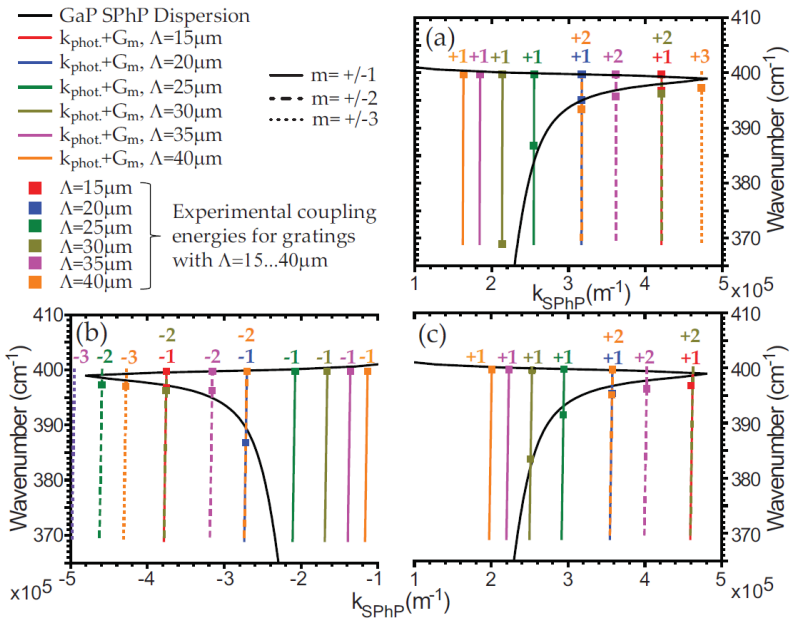

Figure 5.4: Dispersion curves for GaP surface phonon polaritons as calculated from the modeled GaP permittivity (solid black) and from our experimental data (colored squares). Experimental SPhP dispersion calculated from data (a) taken in the "TE" configuration, where the incident photons have no momentum in the grating direction and thus, the ± SPhP modes are degenerate, and (b and c) in the "TM" configuration, where the incident light has a momentum component in the grating direction, for (b) backward and (c) forward propagating SPhPs.

ity of the polar dielectric material (ϵ_{ph}, i.e. GaP), and the permittivity of the adjacent dielectric medium (ϵ_d, i.e. air). SPhP modes can only be sustained when the permittivity of the polar dielectric is negative, and its absolute value exceeds that of the adjacent dielectric medium per the constraints indicated in Equation 5.2. In order for SPhP modes to couple to the GaP surface, it is necessary to match the polariton momentum (k_{SPhP}) with that of the incoming photon (k_0) by use of a periodic grating (Λ) on the surface of the GaP. The grating adds additional momentum ($\frac{2\pi m}{\Lambda}$), either parallel($\hat{x}$) or perpendicular ($\hat{y}$) to the incident photon (refer to the coordinate system in Figure 5.2), in accordance with Equation 5.3. By tabulating the experimental reflection dips, and then using Equation 5.3, assigning an index (m) to each dip, we generate a series of points relating the SPhP coupling frequency to the SPhP wavevector. The results are plotted in Figure 5.4 (for each sample orientation), where the solid squares indicate color-coded data points from the

samples of varying period, and the color-coded lines represent the magnitude of the photon+grating momenta, $\left|k_0(\omega)\sin(\theta)\hat{x} + 2\pi m/\Lambda(\hat{x}\ or\ \hat{y})\right|$, for the given angle of incidence and grating period, in effect, graphically reproducing Equations 5.2 and 5.3. Our experimental data largely lie on the calculated GaP dispersion, suggesting the reflection dips observed experimentally are evidence for coupling to GaP SPhPs.

$$k_{(SPhP)} = \frac{\omega}{c}\sqrt{\frac{\epsilon_{ph}\epsilon_d}{\epsilon_{ph}+\epsilon_d}}, \quad \epsilon_{ph} < 0 \quad and \quad \left|\frac{\epsilon_{ph}}{\epsilon_d}\right| > 1 \tag{5.2}$$

$$\pm\,\vec{k}_{SPhP} = \frac{2\pi m}{\Lambda}(\hat{x}\ or\ \hat{y}) + k_0\sin(\theta)\hat{x} \tag{5.3}$$

5.5 Thermal Emission

Finally, we measured the polarized thermal emission from a flat GaP surface and multiple patterned GaP samples. Polarized thermal emission spectra were measured by mounting the samples on a hot-plate held at 473 K and coupling the emitted light, through the FIR polarizer, into the FTIR via a parabolic focusing mirror. The emitted thermal radiation was spatially filtered with a vertical slit aperture providing acceptance angles between $\pm 7.5°$ and collected with a gold parabolic mirror. Background thermal emission spectra were taken from a covered input port of the FTIR and subtracted from the thermal emission spectra. The spectra were then normalized to emission from an Omega BB703 calibrated blackbody source operating at the same temperature (473 K).

Figure 5.5 shows both the thermal emission and the reflection (polarized for the electric field perpendicular to the gratings) from four of the samples studied in this chapter. Selective thermal emission is observed from GaP samples with grating periodicities of $\Lambda = 20$ and 25 µm, with relative intensities similar to the relative intensities of these samples' reflection dips. The flat GaP and $\Lambda = 30$ µm samples show little to no thermal emission in this wavelength range, as would be expected from their reflection spectra, which show no (or weak) dips from SPhP coupling. A shift in wavelength is observed between

the thermal emission peak and reflection dip for each sample and is attributed to a shift in the GaP permittivity with temperature [112–114]. While small ($\sim$ 3.5 cm^{-1}) for the Λ = 20 µm sample, this shifts grows larger ($\sim$ 7.5 cm^{-1}) for the Λ = 25 µm sample, whose coupling resonance lies in the highly dispersive portion of the GaP permittivity, again indicating the sensitivity of the resonance (to experimental and material changes) in this range of the Reststrahlen band.

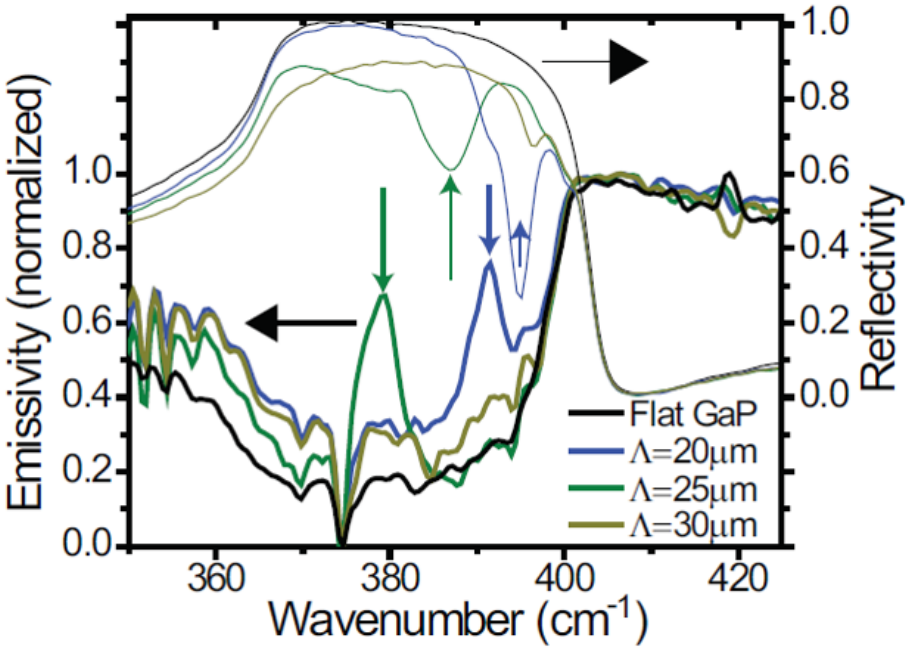

Figure 5.5: "TE" configuration reflection (thin lines) and polarized surface normal thermal emission (thick lines) from flat GaP surface (black) and patterned GaP surfaces with 20 µm (blue), 25 µm (green), and 30 µm (yellow) grating periods. Arrows indicate primary reflection and emission resonances for the 20 and 25 µm grating samples, showing the shift in resonance with temperature. Note: y-axis is offset to prevent overlap of plots.

5.6 Discussion

In conclusion, we have demonstrated excitation of SPhPs on patterned GaP surfaces in the FIR ($k_0 > 25$ µm) Reststrahlen band. Samples were characterized by FIR reflection spectroscopy and modeled using finite element

methods. The SPhP dispersion curve was extracted from the experimental reflection measurements and agrees well with the modeled and simulated SPhP dispersion. Selective emission via outcoupling of thermally excited SPhPs was also demonstrated for the patterned samples. While the thermal emission resonances were relatively weak and only limited sideband suppression, the thermal out-coupling of surface phonon modes suggests the possibility of phonon-based architectures for the manipulation and generation of light at FIR frequencies and further enabling the development of optical components at Reststrahlen band frequencies. Chapter 6 will consider a means of modifiying the permittivity within a material's Reststrahlen band using hybrid polariton modes to allow thermal emission near the LO phonon energy.

Chapter 6

Extending the Reststrahlen Band with Hybrid Modes

In an effort to leverage the exciting results from the recent work investigating surface modes in III-nitride and III-V semiconductors, we will investigate a path toward furthering development of FIR optical infrastructure, integration of phononic surface modes with optoelectronic structures [116], and a potential mechanism for linking lattice vibrations resonances to free space light. Recent work has shown LSPh's on GaN [117] ($\lambda \sim 15$ µm) and SPhPs on GaP [98] ($\lambda \sim 25$ µm) and GaAs [105,106] ($\lambda \sim 35$ µm). Unfortunately, the majority of materials supporting surface phonon modes have nowhere near the wavelength flexibility of their plasmonic counterparts. The negative permittivity range of these materials is typically quite narrow, extending only from near the LO phonon energy to the TO phonon (the semiconductor's Reststrahlen band), though near the TO phonon energy extremely large losses dominate the optical response of the materials. In this chapter we demonstrate that by combining the control of optical parameters offered by doping and the fixed optical response of phonon resonances, we are able to engineer materials which support hybrid phononic/plasmonic surface modes, effectively extending the range of negative permittivity associated with a semiconductor's Reststrahlen band. In particular, these results demonstrate coupling of hybrid surface modes at or near the LO phonon energy, which is one of two epsilon near zero (ENZ) points in the Reststrahlen band of undoped semiconductors, where these undoped materials cannot support surface modes. The lightly doped material shifts the corresponding ENZ point to higher energy [118] permitting surface modes near the LO phonon energy and suggesting the opportunity for further work that may enable free space out-coupling of vibrational lattice modes [119–122]. It should be noted that merely shifting the Reststrahlen

This chapter contains experimental results and media that have been previously published in a scholarly journal: see [115]. Dr. Yujun Zhong used molecular beam epitaxy (MBE) to grow the doped gallium arsenide samples under investigation.

band to a different wavelength range can be accomplished by choosing different semiconductors or their alloys. However, regardless of the intrinsic material chosen, surface polaritons cannot be sustained near the LO phonon energy without some additional modification of the material's permittivity — such as light doping.

Many other works have investigated hybrid bulk plasmon/phonon modes in semiconductors [123, 124] some specifically in GaAs [125–127]. Additionally, many recent works have observed hybrid surface plasmon/phonon modes at heterostructure interfaces [128–131] with plasmonic modes supported in one material and phononic modes supported in the other. However few works have considered hybrid surface modes supported in the same material. We grow moderately doped layers of GaAs above semi-insulating (SI) GaAs, and pattern this material into 1D grating structures capable of supporting both propagating and localized hybrid phonon/plasmon modes. We demonstrate coupling to these hybrid surface excitations and show that by controlling the doping of our epitaxially grown GaAs, we are able to support hybrid surface modes outside the traditional Reststrahlen band of GaAs.

6.1 Sample Design and Fabrication

In this chapter we investigate three samples. Sample A is a wafer of SI-GaAs, while Samples B and C have 2 µm of lightly ($n_B = 6 \times 10^{17}$ cm^{-3}) and highly ($n_B = 3.8 \times 10^{18}$ cm^{-3}) doped GaAs, respectively, grown on SI-GaAs substrates using molecular beam epitaxy (MBE). At the FIR wavelengths of interest (30 – 40 µm), Sample A will only support phonon polaritons, while the surface modes of the Sample C will largely be plasmonic. Sample B will support hybrid modes, as the negative permittivity due to free carrier and lattice effects will be of the same order.

Our materials and patterned samples are modeled using rigorous coupled wave analysis (RCWA) (see Section 2.5). We model the permittivity of our materials using a combination of the Drude model (see Section 1.4.1) and a dual Lorentz oscillator model for the phonon response [132] (see Section 1.4.2), such that:

$$\epsilon(\omega) = -\frac{\epsilon_\infty \omega_p^2}{\omega(\omega + i\gamma)} + \frac{(\epsilon_0 - \epsilon_\infty)\omega_{TO}^2}{\omega_{TO}^2 - \omega^2 + 2i\omega\Gamma_{ph}} + \frac{(\epsilon_\infty - \epsilon_{uv})\omega_{vis}^2}{\omega_{vis}^2 - \omega^2 + 2i\omega\Gamma_{vis}} + \epsilon_{uv} \tag{6.1a}$$

$$\omega_p^2 = \frac{e^2 n}{m^* \epsilon_0 \epsilon_\infty} \tag{6.1b}$$

$$\sqrt{\frac{\epsilon(\infty)}{\epsilon(0)}} = \frac{\omega_{TO}}{\omega_{LO}} \tag{6.1c}$$

Here, ϵ_{uv}, ϵ_∞, and ϵ_0 are, respectively, the high- and low-frequency and static contributions to the background permittivity of the semiconductor, ω_{TO}, and ω_{LO} the transverse and longitudinal optical phonon frequencies (related by the Lyddane-Sachs-Teller relation in Equation 6.1c) , γ and Γ_{ph} the plasmon and phonon scattering rates, and plasma frequency ω_p, which depends on the free carrier density n and effective mass m^*, and which we define as the frequency at which the free carrier contribution to the permittivity negates the high-frequency background permittivity as in Equation 6.1b. The second high-frequency oscillator, centered at ω_{vis} and dampened by Γ_{vis}, is an approximation of the NIR and visible contributions to the permittivity. The parameters used to model each sample's permittivity are listed in Table 6.1.

Table 6.1: Permittivity Parameters for Each Sample

Sample	ϵ_∞	ϵ_0	ω_{TO} (cm^{-1})	Γ_{ph} (cm^{-1})	n (cm^{-3})	m^*	ω_p (THz)	Γ (THz)	ω_{vis} (cm^{-1})	Γ_{vis} (cm^{-1})	ϵ_{vis}
A	10.86	12.96	268	1.3	-	-	-	-	2300	1	4.5
B	10.86	12.96	268	1.3	6.0×10^{17}	0.067	26.7	7.54	23000	1	4.5
C	10.86	12.96	268	2.8	3.8×10^{18}	0.067	67.6	16.8	23000	1	4.5

Figure 6.1 shows the experimental (squares) and modeled (lines) reflection at 10° incidence angle from the unpatterned samples studied in this chapter. The layered systems are modeled using RCWA with the material permittivity given by the expressions in Equations 6.1, with our modeled reflectivity matching the experimental data closely across the wavelength range of interest. The extracted permittivity for the lightly doped epi-layer sample (B), shown in Figure 6.1b), clearly demonstrates that we are able to extend our region of negative permittivity well past the LO phonon energy (marked with the vertical dashed line), giving the opportunity to engineer hybrid surface modes

outside the Reststrahlen band. The additional spectral range in which we are able to support surface waves is shaded in Figure 6.1a-b. Of course, the heavily doped sample can support surface waves across a much greater portion of the FIR, but these waves are predominantly plasmonic, and have little polarization resulting from the lattice. This is shown in Figure 6.1(c) and (d) where we plot the real and imaginary contribution to the material permittivity from lattice vibrations (ϵ'_{ph} and ϵ''_{ph}, respectively) and free carriers (ϵ'_{pl} and ϵ''_{pl}, respectively). As can be seen from these plots, at the edge of the GaAs Reststrahlen band ($\lambda \approx 34$ µm), the permittivity of the highly doped GaAs (Sample C) is dominated by the free carrier response, while for the lightly doped Sample B, lattice vibrations and free carriers contribute equally to the permittivity. In addition, we calculate figures of merit (FOM) for SP(h)P and LSP(h) modes supported on the materials in Samples A, B, and C, using the expressions:

$$FOM_{SPP} = \frac{L_{SPP}}{\delta_{SPP}} \quad and \quad FOM_{LSP} = \frac{\omega \frac{\mathrm{d}\epsilon'_m}{\mathrm{d}\omega}}{2\epsilon''_m} \tag{6.2}$$

where L_{SPP} and δ_{SPP} are the propagation length and penetration depth of the SP(h)P mode and ϵ'_m and ϵ''_m are the real and imaginary components of the "metal" permittivity [133, 134]. The results of these calculations are shown in Figure 6.1e, demonstrating that the doped GaAs offers a larger wavelength range supporting both localized and propagating modes. If we define this wavelength range by $W = \Delta\omega_{RB}/\omega_{TO}$, where $\Delta\omega_{RB}$ is the spectral width of the $\epsilon < 0$ region, we see that the narrow range of the undoped Sample A ($W_A \sim 0.0825$) is more than doubled by the light doping of Sample B ($W_A \sim 0.205$). While the FOM_{SPP} for all three materials are similar, the FOM_{LSP} is significantly degraded for the highly doped GaAs (Sample C), a result of the additional material losses coming from free carriers. The highly doped sample can hardly be considered to support hybrid plasmonic/phononic modes, as the dominant response is largely plasmonic. Such highly doped semiconductors have been the subject of much recent work [20–26], but because we are interested here in characterizing hybrid phononic/plasmonic modes, we will, for the remainder of the manuscript, focus on Samples A and B.

Our samples were patterned with 1D gratings in order to investigate both propagating and localized hybrid plasmon/phonon modes. The gratings add

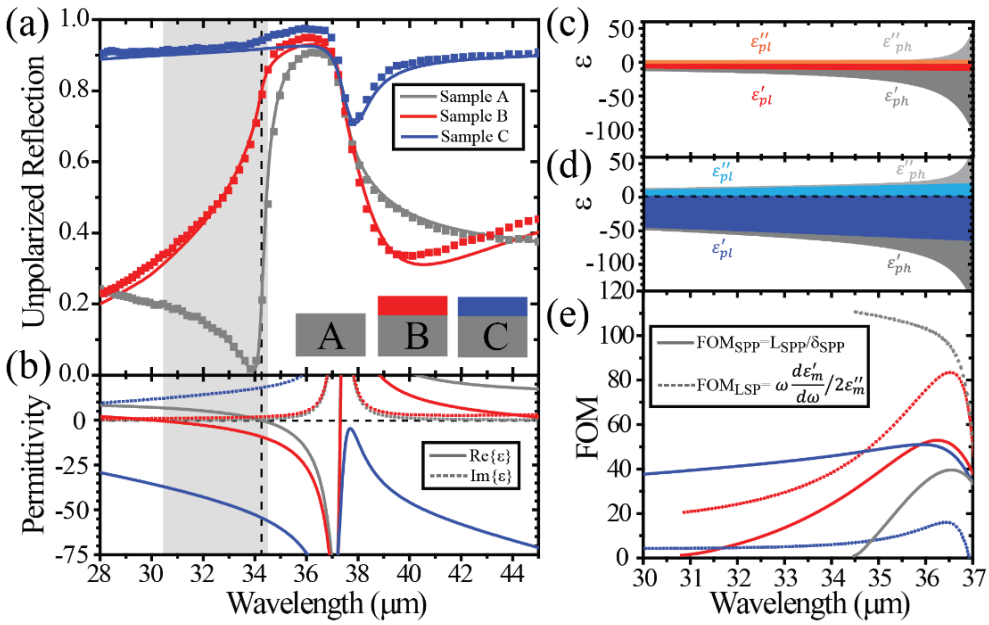

Figure 6.1: (a) Reflection spectra of unpatterned Samples A (gray, semi-insulating GaAs wafer), B (red, 2 μm Si:GaAs $n_B = 6 \times 10^{17}$ cm^{-3}), and C (blue, 2 μm Si:GaAs $n_C = 3.8 \times 10^{18}$ cm^{-3}). (b) Extracted Real (solid) and Imaginary (dashed) components of the permittivity of Samples A (gray), B (red) and C (blue). Inset in (a) shows the structure of unpatterned samples studied. Stacked area plots show the contributions to the real and imaginary permittivity in (c) Sample B and (d) Sample C from free carriers and lattice vibrations. (e) Calculated figures of merit for LSP(h)'s (dotted) and SP(h)P's (solid) as a function of wavelength for each of the three samples (A-gray, B-red, and C-blue).

to the photon momenta in the grating direction and allow coupling to the hybrid surface modes supported on the semiconductor surface; without the gratings, direct coupling of free-space photons to the surface modes is not possible due to a momentum mismatch. Coupling to propagating SPhP modes and hybrid surface plasmon/phonon polariton (SPPhP) modes are demonstrated on Samples A (intrinsic GaAs) and B (lightly doped). Samples were wet etched using a 4.76 mol/L solution of monohydrate citric acid mixed at a 5:1 ratio with hydrogen peroxide $[C_6H_8O_7 \cdot H_2O : H_2O_2\ (5:1)]$ to a depth of 1.4 μm with a 35 μm period grating and 18 μm wide grating ridges.

6.2 Experimental Setup

Our samples are characterized by FTIR polarization- and angle-dependent reflection spectroscopy in a Bruker v80v FTIR using a Mylar beamsplitter and FIR DTGS detector. Two reflection accessories were used to measure the sample reflection within the FTIR's vacuum sample chamber, mitigating atmospheric absorption signatures in our spectra. The first, a Pike Technologies 10Spec reflection accessory allows for fixed 10° incident angle reflection (see Section 2.2.1) and is used to measure reflection from the as-grown samples (from which we are able to extract the layer permittivity), as well as to measure reflection from 1D-patterned samples as a function of sample rotation about the surface normal. The second is a Pike Technologies VeeMAX III (see Section 2.2.3), which allows for variable angle reflectance from 30 – 80° incidence angles. In this experiment, shown in Figure 6.2, the sample is placed in the measurement chamber such that the grating lines are parallel to the plane of incidence of the incident radiation (incident with $\theta = 10°$), which is TE polarized (the electric field is parallel to the sample surface). The sample is then rotated around the sample normal by an angle ϕ, changing the component of the incident photons' momentum in the direction of the SPPhP propagation. Doing so allows us to map out a reasonable portion of the dispersion curve for the surface modes supported by our material.

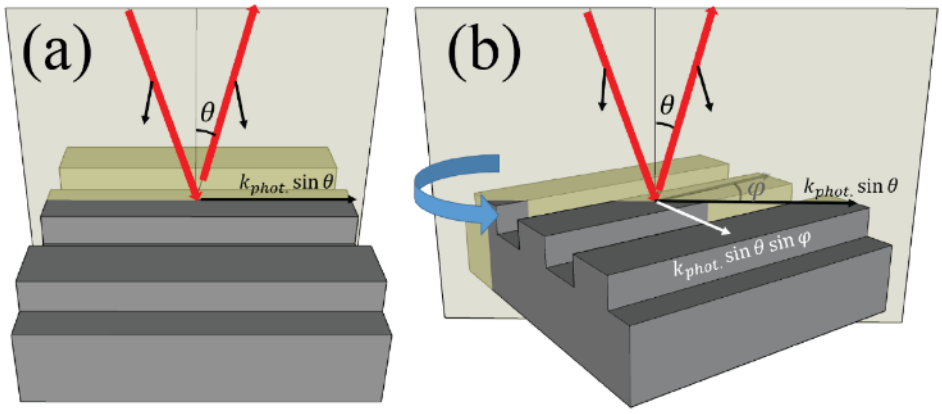

Figure 6.2: Schematic of experimental setup for determination of surface mode dispersion. In (a), the incident photon has no momentum in the grating direction, while in (b) the incident photon has a momentum component given by $k_{ph,x} = k_0 \sin\theta \sin\phi$, where $\theta = 10°$, fixed by our experimental apparatus, and ϕ varies from 0 to 50°.

6.3 Hybrid Polariton Dispersion

Figure 6.3 shows the calculated dispersion curves for both our undoped (gray) and doped (red) GaAs, calculated assuming GaAs and air occupying the half-spaces $z < 0$, $z > 0$, respectively. The red and black squares correspond to coupling energies/wavevectors as calculated using RCWA simulations of our actual structures. The divergence of the RCWA data from analytical calculations is a result of the finite thickness of the doped layer used in the RCWA, as can be seen by the red circles in Figure 6.3, which show coupling energies/wavevectors for infinitely thick lightly doped GaAs. Even with the finite thickness ($\sim \lambda_0/15$) of the doped GaAs, a clear shift of the dispersion curve of the SPPhP is predicted, when compared to the SPhP, effectively extending the GaAs Reststrahlen band with the now hybrid plasmonic/phononic modes.

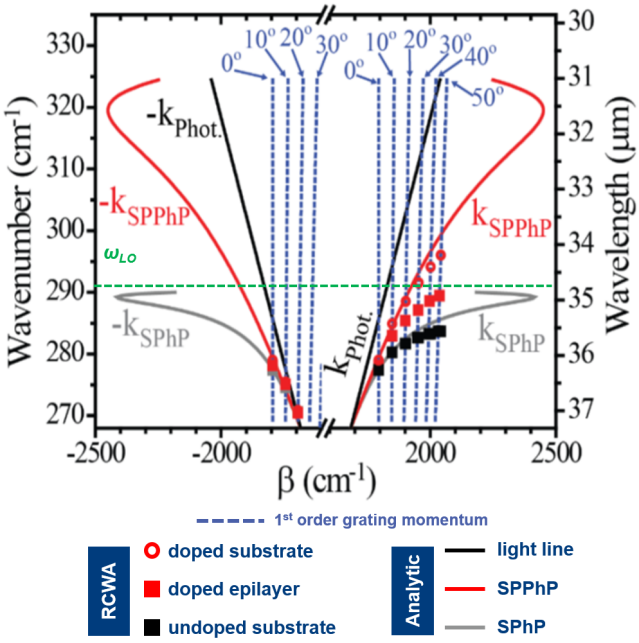

Figure 6.3: Calculated dispersion of semi-infinite phononic/air (gray) and hybrid (phononic/plasmonic)/air (red) interfaces. The black line shows the dispersion of the free-space photon, while the dashed blue lines show the sum of the grating momentum and incident photon momentum in the grating direction $k_{ph,x} + \frac{2\pi}{\Lambda}$, where Λ is the grating period. Coupling to the grating, as calculated by RCWA, is shown for the undoped Sample A (black squares), the doped epilayer of Sample B (red squares), and a hypothetical sample of infinite thickness, doped to the same concentrations as Sample B (red circles).

6.4 Reflectivity

Figure 6.4 shows the experimental and RCWA simulated TE-polarized reflection spectra for both the doped and undoped samples studied in this chapter. Though the observed experimental reflection dips are not quite as strong as those predicted in RCWA, most likely a result of fabrication-related variation in sample geometry or the finite angular spread of the incident light in our experimental apparatus, which can broaden the narrow (~ 4 cm^{-1}) coupling features, a clear signature of coupling to surface modes is experimentally observed, along with the splitting of the reflection dips as the sample is rotated about the surface normal.

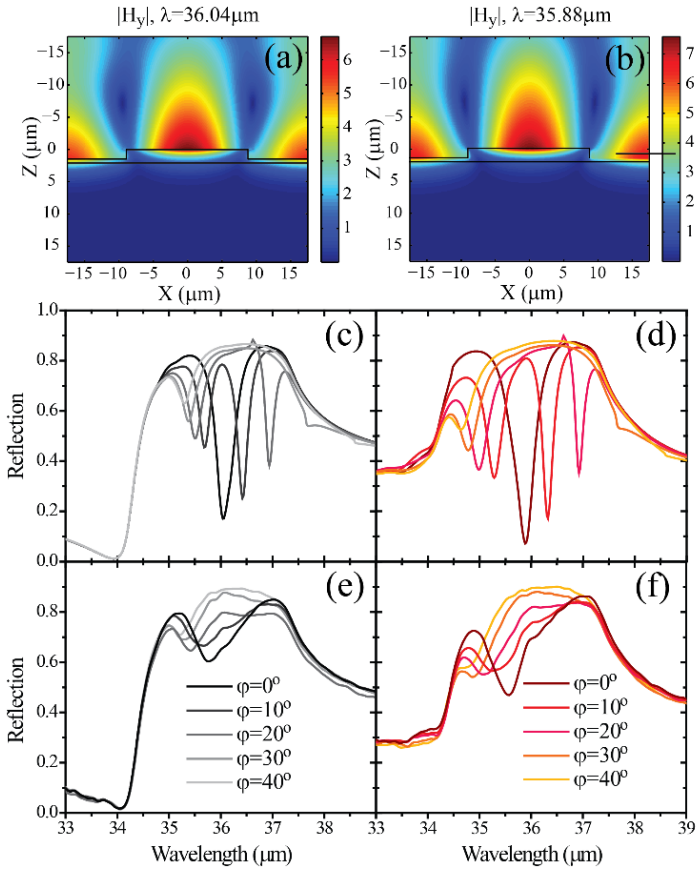

Figure 6.4: Magnetic field $\left|H_y\right|$ plots at $\lambda \sim 36$ µm and $\lambda \sim 35.9$ µm, corresponding to the normal incidence coupling wavelengths for the (a) undoped and (b) doped Samples A and B, respectively. TE-polarized (c, d) RCWA-simulated and (e, f) experimental reflection from (c, e) undoped SI GaAs (Sample A) and (d, f) 2 µm Si:GaAs $N_D = 6 \times 10^{17}$ cm^{-3} (Sample B). Each sample is patterned with a 1D grating with period $\Lambda = 35$ µm, ridge width $w = 18$ µm, and ridge depth $d = 1.4$ µm.

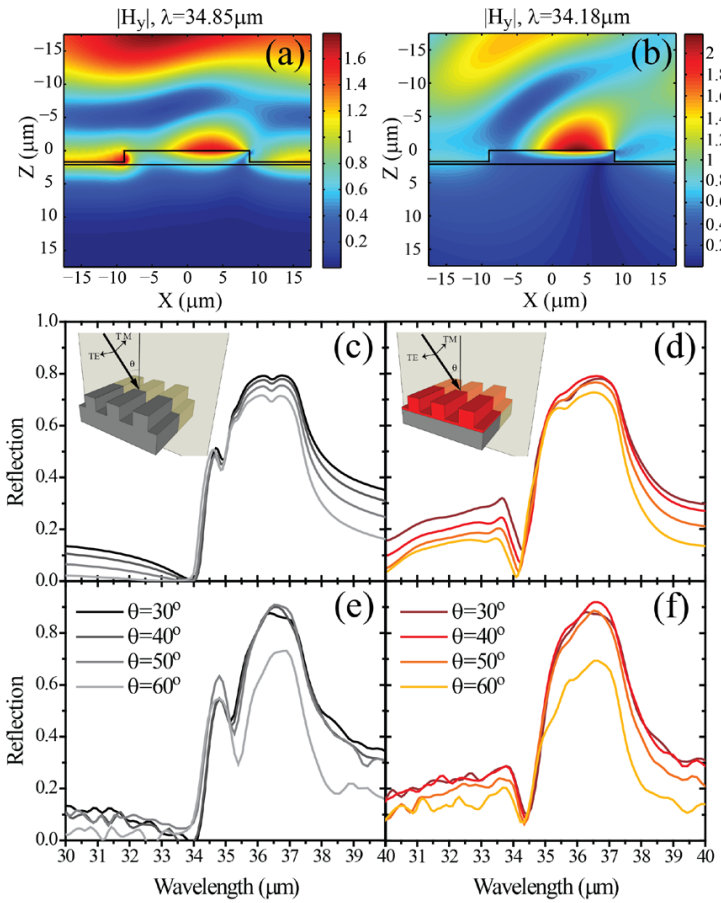

Figure 6.5: Magnetic field $|H_y|$ at $\lambda \sim 34.8$ µm and $\lambda \sim 34.2$ µm, for the (a) undoped and (b) doped sample, respectively, with light incident at 50° from normal. TM-polarized (c, d) RCWA-simulated and (e, f) experimental reflection from (c, e) undoped SI GaAs wafer and (d, f) 2 µm Si:GaAs $N_D = 6 \times 10^{17}$ cm^{-3} sample. Each sample is patterned with a 1D grating with period $\Lambda = 35$ µm and ridge width $w = 18$ µm and deep-etched ridge depth $d = 1.8$ µm. Insets in (c) and (d) show the experimental configuration.

In addition to being able to support SPPhP modes, our samples also display evidence for coupling to localized surface excitations. Figure 6.5 shows the TM-polarized, angle-dependent reflectivity from 1D grating samples with grating pitch $\Lambda = 35$ µm and ridge width $w = 18$ µm and deep-etched ridge depth $d = 1.8$ µm fabricated from Sample A (undoped SI wafer) and Sample B (2 µm Si:GaAs $N_D = 6 \times 10^{17}$ cm^{-3}). Strong dips in reflection are seen for Samples A and B at $\lambda \sim 34.8$ µm and $\lambda \sim 34.2$ µm, respectively. These features show no significant change with incidence angle (in stark contrast to the modes observed in Figures 6.3 and 6.4), and can thus be attributed to localized excitations supported on the patterned ridges. In the case of

the doped sample (B), the resonance results from a hybrid phonon/plasmon excitation, at or near the GaAs LO phonon energy, where undoped GaAs cannot support either localized or propagating surface phonon modes. RCWA simulations support our experimental data, with field profiles on resonance showing the strong field confinement achievable with our patterned surfaces, on resonance. In particular, the hybrid plasmonic/phononic sample shows a stronger resonance, as the substrate, at resonance, provides a low-loss, low-index material, while the undoped sample substrate has the same material properties as the ridge, weakening the simulated dip as well as the spatial localization of the mode. Our RCWA simulations agree well with our observed experimental data, with the exception of the stronger dips observed on the experimental reflection (Figure 6.5e), which may be the result of additional localization resulting from variations in the ridge width along each ridge, coming from fabrication related imperfections.

6.5 Discussion

In summary, we demonstrate coupling to FIR surface modes on GaAs materials. While the spectral range for coupling to pure surface phonon modes is limited to the range between the GaAs LO and TO phonon energies, we show that by lightly doping the GaAs, we are able to extend the spectral range in which coupling to both propagating and localized surface modes is allowed. Unlike heavily doped semiconductor materials, the surface modes supported on our lightly doped samples have equal contributions to permittivity from both free carriers and lattice vibrations, so that such modes can be characterized as hybrid plasmonic/phononic modes. We experimentally demonstrate coupling to both propagating and localized modes, and show good agreement between our experimental data and our simulated results. We show that the localized and propagating hybrid phonon/plasmon modes can be supported at higher energies than their purely phononic counterparts, demonstrating resonances aligned with the GaAs LO phonon energy, which cannot be achieved in a purely phononic material. The results presented offer a mechanism for extending the Reststrahlen bands of semiconductor materials and potentially providing a bridge between LO phonons and free space photons at the same energy.

Chapter 7

Strong Thermal Emission of the Berreman Mode

In this chapter, we present preliminary data that demonstrates strong TM-polarized selective thermal emission from an unpatterned sample of thin-film AlN. We attribute this emission to an absorption resonance known as the Berreman mode [135]. The Berreman mode is observed in polar semiconductors near the energy of the material's LO phonon. When the material is deposited as a film upon a metallic substrate, the strong absorption is evident in TM-polarized reflectivity measurements, while absent in TE-polarized measurements. Early descriptions of the Berreman mode attributed it to a resonance of the LO phonon itself [136,137], but later work explained the phenomenon in terms of interface polariton modes [138] or, more specifically, leaky polariton modes [139].

The interface mode associated with the Berreman is described in [138] as a Fano-type double interface surface polariton mode, which propagates along the adjacent pair of interfaces in the dielectric/phononic/plasmonic (i.e. air/semiconductor/metal) stack of materials and decays exponentially away from the interfaces. The authors in [138] analyzed a lossless dispersion model for the Berreman mode, but both the metallic substrate and the Reststrahlen band region of the semiconductor have significant material losses, which cause the mode to decay in the direction of propagation as well. Further analysis of the Berreman mode in [139] highlights the lack of any surface grating in the observation of the Berreman mode, which would be necessary were the mode to have momentum values greater than the linear dispersion of a free space photon. In other words, the dispersion relation of the Berreman mode must have momentum values bound above by the light line. Such surface polariton modes are known as "leaky polariton" modes since they lose energy by radiating into free space as well by absorption due to material losses. The

This chapter presents preliminary experimental results. Galen Harden of Prof. Anthony Hoffman's research group performed the Raman spectroscopy measurements.

coupling efficiency of the Berreman mode is sensitive to the thickness of the semiconductor film as well as the angle of incidence of the probing light [140].

The sample under investigation was a bare, unpatterned 1200 nm thin film of AlN grown on a ground plane of optically thick molybdenum on a silicon substrate. The sample was, in fact, the same source material used in Chapter 4 — already a convenient size with a suitable film thickness atop a metallic ground plane. The models and methods used to calculate the permittivity of the materials and expected absorptivity/emissivity spectra were likewise the same as those used in Section 4.2.

7.1 Angle-Resolved Thermal Emissivity

Thermal emission measurements were taken using a Bruker v80v FTIR spectrometer with a KBr beamsplitter and MCT detector as described in Section 2.3. The sample was mounted externally on a hot plate, and emitted light was spatially filtered and collected using an off-axis gold parabolic mirror with polarization selected by a KRS-5 wire grid polarizer. The hot plate was mounted onto a rotational base in such a manner that its rotational axis aligned with the front face of the hot plate where the sample was mounted via metal clamps. This permitted the sample and hot plate to be rotated together allowing measurments of emission spectra at various angles of emission. The angles of emission ranged from from 0° to 70° in steps of 5°. The hot plate was held by a feedback stabilized temperature controller at a temperature of 200 °C. The emission spectra were normalized using a "black soot" reference sample, fabricated in the same manner as described in Section 4.4, and with an emissivity previously measured via MIR reflection spectroscopy using the Pike 10Spec apparatus (see Section 2.2.1). Thermal background measurements were taken with the port of the spectrometer open and cold. These background measurements were subtracted from the sample spectra and those of the reference sample before normalizing the sample emission spectra, yielding angle-dependent emissivity measurements.

Figure 7.1 depicts contour maps of the measured (a,b) and calculated (c,d) with TM- (a,c) and TE-polarization (b,d). The anticipated Berreman mode is present in the TM-polarized spectra, while absent in the TE-polarized spectra, as expected. The peak of the Berreman mode occupies a narrow band from

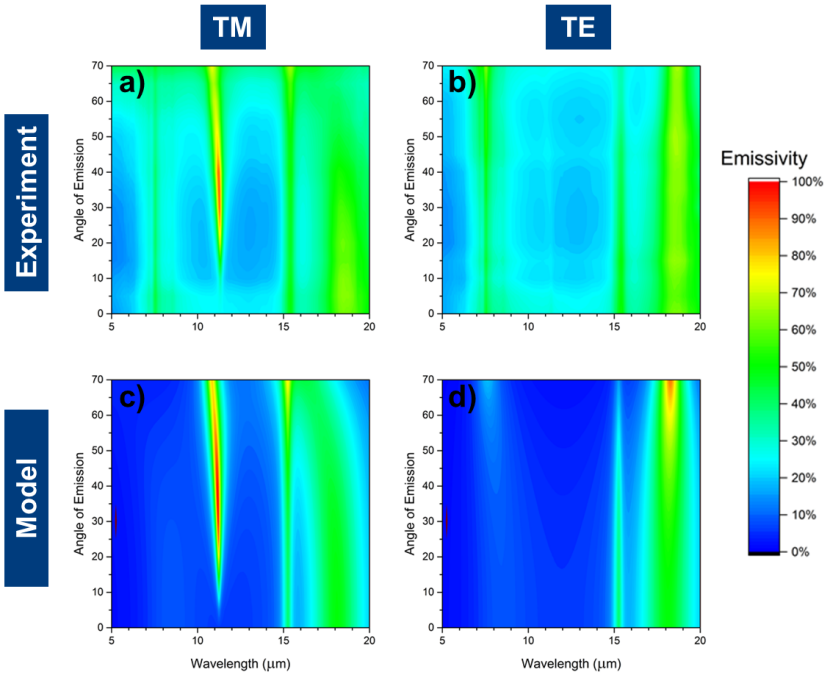

Figure 7.1: Measured (a,b) and calculated (c,d) emissivity for AlN film at various angles of emission. The strong emission band present in the TM-polarized (a,c) spectra is attributed to the Berreman mode. The band is absent in the TE-polarized (b,d) spectra as would be expected for this mode. The maximum emission occurs at an angle of incidence of 35° and $\lambda = 11.25$ μm (889 cm^{-1}).

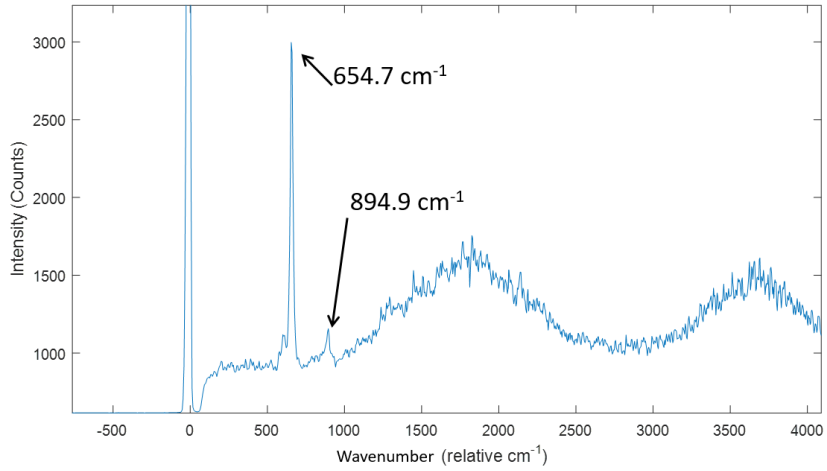

Figure 7.2: Raman spectrum of 1200 nm AlN film on molybdenum ground-plane. The stronger peak at $\bar{\nu} = 654.7$ cm^{-1} corresponds to the TO phonon energy, while the weaker peak at $\bar{\nu} = 894.9$ cm^{-1} corresponds to the LO phonon energy.

11.32 µm to 10.85 µm (883 cm^{-1} to 922 cm^{-1}). The measured emissivity spectra display a higher thermal background than expected, possibly due to inadequate spatial filtering by the aperature of the hot plate's thermal emission. Additionally, the measured spectra exhibit a broad, slightly dispersive, and polarization-independent emission band of moderate strength centered at $\lambda = 7.5$ µm, which is largely absent in the calculated spectra. This discrepancy may, however, be exacerbated by the undercorrected thermal background measurement.

We also examined our samples using Raman spectroscopy. Samples were excited with a 488 nm laser with a power of 6.85 mW. The measured Raman spectrum confirms the expected energies of the TO and LO phonon as shown in Figure 7.2. Moreover, the measured energy of the LO phonon lies in the narrow range occupied by the Berreman mode observed in the thermal emission spectra.

7.2 Discussion

Further investigation of these results should include emissivity measurements of the samples with different thicknesses as the dispersion relations of the polariton modes would be expected to have significant dependence on the thickness of the phononic film, as well as an attempt at analytically describing the dispersion of the observed polariton modes.

Despite the higher-energy Reststrahlen band of AlN, which lies above the FIR region that is the focus of this dissertation, we expect these results to be generally applicable at longer wavelengths in the Reststrahlen bands of common semiconductors. Moreover, epitaxial growth of these materials would permit additional permittivity modifications through heavy doping (for growth of metallic groundplanes) or light doping (to support hybrid polariton modes as discussed in Chapter 6). Follow-up investigations might also consider incorporating structures such as quantum wells or quantum cascades tuned to resonate at the LO phonon energy, as such structures might have the potential to complete a linkage between optical phonon generation and free space photon emission — fulfilling the breakthrough goal of the work described in this dissertation.

Chapter 8

Conclusion and Future Work

8.1 Summary

This dissertation explores several pathways toward the development of novel materials and light sources operating in the FIR region of the electromagnetic spectrum. This region has been largely underserved by available technology despite investigations into its potentially unique value in the advancement of fields such as astronomy, medicine, and the petrochemical industry. The first phase of the dissertation focused on demonstrating selective thermal emitters operating in the FIR by extrapolating some successes at shorter wavelengths in the MIR wavelength range. This approach culminated in the successful demonstration of a strong, tunable and selective thermal absorber/emitter structure composed of a thin film of aluminum nitride atop a metal ground plane and beneath 1D and 2D gold gratings. The absorption resonances could be easily and robustly tuned across a wide wavelength range in the FIR simply by adjusting the width of the gold gratings. Modeled emission calculations estimated the power efficiency of the structures significantly surpassed that of a comparable blackbody source.

Despite the success of these exciting results, any thermal emitter is bounded in its power output, within any particular wavelength band, by that of a blackbody source. Operating the device will always require emitting in bands outside the desired one. This is all the more true in the FIR, since the more power put into a thermal emitter to raise its temperature, the smaller the proportion of that power that will be emitted at longer wavelengths. Thus, this conundrum begs for an alternative approach to achieving genuinely efficient and selective emitters operating in the FIR.

To this end, the next phase of the dissertation explored a potential mechanism of FIR light generation by investigating the possibility of coupling

optical phonons to free space photons via surface polariton modes within the Reststrahlen bands of common semiconductors. They key motivation in this approach is the ease with which LO phonons can be generated in the bulk of semiconductors via the relaxation of optically or electronically excited electrons. Unfortunately, another fundamental limitation seems to stand in opposition to such an approach; namely, that photons (a transverse oscillation of the electromagnetic field) do not couple, in bulk, to LO phonons. However, we investigate two examples — hybrid surface polaritons and the Berreman mode — of strong emission/absorption near the LO phonon energy of a semiconductor. These results suggest that such modes might, under further investigation, yield a critical bridge between copious LO phonon populations in bulk and free space light emission in the FIR region of the electromagnetic spectrum.

8.2 Future Work

8.2.1 Reststrahlen Band Engineering

As previously depicted in Figure 1.5, much of the FIR wavelength range can be covered by the Reststrahlen bands of several common III-V semiconductors. Future investigations should investigate how Reststrahlen bands might be tuned to cover specific FIR wavelengths through judicious application of III-V alloys in an approach analogous to the band-gap engineering so common place in optoelectronics today. The optical phonon energy can be modified by changing the composition of semiconductor alloys [141]. The LO phonon energy of the ternary semiconductor InGaAs can be tuned from 36 meV to 29 meV as the gallium fraction changes from 100% (GaAs) to 0% (InAs). The LO phonon energy can also be altered by designing superlattices (SLs), which have been shown to have phonon energies distinct from the SLs constituent materials [142–145]. The phonons associated with SLs are known as interface phonons, and their energy and other properties can be controlled by the dimensions of the SL — namely, altering the width of its barriers and wells. The tuning of the interface phonon energy is depicted in Figure 8.1c, wherein the SL well width is changed relative to a fixed barrier width. Two possible structures used to control coupling between optical phonons and surface modes

are also depicted in Figure 8.1 — one using phonon energies determined by alloy composition (a) and another using SL interface phonons (b). Research groups who have specialized in growing epitaxial films in these material systems may find this line of investigation to be an exciting new research opportunity. Such groups and their collaborators would be well advised to pursue the concomitant development of new computational models to facilitate the design of materials with engineered phonon energies. Additionally, they will need to possess or acquire a strong competency in the use of FIR Raman spectroscopy for the purpose of analyzing phonon energies and populations present in this new class of materials.

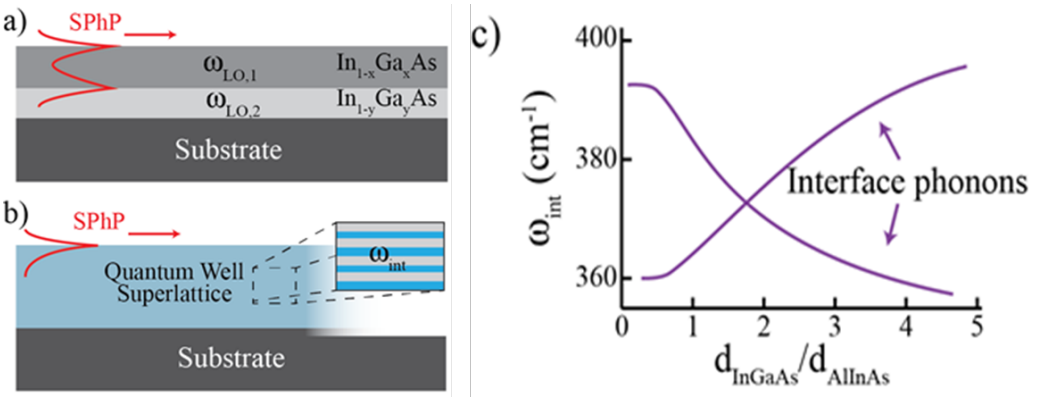

Figure 8.1: (a) Heterostructure using two different alloy compositions. The LO phonon frequency in the second layer is degenerate with the SPhP energy. (b) Schematic of a QW heterostructure supporting interface phonons at ω_{int}. (c) Depiction of the interface phonon frequency versus well width for a fixed barrier width.

8.2.2 Generation of Non-Equilibrium Phonons

Another important line of investigation for the development of novel FIR optical architecture will be the dynamics of generating non-equilibrium phonon populations via processes such as photo-excitation of electrons and quantum cascade (QC) heterostructures. The hot electrons, produced by photo-excitation, will subsequently relax and scatter to generate optical phonons - a process which has been shown to be capable of generating non-equilibrium populations of both bulk and interface phonons [146–150]. The optical generation of phonons via hot electrons is depicted schematically in Figure 8.2a.

Quantum cascade heterostructures could be used to electrically generate LO phonons. Similar structures are routinely employed in QCLs to efficiently depopulate the lower laser level and shuttle the electron into the next stage of the cascade [151]. Such structures have the additional advantage of generating one LO phonon per stage from the same injected electron and have been shown capable of generating non-equilibrium phonon populations [152, 153]. Such a proposed structure is depicted in Figure 8.2b.

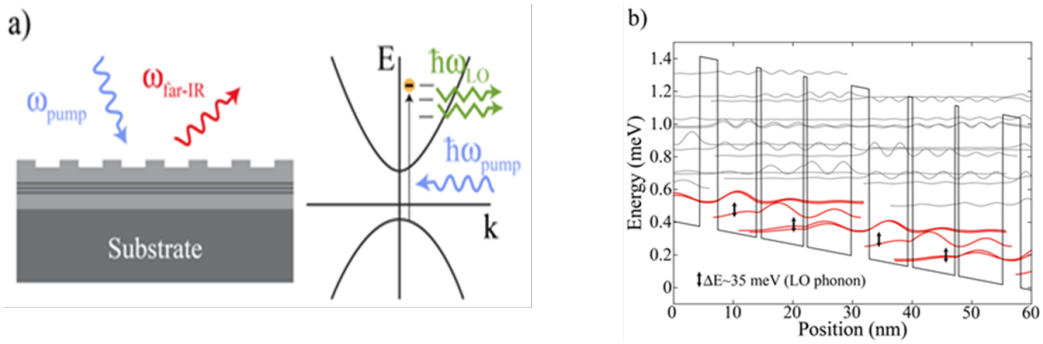

Figure 8.2: (a) Left: Schematic of a sample for generating phonons using optical pumping. The QWs absorb the pump photons and the rest of the sample is transparent. Right: Energy band showing the excitation of hot electrons via the pump laser and relaxation via LO phonon emission. (b) A three-well QC phonon active region. Relevant wavefunctions are in red and the vertical arrows indicate electron transitions that generate LO phonons.

8.2.3 Electrical Generation and Device Integration

The more mature stages of investigation into the development of FIR optical architecture should pursue the integration of previously presented and suggested work into potentially practical devices. Initial phases of development might use photo-excitation to drive non-equilibrium phonon populations within these devices, while final phases of development should seek to electrically generate phonons and fully integrate previous phases into compact, technologically viable devices. Schematics of potential integrated designs are depicted in Figure 8.3. The blue and gray regions indicate QC phonon emitters, electrically driven by gold contacts. The first configuration (a) might out-couple FIR light via gratings and SPPhP modes, while the second (b) might out-couple FIR light via leaky polariton modes.

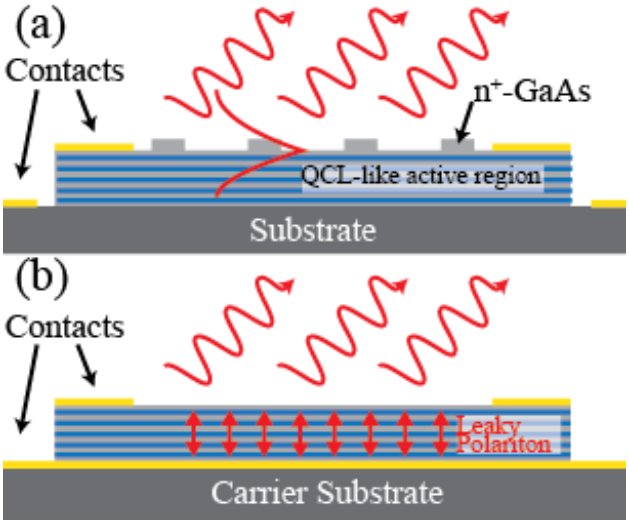

Figure 8.3: Schematics of electrically-pumped emitter devices using (a) SPhPP and (b) leaky polariton modes. The alternating blue/gray regions represent coupled quantum wells, contacts are shown in gold, the surface wave and emitted photons are shown in red.

8.3 Conclusion

The FIR region of the electromagnetic spectrum stands as one of the last optical frontiers. This wavelength region is served by a minimal assortment of optical components with greater cost and more limited capabilities when compared with the mature optical architecture that serves the shorter wavelength regions. The dearth of FIR optical technology, which enables little more than basic research and development, surely hinders the advancement of potentially unique FIR applications. As such, interest in the field is disparate and lacks any common vision for guiding, shaping, and sharing new research efforts. It is the hope of this author that the achievements and future goals described in this dissertation will pique the interest and curiosity of other able and motivated research groups and promote the founding of a scientific community dedicated to pursuing the exciting work of developing a more capable and robust FIR optical architecture. This research effort offers rich opportunities for investigating fundamental science as well as developing new technologies and the concomitant applications made possible by these efforts.

References

[1] R. Colombelli, F. Capasso, C. Gmachl, A. L. Hutchinson, D. L. Sivco, A. Tredicucci, M. C. Wanke, A. M. Sergent, and A. Y. Cho, "Far-infrared surface-plasmon quantum-cascade lasers at 21.5 µm and 24 µm wavelengths," *Applied Physics Letters*, vol. 78, no. 18, pp. 2620–2622, 2001.

[2] E. S. Koteles and W. R. Datars, "Two-phonon absorption in InSb, InAs, and GaAs," *Canadian Journal of Physics*, vol. 54, no. 16, pp. 1676–1691, 1976.

[3] G. Sun, R. A. Soref, and J. B. Khurgin, "Active region design of a terahertz GaN/ $Al_{0.15}Ga_{0.85}N$ quantum cascade laser," *Superlattices and Microstructures*, vol. 37, no. 2, pp. 107–113, 2005.

[4] O. Pirali, N.-T. Van-Oanh, P. Parneix, M. Vervloet, and P. Brechignac, "Far-infrared spectroscopy of small polycyclic aromatic hydrocarbons," *Physical Chemistry Chemical Physics*, vol. 8, no. 32, pp. 3707–3714, 2006.

[5] A. Leger and J. Puget, "Identification of the unidentified IR emission features of interstellar dust?" *Astron. Astrophys.*, vol. 137, pp. L5–L8, 1984.

[6] K. H. Michaelian, Q. Wen, B. E. Billinghurst, J. M. Shaw, and V. Lastovka, "Far- and mid-infrared photoacoustic spectra of tetracene, pentacene, perylene and pyrene," *Vibrational Spectroscopy*, vol. 58, pp. 50–56, 2012.

[7] J. C. Mather, D. J. Fixsen, R. A. Shafer, C. Mosier, and D. T. Wilkinson, "Calibrator design for the cobe far infrared absolute spectrophotometer (FIRAS)," *The Astrophysical Journal*, vol. 512, no. 2, p. 511, 1999.

[8] B. K. Wilt, W. T. Welch, and J. G. Rankin, "Determination of asphaltenes in petroleum crude oils by fourier transform infrared spectroscopy," *Energy & Fuels*, vol. 12, no. 5, pp. 1008–1012, 1998.

[9] F. Cataldo, D. A. Garca-Hernndez, and A. Manchado, "Far- and mid-infrared spectroscopy of complex organic matter of astrochemical interest: coal, heavy petroleum fractions and asphaltenes," *Monthly Notices of the Royal Astronomical Society*, vol. 429, no. 4, pp. 3025–3039, 2013.

[10] G. Dickakian and S. Seay, "Asphaltene precipitation primary crude exchanger fouling mechanism," *Oil & Gas Journal*, vol. 47, pp. 47–50, 1988.

[11] M. R. Kutteruf, C. M. Brown, L. K. Iwaki, M. B. Campbell, T. M. Korter, and E. J. Heilweil, "Terahertz spectroscopy of short-chain polypeptides," *Chemical Physics Letters*, vol. 375, no. 34, pp. 337–343, 2003.

[12] S. A. Maier and H. A. Atwater, "Plasmonics: Localization and guiding of electromagnetic energy in metal/dielectric structures," *Journal of Applied Physics*, vol. 98, no. 1, 2005.

[13] W. A. Murray and W. L. Barnes, "Plasmonic materials," *Advanced Materials*, vol. 19, no. 22, pp. 3771–3782, 2007.

[14] S. A. Maier, *Plasmonics: Fundamentals and Applications*. Springer US, 2007.

[15] G. V. Naik, J. Kim, and A. Boltasseva, "Oxides and nitrides as alternative plasmonic materials in the optical range [invited]," *Optical Materials Express*, vol. 1, no. 6, pp. 1090–1099, 2011.

[16] G. V. Naik, J. Liu, A. V. Kildishev, V. M. Shalaev, and A. Boltasseva, "Demonstration of Al:ZnO as a plasmonic component for near-infrared metamaterials," *Proceedings of the National Academy of Sciences of the United States of America*, vol. 109, no. 23, pp. 8834–8838, 2012.

[17] G. V. Naik, J. L. Schroeder, X. Ni, A. V. Kildishev, T. D. Sands, and A. Boltasseva, "Titanium nitride as a plasmonic material for visible and near-infrared wavelengths," *Optical Materials Express*, vol. 2, no. 4, pp. 478–489, 2012.

[18] J. W. Cleary, R. E. Peale, D. J. Shelton, G. D. Boreman, C. W. Smith, M. Ishigami, R. Soref, A. Drehman, and W. R. Buchwald, "IR permittivities for silicides and doped silicon," *Journal of the Optical Society of America B: Optical Physics*, vol. 27, no. 4, pp. 730–734, 2010.

[19] J. W. Cleary, W. H. Streyer, N. Nader, S. Vangala, I. Avrutsky, B. Claflin, J. Hendrickson, D. Wasserman, R. E. Peale, W. Buchwald, and R. Soref, "Platinum germanides for mid- and long-wave infrared plasmonics," *Optics Express*, vol. 23, no. 3, pp. 3316–3326, 2015.

[20] J. C. Ginn, R. L. Jarecki Jr, E. A. Shaner, and P. S. Davids, "Infrared plasmons on heavily-doped silicon," *Journal of Applied Physics*, vol. 110, no. 4, 2011.

[21] M. Shahzad, G. Medhi, R. E. Peale, W. R. Buchwald, J. W. Cleary, R. Soref, G. D. Boreman, and O. Edwards, "Infrared surface plasmons on heavily doped silicon," *Journal of Applied Physics*, vol. 110, no. 12, 2011.

[22] W. Streyer, S. Law, G. Rooney, T. Jacobs, and D. Wasserman, "Strong absorption and selective emission from engineered metals with dielectric coatings," *Optics Express*, vol. 21, no. 7, pp. 9113–9122, 2013.

[23] A. Rosenberg, J. Surya, R. Liu, W. Streyer, S. Law, L. Suzanne Leslie, R. Bhargava, and D. Wasserman, "Flat mid-infrared composite plasmonic materials using lateral doping-patterned semiconductors," *Journal of Optics (United Kingdom)*, vol. 16, no. 9, 2014.

[24] S. Law, L. Yu, and D. Wasserman, "Epitaxial growth of engineered metals for mid-infrared plasmonics," *Journal of Vacuum Science and Technology B: Nanotechnology and Microelectronics*, vol. 31, no. 3, 2013.

[25] S. Law, R. Liu, and D. Wasserman, "Doped semiconductors with band-edge plasma frequencies," *Journal of Vacuum Science and Technology B: Microelectronics and Nanometer Structures*, vol. 32, no. 5, 2014.

[26] V. Ntsame Guilengui, L. Cerutti, J. B. Rodriguez, E. Tourni, and T. Taliercio, "Localized surface plasmon resonances in highly doped semiconductors nanostructures," *Applied Physics Letters*, vol. 101, no. 16, 2012.

[27] E. Sachet, C. T. Shelton, J. S. Harris, B. E. Gaddy, D. L. Irving, S. Curtarolo, B. F. Donovan, P. E. Hopkins, P. A. Sharma, A. L. Sharma, J. Ihlefeld, S. Franzen, and J.-P. Maria, "Dysprosium-doped cadmium oxide as a gateway material for mid-infrared plasmonics," *Nat Mater*, vol. 14, no. 4, pp. 414–420, 2015.

[28] N. Ashcroft and N. Mermin, *Solid State Physics*. United States: Thomson Learning, Inc., 1976.

[29] C. Kittel, *Introduction to Solid State Physics*, 7th ed. New York: John Wiley & Sons, Inc., 1996.

[30] K. Feng, W. Streyer, Y. Zhong, A. J. Hoffman, and D. Wasserman, "Photonic materials, structures and devices for reststrahlen optics," *Optics Express*, vol. 23, no. 24, pp. A1418–A1433, 2015.

[31] J. D. Caldwell, L. Lindsay, V. Giannini, I. Vurgaftman, T. L. Reinecke, S. A. Maier, and O. J. Glembocki, "Low-loss, infrared and terahertz nanophotonics using surface phonon polaritons," *Nanophotonics*, vol. 4, no. 1, pp. 44–68, 2015.

[32] Z. Jacob, "Nanophotonics: Hyperbolic phonon-polaritons," *Nat Mater*, vol. 13, no. 12, pp. 1081–1083, 2014.

[33] J. J. Greffet, R. Carminati, K. Joulain, J. P. Mulet, S. Mainguy, and Y. Chen, "Coherent emission of light by thermal sources," *Nature*, vol. 416, no. 6876, pp. 61–64, 2002.

[34] A. Huber, N. Ocelic, D. Kazantsev, and R. Hillenbrand, "Near-field imaging of mid-infrared surface phonon polariton propagation," *Applied Physics Letters*, vol. 87, no. 8, p. 081103, 2005.

[35] A. J. Huber, B. Deutsch, L. Novotny, and R. Hillenbrand, "Focusing of surface phonon polaritons," *Applied Physics Letters*, vol. 92, no. 20, 2008.

[36] B. Neuner III, D. Korobkin, C. Fietz, D. Carole, G. Ferro, and G. Shvets, "Critically coupled surface phonon-polariton excitation in silicon carbide," *Optics Letters*, vol. 34, no. 17, pp. 2667–2669, 2009.

[37] T. Wang, P. Li, B. Hauer, D. N. Chigrin, and T. Taubner, "Optical properties of single infrared resonant circular microcavities for surface phonon polaritons," *Nano Letters*, vol. 13, no. 11, pp. 5051–5055, 2013.

[38] J. D. Caldwell, O. J. Glembocki, Y. Francescato, N. Sharac, V. Giannini, F. J. Bezares, J. P. Long, J. C. Owrutsky, I. Vurgaftman, J. G. Tischler, V. D. Wheeler, N. D. Bassim, L. M. Shirey, R. Kasica, and S. A. Maier, "Low-loss, extreme subdiffraction photon confinement via silicon carbide localized surface phonon polariton resonators," *Nano Letters*, vol. 13, no. 8, pp. 3690–3697, 2013.

[39] S. Dai, Z. Fei, Q. Ma, A. S. Rodin, M. Wagner, A. S. McLeod, M. K. Liu, W. Gannett, W. Regan, K. Watanabe, T. Taniguchi, M. Thiemens, G. Dominguez, A. H. C. Neto, A. Zettl, F. Keilmann, P. Jarillo-Herrero, M. M. Fogler, and D. N. Basov, "Tunable phonon polaritons in atomically thin van der Waals crystals of boron nitride," *Science*, vol. 343, no. 6175, pp. 1125–1129, 2014.

[40] J. D. Caldwell, A. V. Kretinin, Y. Chen, V. Giannini, M. M. Fogler, Y. Francescato, C. T. Ellis, J. G. Tischler, C. R. Woods, A. J. Giles, M. Hong, K. Watanabe, T. Taniguchi, S. A. Maier, and K. S. Novoselov, "Sub-diffractional volume-confined polaritons in the natural hyperbolic material hexagonal boron nitride," *Nat Commun*, vol. 5, 2014.

[41] D. Heitmann and H. Raether, "Light emission of nonradiative surface plasmons from sinusoidally modulated silver surfaces," *Surface Science*, vol. 59, no. 1, pp. 17–22, 1976.

[42] J. C. Weeber, Y. Lacroute, and A. Dereux, "Optical near-field distributions of surface plasmon waveguide modes," *Physical Review B - Condensed Matter and Materials Physics*, vol. 68, no. 11, pp. 1 154 011–11 540 110, 2003.

[43] D. J. Bergman and M. I. Stockman, "Surface plasmon amplification by stimulated emission of radiation: Quantum generation of coherent surface plasmons in nanosystems," *Physical Review Letters*, vol. 90, no. 2, pp. 027 402/1–027 402/4, 2003.

[44] M. T. Hill, M. Marell, E. S. P. Leong, B. Smalbrugge, Y. Zhu, M. Sun, P. J. Van Veldhoven, E. J. Geluk, F. Karouta, Y. S. Oei, R. Ntzel, C. Z. Ning, and M. K. Smit, "Lasing in metal-insulator-metal subwavelength plasmonic waveguides," *Optics Express*, vol. 17, no. 13, pp. 11 107–11 112, 2009.

[45] R. F. Oulton, V. J. Sorger, T. Zentgraf, R. M. Ma, C. Gladden, L. Dai, G. Bartal, and X. Zhang, "Plasmon lasers at deep subwavelength scale," *Nature*, vol. 461, no. 7264, pp. 629–632, 2009.

[46] M. A. Noginov, G. Zhu, A. M. Belgrave, R. Bakker, V. M. Shalaev, E. E. Narimanov, S. Stout, E. Herz, T. Suteewong, and U. Wiesner, "Demonstration of a spaser-based nanolaser," *Nature*, vol. 460, no. 7259, pp. 1110–1112, 2009.

[47] P. B. Johnson and R. W. Christy, "Optical constants of the noble metals," *Physical Review B*, vol. 6, no. 12, pp. 4370–4379, 1972.

[48] S. Law, V. Podolskiy, and D. Wasserman, "Towards nano-scale photonics with micro-scale photons: The opportunities and challenges of mid-infrared plasmonics," *Nanophotonics*, vol. 2, no. 2, p. 103130, 2013.

[49] J. B. Khurgin, "How to deal with the loss in plasmonics and metamaterials," *Nat Nano*, vol. 10, no. 1, pp. 2–6, 2015.

[50] S. Law, D. C. Adams, A. M. Taylor, and D. Wasserman, "Mid-infrared designer metals," *Optics Express*, vol. 20, no. 11, pp. 12 155–12 165, 2012.

[51] G. Shkerdin, S. Rabbaa, J. Stiens, and R. Vounckx, "Free-electron absorption in n-doped GaN semiconductors at mid-IR wavelengths in the strong phononplasmon coupling regime," *Journal of Physics D: Applied Physics*, vol. 45, no. 49, p. 495103, 2012.

[52] E. Hecht, *Optics*, 4th ed. San Francisco, CA: Addison-Wesley, 2002.

[53] B. C. Smith, *Fundamentals of Fourier Transform Infrared Spectrometry*, 2nd ed. Boca Raton, FL: CRC Press, 2001.

[54] P. R. Griffiths and J. A. de Haseth, *Fourier Transform Infrared Spectrometry*, 2nd ed. Hoboken, New Jersey: John Wiley & Sons, Inc., 2007.

[55] Bruker Optics, "VERTEX Series: Advanced Research FT-IR Spectrometers," https://www.bruker.com/products/infrared-near-infrared-and-raman-spectroscopy/ft-ir-research-spectrometers/vertex-series/vertex-8080v/overview.html, 2013, retrieved November 6, 2016.

[56] Pike Technologies, "10Spec — Near-normal Sample Reflectivity Measurements," https://www.piketech.com/files/pdfs/10SpecPDS1313.pdf, 2013, retrieved November 16, 2016.

[57] Bruker Optics, "HYPERION Series: FT-IR Microscopes," https://www.bruker.com/products/infrared-near-infrared-and-raman-spectroscopy/ft-ir-microscopes-raman-microscopes/hyperion/overview.html, 2013, retrieved November 18, 2016.

[58] Pike Technologies, "VeeMAX III — The Ultimate Variable Angle Specular Reflectance Accessory," https://www.piketech.com/files/pdfs/VeeMAXPDS1313.pdf, 2013, retrieved November 19, 2016.

[59] B. E. A. Saleh and M. C. Teich, *Fundamentals of Photonics*. Hoboken, NJ: Wiley, 1991.

[60] C. Roberts and V. Podolskiy, http://viktor-podolskiy-research.wiki.uml.edu/RCWA, 2015, MATLAB implementation of the RCWA numerical method from the V. Podolskiy Research Group.

[61] M. G. Moharam and T. K. Gaylord, "Rigorous coupled-wave analysis of planar-grating diffraction," *Journal of the Optical Society of America*, vol. 71, no. 7, pp. 811–818, 1981.

[62] M. G. Moharam, T. K. Gaylord, E. B. Grann, and D. A. Pommet, "Formulation for stable and efficient implementation of the rigorous coupled-wave analysis of binary gratings," *Journal of the Optical Society of America A*, vol. 12, no. 5, pp. 1068–1076, 1995.

[63] R. Rumpf, "EE 5320: Computational Electromagnetics," http://emlab.utep.edu/ee5390cem.htm, 2012, lectures 21 – 23.

[64] N. I. Landy, S. Sajuyigbe, J. J. Mock, D. R. Smith, and W. J. Padilla, "Perfect metamaterial absorber," *Physical Review Letters*, vol. 100, no. 20, 2008.

[65] Y. Avitzour, Y. A. Urzhumov, and G. Shvets, "Wide-angle infrared absorber based on a negative-index plasmonic metamaterial," *Physical Review B - Condensed Matter and Materials Physics*, vol. 79, no. 4, 2009.

[66] N. Liu, M. Mesch, T. Weiss, M. Hentschel, and H. Giessen, "Infrared perfect absorber and its application as plasmonic sensor," *Nano Letters*, vol. 10, no. 7, pp. 2342–2348, 2010.

[67] J. A. Mason, S. Smith, and D. Wasserman, "Strong absorption and selective thermal emission from a midinfrared metamaterial," *Applied Physics Letters*, vol. 98, no. 24, 2011.

[68] C. Wu, B. Neuner, G. Shvets, J. John, A. Milder, B. Zollars, and S. Savoy, "Large-area wide-angle spectrally selective plasmonic absorber," *Physical Review B - Condensed Matter and Materials Physics*, vol. 84, no. 7, 2011.

[69] Z. H. Jiang, S. Yun, F. Toor, D. H. Werner, and T. S. Mayer, "Conformal dual-band near-perfectly absorbing mid-infrared metamaterial coating," *ACS Nano*, vol. 5, no. 6, pp. 4641–4647, 2011.

[70] K. Aydin, V. E. Ferry, R. M. Briggs, and H. A. Atwater, "Broadband polarization-independent resonant light absorption using ultrathin plasmonic super absorbers," *Nature Communications*, vol. 2, no. 1, 2011.

[71] J. A. Mason, G. Allen, V. A. Podolskiy, and D. Wasserman, "Strong coupling of molecular and mid-infrared perfect absorber resonances," *IEEE Photonics Technology Letters*, vol. 24, no. 1, pp. 31–33, 2012.

[72] W. W. Salisbury, "Absorbent body for electromagnetic waves," US Patent 2,599,944, 1952.

[73] M. A. Kats, R. Blanchard, P. Genevet, and F. Capasso, "Nanometre optical coatings based on strong interference effects in highly absorbing media," *Nature Materials*, vol. 12, no. 1, pp. 20–24, 2013.

[74] M. A. Kats, D. Sharma, J. Lin, P. Genevet, R. Blanchard, Z. Yang, M. M. Qazilbash, D. N. Basov, S. Ramanathan, and F. Capasso, "Ultra-thin perfect absorber employing a tunable phase change material," *Applied Physics Letters*, vol. 101, no. 22, 2012.

[75] W. Streyer, K. Feng, Y. Zhong, A. J. Hoffman, and D. Wasserman, "Selective absorbers and thermal emitters for far-infrared wavelengths," *Applied Physics Letters*, vol. 107, no. 8, p. 081105, 2015.

[76] K. Ellmer and R. Mientus, "Carrier transport in polycrystalline ITO and ZnO:Al II: The influence of grain barriers and boundaries," *Thin Solid Films*, vol. 516, no. 17, pp. 5829–5835, 2008.

[77] M. U. Pralle, N. Moelders, M. P. McNeal, I. Puscasu, A. C. Greenwald, J. T. Daly, E. A. Johnson, T. George, D. S. Choi, I. El-Kady, and R. Biswas, "Photonic crystal enhanced narrow-band infrared emitters," *Applied Physics Letters*, vol. 81, no. 25, pp. 4685–4687, 2002.

[78] K. Ikeda, H. T. Miyazaki, T. Kasaya, K. Yamamoto, Y. Inoue, K. Fujimura, T. Kanakugi, M. Okada, K. Hatade, and S. Kitagawa, "Controlled thermal emission of polarized infrared waves from arrayed plasmon nanocavities," *Applied Physics Letters*, vol. 92, no. 2, 2008.

[79] J. A. Mason, D. C. Adams, Z. Johnson, S. Smith, A. W. Davis, and D. Wasserman, "Selective thermal emission from patterned steel," *Optics Express*, vol. 18, no. 24, pp. 25 192–25 198, 2010.

[80] S. E. Han and D. J. Norris, "Beaming thermal emission from hot metallic bulls eyes," *Optics Express*, vol. 18, no. 5, pp. 4829–4837, 2010.

[81] X. Liu, T. Tyler, T. Starr, A. F. Starr, N. M. Jokerst, and W. J. Padilla, "Taming the blackbody with infrared metamaterials as selective thermal emitters," *Physical Review Letters*, vol. 107, no. 4, 2011.

[82] M. L. Hsieh, J. Bur, Y. S. Kim, and S. Y. Lin, "Direct observation of quasi-coherent thermal emission by a three-dimensional metallic photonic crystal," *Optics Letters*, vol. 38, no. 6, pp. 911–913, 2013.

[83] T. Inoue, M. De Zoysa, T. Asano, and S. Noda, "Single-peak narrow-bandwidth mid-infrared thermal emitters based on quantum wells and photonic crystals," *Applied Physics Letters*, vol. 102, no. 19, 2013.

[84] S. Law, C. Roberts, T. Kilpatrick, L. Yu, T. Ribaudo, E. A. Shaner, V. Podolskiy, and D. Wasserman, "All-semiconductor negative-index plasmonic absorbers," *Physical Review Letters*, vol. 112, no. 1, 2014.

[85] K. Joulain and A. Loizeau, "Coherent thermal emission by microstructured waveguides," *Journal of Quantitative Spectroscopy and Radiative Transfer*, vol. 104, no. 2, pp. 208–216, 2007.

[86] P. Ben-Abdallah and B. Ni, "Single-defect Bragg stacks for high-power narrow-band thermal emission," *Journal of Applied Physics*, vol. 97, no. 10, 2005.

[87] R. Hillenbrand, T. Taubner, and F. Keilmann, "Phonon-enhanced light-matter interaction at the nanometre scale," *Nature*, vol. 418, no. 6894, pp. 159–162, 2002.

[88] T. Taubner, D. Korobkin, Y. Urzhumov, G. Shvets, and R. Hillenbrand, "Near-field microscopy through a SiC superlens," *Science*, vol. 313, no. 5793, p. 1595, 2006.

[89] G. C. R. Devarapu and S. Foteinopoulou, "Mid-IR near-perfect absorption with a SiC photonic crystal with angle-controlled polarization selectivity," *Optics Express*, vol. 20, no. 12, pp. 13 040–13 054, 2012.

[90] D. Korobkin, Y. A. Urzhumov, B. Neuner III, C. Zorman, Z. Zhang, I. D. Mayergoyz, and G. Shvets, "Mid-infrared metamaterial based on perforated SiC membrane: Engineering optical response using surface phonon polaritons," *Applied Physics A: Materials Science and Processing*, vol. 88, no. 4, pp. 605–609, 2007.

[91] F. Marquier, C. Arnold, M. Laroche, J. J. Greffet, and Y. Chen, "Degree of polarization of thermal light emitted by gratings supporting surface waves," *Optics Express*, vol. 16, no. 8, pp. 5305–5313, 2008.

[92] M. Breen, W. Streyer, R. Lu, A. Gao, D. Wasserman, and S. Gong, "High speed mid-infrared detectors based on mems resonators and spectrally selective metamaterials," in *2016 IEEE International Frequency Control Symposium (IFCS)*, May 2016, pp. 1–6.

[93] M. F. MacMillan, R. P. Devaty, and W. J. Choyke, "Infrared reflectance of thin aluminum nitride films on various substrates," *Applied Physics Letters*, vol. 62, no. 7, pp. 750–752, 1993.

[94] N. K. Grady, N. J. Halas, and P. Nordlander, "Influence of dielectric function properties on the optical response of plasmon resonant metallic nanoparticles," *Chemical Physics Letters*, vol. 399, no. 13, pp. 167–171, 2004.

[95] M. A. Ordal, L. L. Long, R. J. Bell, S. E. Bell, R. W. Alexander Jr, C. A. Ward, and R. R. Bell, "Optical properties of the metals Al, Co, Cu, Au, Fe, Pb, Ni, Pd, Pt, Ag, Ti, and W in the infrared and far infrared," *Applied Optics*, vol. 22, no. 7, pp. 1099–1119, 1983.

[96] J. Mink, *Handbook of Vibrational Spectroscopy*. John Wiley & Sons, Ltd, 2006.

[97] M. A. Kats, R. Blanchard, S. Zhang, P. Genevet, C. Ko, S. Ramanathan, and F. Capasso, "Vanadium dioxide as a natural disordered metamaterial: Perfect thermal emission and large broadband negative differential thermal emittance," *Physical Review X*, vol. 3, no. 4, p. 041004, 2013.

[98] W. Streyer, S. Law, A. Rosenberg, C. Roberts, V. A. Podolskiy, A. J. Hoffman, and D. Wasserman, "Engineering absorption and blackbody radiation in the far-infrared with surface phonon polaritons on gallium phosphide," *Applied Physics Letters*, vol. 104, no. 13, 2014.

[99] M. Kreiter, J. Oster, R. Sambles, S. Herminghaus, S. Mittler-Neher, and W. Knoll, "Thermally induced emission of light from a metallic diffraction grating, mediated by surface plasmons," *Optics Communications*, vol. 168, no. 1, pp. 117–122, 1999.

[100] B. J. Lee and Z. M. Zhang, "Design and fabrication of planar multilayer structures with coherent thermal emission characteristics," *Journal of Applied Physics*, vol. 100, no. 6, 2006.

[101] L. G. Wang, G. X. Li, and S. Y. Zhu, "Thermal emission from layered structures containing a negative-zero-positive index metamaterial," *Physical Review B - Condensed Matter and Materials Physics*, vol. 81, no. 7, 2010.

[102] J. J. Greffet, R. Carminati, K. Joulain, J. P. Mulet, S. Mainguy, and Y. Chen, "Coherent emission of light by thermal sources," *Nature*, vol. 416, no. 6876, pp. 61–64, 2002.

[103] I. Balin, N. Dahan, V. Kleiner, and E. Hasman, "Slow surface phonon polaritons for sensing in the midinfrared spectrum," *Applied Physics Letters*, vol. 94, no. 11, 2009.

[104] E. D. Palik, *Handbook of Optical Constants of Solids*, 1985.

[105] S. Vassant, F. Marquier, J. J. Greffet, F. Pardo, and J. L. Pelouard, "Tailoring GaAs terahertz radiative properties with surface phonons polaritons," *Applied Physics Letters*, vol. 97, no. 16, 2010.

[106] S. Vassant, F. Pardo, P. Bouchon, R. Hadar, F. Marquier, J. J. Greffet, and J. L. Pelouard, "Influence of a depletion layer on localized surface waves in doped semiconductor nanostructures," *Applied Physics Letters*, vol. 100, no. 9, 2012.

[107] S. Vassant, A. Archambault, F. Marquier, F. Pardo, U. Gennser, A. Cavanna, J. L. Pelouard, and J. J. Greffet, "Epsilon-near-zero mode for active optoelectronic devices," *Physical Review Letters*, vol. 109, no. 23, 2012.

[108] S. Vassant, I. Moldovan Doyen, F. Marquier, F. Pardo, U. Gennser, A. Cavanna, J. L. Pelouard, and J. J. Greffet, "Electrical modulation of emissivity," *Applied Physics Letters*, vol. 102, no. 8, 2013.

[109] J. I. Watanabe, K. Uchinokura, and T. Sekine, "Surface-phonon polariton on gratings of GaP thin slabs: Raman scattering," *Physical Review B*, vol. 40, no. 11, pp. 7860–7865, 1989.

[110] J. I. Watanabe, K. Uchinokura, and T. Sekine, "Surface-phonon polariton on gratings of GaP thin slabs: Far-infrared reflection," *Physical Review B*, vol. 40, no. 8, pp. 5677–5682, 1989.

[111] A. S. Barker Jr, "Dielectric dispersion and phonon line shape in gallium phosphide," *Physical Review*, vol. 165, no. 3, pp. 917–922, 1968.

[112] A. Mooradian and G. B. Wright, "First order Raman effect in III-V compounds," *Solid State Communications*, vol. 4, no. 9, pp. 431–434, 1966.

[113] F. Marquier, K. Joulain, J. P. Mulet, R. Carminati, J. J. Greffet, and Y. Chen, "Coherent spontaneous emission of light by thermal sources," *Phys. Rev. B*, vol. 69, 2004.

[114] A. K. Hafeli, E. Rephaeli, S. Fan, D. G. Cahill, and T. E. Tiwald, "Temperature dependence of surface phonon polaritons from a quartz grating," *Journal of Applied Physics*, vol. 110, no. 4, 2011.

[115] W. Streyer, K. Feng, Y. Zhong, A. Hoffman, and D. Wasserman, "Engineering the reststrahlen band with hybrid plasmon/phonon excitations," *MRS Communications*, vol. 6, no. 01, pp. 1–8, 2016.

[116] R. A. Soref, Z. Qiang, and W. Zhou, "Far infrared photonic crystals operating in the reststrahl region," *Optics Express*, vol. 15, no. 17, pp. 10 637–10 648, 2007.

[117] K. Feng, W. Streyer, S. M. Islam, J. Verma, D. Jena, D. Wasserman, and A. J. Hoffman, "Localized surface phonon polariton resonances in polar gallium nitride," *Applied Physics Letters*, vol. 107, no. 8, p. 081108, 2015.

[118] C. G. Olson and D. W. Lynch, "Longitudinal-optical-phonon-plasmon coupling in GaAs," *Physical Review*, vol. 177, no. 3, pp. 1231–1234, 1969.

[119] P. Gu, M. Tani, K. Sakai, and T.-R. Yang, "Detection of terahertz radiation from longitudinal optical phonon-plasmon coupling modes in InSb film using an ultrabroadband photoconductive antenna," *Applied Physics Letters*, vol. 77, no. 12, pp. 1798–1800, 2000.

[120] P. Gu, M. Tani, S. Kono, K. Sakai, and X.-C. Zhang, "Study of terahertz radiation from InAs and InSb," *Journal of Applied Physics*, vol. 91, no. 9, pp. 5533–5537, 2002.

[121] M. P. Hasselbeck, D. Stalnaker, L. A. Schlie, T. J. Rotter, A. Stintz, and M. Sheik-Bahae, "Emission of terahertz radiation from coupled plasmon-phonon modes in InAs," *Physical Review B*, vol. 65, no. 23, p. 233203, 2002.

[122] T. Dekorsy, H. Auer, C. Waschke, H. J. Bakker, H. G. Roskos, H. Kurz, V. Wagner, and P. Grosse, "Emission of submillimeter electromagnetic waves by coherent phonons," *Physical Review Letters*, vol. 74, no. 5, pp. 738–741, 1995.

[123] K. S. Singwi and M. P. Tosi, "Interaction of plasmons and optical phonons in degenerate semiconductors," *Physical Review*, vol. 147, no. 2, pp. 658–662, 1966.

[124] O. K. Kim and W. G. Spitzer, "Study of plasmon LO-phonon coupling in Te-doped $Ga_{1-x}Al_xAs$," *Physical Review B*, vol. 20, no. 8, pp. 3258–3266, 1979.

[125] A. A. Kukharskii, "Plasmon-phonon coupling in GaAs," *Solid State Communications*, vol. 13, no. 11, pp. 1761–1765, 1973.

[126] U. Del Pennino, M. G. Betti, C. Mariani, and I. Abbati, "Surface phonons and plasmons of GaAs(110) investigated by high resolution electron energy loss spectroscopy," *Surface Science*, vol. 211-212, no. C, pp. 557–564, 1989.

[127] F. Valle, F. Ganikhanov, and F. Bogani, "Dephasing of LO-phonon-plasmon hybrid modes in n-type GaAs," *Physical Review B - Condensed Matter and Materials Physics*, vol. 56, no. 20, pp. 13 141–13 146, 1997.

[128] E. H. Hwang, R. Sensarma, and S. Das Sarma, "Plasmon-phonon coupling in graphene," *Physical Review B*, vol. 82, no. 19, p. 195406, 2010.

[129] Y. Liu and R. F. Willis, "Plasmon-phonon strongly coupled mode in epitaxial graphene," *Physical Review B - Condensed Matter and Materials Physics*, vol. 81, no. 8, 2010.

[130] A. Woessner, M. B. Lundeberg, Y. Gao, A. Principi, P. Alonso-Gonzlez, M. Carrega, K. Watanabe, T. Taniguchi, G. Vignale, M. Polini, J. Hone, R. Hillenbrand, and F. H. L. Koppens, "Highly confined low-loss plasmons in graphene-boron nitride heterostructures," *Nat Mater*, vol. 14, no. 4, pp. 421–425, 2015.

[131] V. W. Brar, M. S. Jang, M. Sherrott, S. Kim, J. J. Lopez, L. B. Kim, M. Choi, and H. Atwater, "Hybrid surface-phonon-plasmon polariton modes in graphene/monolayer h-BN heterostructures," *Nano Letters*, vol. 14, no. 7, pp. 3876–3880, 2014.

[132] W. J. Moore and R. T. Holm, "Infrared dielectric constant of gallium arsenide," *Journal of Applied Physics*, vol. 80, no. 12, pp. 6939–6942, 1996.

[133] P. Berini, "Figures of merit for surface plasmon waveguides," *Optics Express*, vol. 14, no. 26, pp. 13 030–13 042, 2006.

[134] F. Wang and Y. R. Shen, "General properties of local plasmons in metal nanostructures," *Physical Review Letters*, vol. 97, no. 20, 2006.

[135] D. W. Berreman, "Infrared absorption at longitudinal optic frequency in cubic crystal films," *Physical Review*, vol. 130, no. 6, pp. 2193–2198, 1963.

[136] R. Ruppin, "Electromagnetic energy in dispersive spheres," *Journal of the Optical Society of America A*, vol. 15, no. 2, pp. 524–527, 1998.

[137] F. Proix and M. Balkanski, "Infrared measurements on CdS thin films deposited on aluminium," *physica status solidi (b)*, vol. 32, no. 1, pp. 119–126, 1969.

[138] M. Schubert, T. Hofmann, and J. Šik, "Long-wavelength interface modes in semiconductor layer structures," *Physical Review B*, vol. 71, no. 3, p. 035324, 2005.

[139] S. Vassant, J.-P. Hugonin, F. Marquier, and J.-J. Greffet, "Berreman mode and epsilon near zero mode," *Optics Express*, vol. 20, no. 21, pp. 23 971–23 977, 2012.

[140] A. Röseler and E.-H. Korte, *Infrared Spectroscopic Ellipsometry.* John Wiley & Sons, Ltd, 2006.

[141] T. P. Pearsall, R. Carles, and J. C. Portal, "Single longitudinal-mode optical phonon scattering in $Ga_{0.47}In_{0.53}As$," *Applied Physics Letters*, vol. 42, no. 5, pp. 436–438, 1983.

[142] M. Cardona and G. Guntherodt, *Light Scattering in Solids V.* Springer-Verlag, 1989.

[143] A. K. Sood, J. Menndez, M. Cardona, and K. Ploog, "Interface vibrational modes in GaAs-AlAs superlattices," *Physical Review Letters*, vol. 54, no. 19, pp. 2115–2118, 1985.

[144] M. P. Chamberlain, M. Cardona, and B. K. Ridley, "Optical modes in GaAs/AlAs superlattices," *Physical Review B*, vol. 48, no. 19, pp. 14 356–14 364, 1993.

[145] S.-F. Ren, H. Chu, and Y.-C. Chang, "Phonon dispersion curves of GaAs-AlAs superlattices grown in the [111] and [110] directions," *Physical Review B*, vol. 40, no. 5, pp. 3060–3065, 1989.

[146] N. Mori and T. Ando, "Electron–optical-phonon interaction in single and double heterostructures," *Physical Review B*, vol. 40, no. 9, pp. 6175–6188, 1989.

[147] W. Z. Lin, L. G. Fujimoto, E. P. Ippen, and R. A. Logan, "Femtosecond carrier dynamics in GaAs," *Applied Physics Letters*, vol. 50, no. 3, pp. 124–126, 1987.

[148] M. A. Brummell, R. J. Nicholas, M. A. Hopkins, J. J. Harris, and C. T. Foxon, "Modification of the electron-phonon interactions in GaAs-GaAlAs heterojunctions," *Physical Review Letters*, vol. 58, no. 1, pp. 77–80, 1987.

[149] D.-S. Kim, A. Bouchalkha, J. M. Jacob, J. F. Zhou, J. J. Song, and J. F. Klem, "Confined-to-propagating transition of LO phonons in GaAs/Al_xGa_{1-x}As superlattices observed by picosecond Raman scattering," *Physical Review Letters*, vol. 68, no. 7, pp. 1002–1005, 1992.

[150] J. Shah, R. C. C. Leite, and J. F. Scott, "Photoexcited hot LO phonons in GaAs," *Solid State Communications*, vol. 8, no. 14, pp. 1089–1093, 1970.

[151] Y. B. Shi and I. Knezevic, "Nonequilibrium phonon effects in midinfrared quantum cascade lasers," *Journal of Applied Physics*, vol. 116, no. 12, p. 123105, 2014.

[152] R. C. Iotti, F. Rossi, M. S. Vitiello, G. Scamarcio, L. Mahler, and A. Tredicucci, "Impact of nonequilibrium phonons on the electron dynamics in terahertz quantum cascade lasers," *Applied Physics Letters*, vol. 97, no. 3, p. 033110, 2010.

[153] M. S. Vitiello, R. C. Iotti, F. Rossi, L. Mahler, A. Tredicucci, H. E. Beere, D. A. Ritchie, Q. Hu, and G. Scamarcio, "Non-equilibrium longitudinal and transverse optical phonons in terahertz quantum cascade lasers," *Applied Physics Letters*, vol. 100, no. 9, p. 091101, 2012.